

Institute for Clinical and Experimental Surgery
Saarland University, Homburg/Saar
(Director: Prof. Dr. med. M. D. Menger)

**Adipose tissue-derived microvascular fragments:
In vitro and *in vivo* analysis of prevascularization strategies
for dermal substitutes**

Dissertation with the aim of achieving the doctoral degree
Dr. rer. nat.
at the Medical Faculty of Saarland University

2018

by Thomas Später
born on December 30th, 1984 in Kusel

Dedicated to my parents with deep gratitude

Table of contents

| | |
|---|-----------|
| 1. Summary | 1 |
| 2. Zusammenfassung | 4 |
| 3. Introduction | 7 |
| 4. Aim of the study | 15 |
| 5. Materials and methods | 17 |
| 5.1. Experimental animals | 17 |
| 5.2. Experimental model..... | 17 |
| 5.2.1. MWD and FWM sample preparation | 17 |
| 5.2.2. Scanning electron microscopy | 18 |
| 5.2.3. Isolation of ad-MVF | 18 |
| 5.2.4. Isolation of SVF single cells | 20 |
| 5.2.5. Characterization of ad-MVF and SVF single cells | 21 |
| 5.2.5.1. Viability | 21 |
| 5.2.5.2. Cellular composition | 21 |
| 5.2.6. Seeding of MWD and FWM..... | 22 |
| 5.2.7. Implantation of the dorsal skinfold chamber | 23 |
| 5.2.8. Preparation and filling of full-thickness skin defects | 24 |
| 5.2.9. Stereomicroscopy | 26 |
| 5.2.10. Intravital fluorescence microscopy | 26 |
| 5.2.11. Ultrasound and photoacoustic imaging | 28 |
| 5.2.12. Tail vein bleeding time..... | 28 |
| 5.3. Histology..... | 29 |
| 5.3.1. Matrix incorporation..... | 29 |
| 5.3.2. Collagen content | 30 |
| 5.4. Immunohistochemistry..... | 30 |

| | |
|---|-----------|
| 5.4.1. Epithelialization | 30 |
| 5.4.2. Microvessel density | 31 |
| 5.4.3. Cell apoptosis and proliferation | 32 |
| 5.4.4. Immune cell infiltration..... | 32 |
| 5.5. Experimental protocols | 33 |
| 5.5.1. Experimental protocol 1: Characterization of ad-MVF | 33 |
| 5.5.2. Experimental protocol 2: MWD vs. FWM..... | 33 |
| 5.5.3. Experimental protocol 3: Ad-MVF seeding density..... | 35 |
| 5.5.4. Experimental protocol 4: Ad-MVF vs. SVF single cells | 35 |
| 5.5.5. Experimental protocol 5: Enox treatment | 36 |
| 5.6. Statistical analyses | 37 |
| 6. Results..... | 38 |
| 6.1. Characterization of ad-MVF..... | 38 |
| 6.1.1. Length distribution | 38 |
| 6.1.2. Cellular composition | 39 |
| 6.2. MWD vs. FWM | 40 |
| 6.2.1. Non-seeded MWD and FWM | 40 |
| 6.2.1.1. Surface morphology..... | 40 |
| 6.2.1.2. Epithelialization..... | 41 |
| 6.2.1.3. Vascularization and incorporation..... | 42 |
| 6.2.1.4. Biocompatibility..... | 43 |
| 6.2.2. Ad-MVF-seeded MWD and FWM..... | 44 |
| 6.2.2.1. Ad-MVF distribution | 44 |
| 6.2.2.2. Vascularization and incorporation..... | 44 |
| 6.2.2.3. Epithelialization..... | 47 |
| 6.2.2.4. Apoptotic cell death and proliferation..... | 48 |
| 6.3. Ad-MVF seeding density | 49 |

| | |
|---|------------|
| 6.3.1. Vascularization and incorporation | 49 |
| 6.3.2. Immune cell infiltration..... | 53 |
| 6.3.3. Epithelialization | 53 |
| 6.4. Ad-MVF vs. SVF single cells | 55 |
| 6.4.1. Viability and cellular composition | 55 |
| 6.4.2. Vascularization, hemorrhage formation, and incorporation | 55 |
| 6.4.3. Epithelialization | 59 |
| 6.5. Enox treatment | 61 |
| 6.5.1. Vascularization and tail vein bleeding time..... | 61 |
| 6.5.2. Hemorrhage formation | 63 |
| 6.5.3. Incorporation | 63 |
| 6.5.4. Epithelialization | 64 |
| 6.6. Summary of the results..... | 66 |
| 7. Discussion | 68 |
| 7.1. Discussion of materials and methods..... | 67 |
| 7.1.1. Dorsal skinfold chamber model | 67 |
| 7.1.2. Intravital fluorescence microscopy | 70 |
| 7.2. Discussion of results..... | 71 |
| 7.2.1. Characterization of ad-MVF | 71 |
| 7.2.2. MWD vs. FWM | 72 |
| 7.2.3. Ad-MVF seeding density | 74 |
| 7.2.4. Ad-MVF vs. SVF single cells | 76 |
| 7.2.5. Enox treatment..... | 78 |
| 7.3. Conclusion and clinical perspectives | 80 |
| 8. References | 81 |
| 9. Acknowledgement..... | 99 |
| 10. Publications | 100 |

| | |
|----------------------------------|-----|
| 10.1. Original articles..... | 100 |
| 10.2. Citable abstracts..... | 101 |
| 10.3. Non-citable abstracts..... | 102 |
| 10.4. Awards | 102 |

1. Summary

For the treatment of full-thickness skin defects, autologous split-thickness skin grafting is the gold standard. However, the outcome of this approach may be impaired by scarring, wound contraction, or the lack of vascularization within the wound bed. To counteract these problems, bioengineered off-the-shelf matrices, such as Integra[®] Matrix Wound Dressing (MWD), have been introduced over the past years. This collagen-glycosaminoglycan matrix with a silicone pseudo-epidermis is first implanted into the debrided wound bed. Only after a sufficient vascularization, the silicone layer is removed and the matrix can be covered with a split-thickness skin graft. Noteworthy, the ingrowth of blood vessels into the matrix requires up to 3 weeks. Since wound infection is a threat throughout this time, strategies are needed to improve the vascularization of the matrix. Prevascularization, which aims for the creation of microvascular networks within the matrix prior to its implantation, is such a strategy. Although the seeding of matrices with stem cells showed positive results in the creation of preformed networks, a time-consuming *in vitro* cultivation is necessary to generate the needed number of cells. Moreover, stem cells need too much time to vascularize the entire matrix. To overcome this problem, the seeding of matrices with adipose tissue-derived microvascular fragments (ad-MVF) has recently been introduced as a promising strategy. Ad-MVF can easily be isolated from adipose tissue and, unlike single cells, already represent fully functional blood vessel segments that rapidly reassemble into new microvascular networks within seeded matrices. However, although experimental studies indicate the benefits of ad-MVF as prevascularization units, many questions have to be clarified to allow a successful transfer of this novel approach into clinical practice, as outlined and analyzed in the present doctoral thesis.

For all *in vitro* and *in vivo* parts of this thesis, green fluorescent protein (GFP)⁺ C57BL/6 mice were used as ad-MVF donor animals. The tissue of these animals appears green under blue light excitation, enabling the identification of ad-MVF after their transplantation into GFP⁻ C57BL/6 recipient mice. Non-seeded and ad-MVF- or stromal vascular fraction (SVF)-seeded Integra[®] matrices were implanted into full-thickness skin defects within mouse dorsal skinfold chambers to analyze their vascularization, incorporation, oxygenation, and epithelialization by means of intravital fluorescence microscopy, photoacoustic imaging, histology, and immunohistochemistry over an observation period of 2 weeks.

The aim of a **first set of experiments** was to clarify whether the volumes of epididymal adipose tissue and/or the numbers of ad-MVF depend on the age of the animal. For this

purpose, 7 - 12 months old GFP⁺ C57BL/6 donor mice were used for harvesting their epididymal fat tissue and subsequent ad-MVF isolations. It was found that a comparable volume of ~ 1.4 mL fat tissue can be harvested from animals ranging between 7 - 12 months. Furthermore, a comparable number of ~ 40.000 ad-MVF/mL adipose tissue could be isolated from these mice. The isolated ad-MVF exhibited an average length of ~ 38 μ m and a viability of > 90 %. This indicates that all mice of the analyzed age range can be used for a highly standardized isolation of ad-MVF.

In a **second set of experiments** it was hypothesized that the seeding of ad-MVF on a flowable matrix, which allows a more homogeneous distribution, may result in a faster matrix vascularization and incorporation when compared to MWD. For this purpose, MWD as well as samples of Integra[®] Flowable Wound Matrix (FWM) were seeded with identical numbers of ad-MVF. Of interest, FWM exhibited a more homogeneous distribution of individual ad-MVF when compared to MWD. However, when implanted into full-thickness skin defects within GFP⁻ C57BL/6 recipient mice, this resulted in an increased distance between individual ad-MVF, leading to a prolonged ad-MVF interconnection time as well as a reduced matrix vascularization and incorporation *in vivo*. These results indicate that MWD is more suitable for the treatment of rather large wounds, while FWM may be particularly used for the treatment of small wounds and wounds with irregular geometries which are hardly to access.

In a **third set of experiments** it was hypothesized that the seeding density of ad-MVF is a crucial determinant for an adequate vascularization and incorporation of seeded matrices. For this purpose, MWD was seeded with three different densities of ad-MVF. The results indicate that a minimum density of ~ 80,000 ad-MVF/cm² is required to guarantee a sufficient vascularization and incorporation of implanted MWD *in vivo*. Under clinical conditions, this may be particularly relevant for the treatment of patients with extensive skin defects and/or limited availability of adipose tissue.

Besides the novel approach of ad-MVF prevascularization, the seeding of matrices with vessel-forming single cells of the SVF is a frequently applied strategy. In a **fourth set of experiments** it was hypothesized that the ad-MVF-based prevascularization of MWD is superior to the conventional SVF-based approach. While both ad-MVF and SVF isolates contained a comparable fraction of endothelial cells, perivascular cells, adipocytes, and stem cells, ad-MVF exhibited a significantly higher viability after their isolation. It was further shown that SVF-seeded MWD exhibited a reduced vascularization and incorporation when compared to ad-MVF-seeded MWD *in vivo*. These novel findings indicate that ad-MVF are

highly potent vascularization units that may be even superior to SVF single cells in future tissue engineering applications.

In a **fifth set of experiments** it was hypothesized that the anti-angiogenic properties of low molecular weight heparins (LMWH), such as enoxaparin (enox), prevent the reassembly of seeded ad-MVF into new microvascular networks. It was further hypothesized that the anti-coagulative properties of enox may increase the bleeding risk during network formation within implanted MWD. To test these hypotheses, ad-MVF were isolated from enox- and vehicle-treated GFP⁺ C57BL/6 donor mice, seeded onto MWD and implanted into enox- and vehicle-treated GFP⁻ recipient animals. Intravital fluorescence microscopic, histological, and immunohistochemical analyses revealed that enox does neither inhibit the reassembly of ad-MVF nor promotes implant-induced hemorrhage formation. These novel findings demonstrate that the seeding of MWD matrices with ad-MVF as prevascularization units may also be applied during thromboprophylactic therapy without any concern.

2. Zusammenfassung

Obwohl die Deckung dermalen Wunden mittels autologer Spalthauttransplantate zur klinischen Standardbehandlung zählt, kann der Erfolg dieser Methode durch Komplikationen wie Narbenbildung, Wundkontraktionen oder eine ausbleibende Vaskularisierung des Wundbetts gefährdet werden. Um diese Probleme zu vermeiden, wurden in den letzten Jahren biosynthetische Matrices, wie beispielsweise Integra[®] Matrix Wound Dressing (MWD), entwickelt. MWD ist eine Kollagen-Glykosaminoglykan-Matrix, welche mit einer Pseudo-Epidermis aus Silikon bedeckt ist, um die Austrocknung der Wunde zu verhindern. Erst nach ausreichender Vaskularisierung der Matrix kann die Silikonschicht abgenommen werden und eine Deckung mit Spalthaut erfolgen. Da die Vaskularisierung bis zu 3 Wochen dauern kann und in diesem Zeitraum ein erhöhtes Infektionsrisiko besteht, müssen unbedingt neue Strategien zur Beschleunigung der Vaskularisierung solcher Matrices entwickelt werden. Ein solcher Ansatz ist die Prävasikularisierung, eine Methode, bei der mikrovasikuläre Netzwerke in einer Matrix vor deren Implantation generiert werden. Auch wenn die Besiedlung von Matrices mit Stammzellen bereits positive Ergebnisse bei der Herstellung prävasikularisierter Netzwerke gezeigt hat, sind dabei zeitaufwändige *in vitro* Kultivierungen unabdingbar, um eine ausreichende Zellzahl zu erhalten. Darüber hinaus benötigen Stammzellen zu viel Zeit, bis sie sich in der gesamten Matrix zu neuen Blutgefäßen entwickelt haben. Um diese Probleme zu vermeiden, wurde kürzlich die Prävasikularisierung von Matrices mit mikrovasikulären Fragmenten (ad-MVF) aus Fettgewebe als neue Strategie beschrieben. Ad-MVF können in großen Mengen durch enzymatische Digestion von Fettgewebe gewonnen werden und stellen, im Gegensatz zu Einzelzellen, bereits intakte Gefäßsegmente dar, welche sich innerhalb einer Matrix nur noch zusammenlagern müssen, um vollständige Netzwerke auszubilden. Auch wenn experimentelle Studien den Einsatz von ad-MVF als Prävasikularisierungseinheiten bereits als vielversprechend beschreiben, müssen noch wesentliche Fragen beantwortet werden, um diesen Ansatz erfolgreich in die Klinik einzuführen.

Für alle *in vitro* und *in vivo* Versuche der vorliegenden Arbeit wurden green fluorescent protein (GFP)⁺ C57BL/6 Spendermäuse zur Fettgewinnung und Isolation von ad-MVF verwendet. Das Gewebe dieser Tiere erscheint unter Anregung mit blauem Licht grün und ermöglicht so die Identifikation von ad-MVF nach Implantation in GFP⁻ Empfängertiere. Unbesiedelte und ad-MVF- oder stromal vascular fraction (SVF)-besiedelte Integra[®] Matrices wurden in Vollhautdefekte innerhalb von Rückenhautkammern implantiert und anschließend deren Vaskularisierung, Inkorporation, Oxygenierung und Epithelialisierung mittels

intravitaler Fluoreszenzmikroskopie, photoakustischer Bildgebung, Histologie und Immunhistochemie über einen Zeitraum von 2 Wochen analysiert.

In einem **ersten experimentellen Teil** wurde die Hypothese geprüft, ob die Menge an epididymalem Fettgewebe oder die Anzahl isolierbarer ad-MVF abhängig vom Alter des Spendertieres sind. Zu diesem Zweck wurden 7 - 12 Monate alte GFP⁺ C57BL/6 Mäuse verwendet, um deren epididymales Fett zu entnehmen und ad-MVF zu isolieren. Dabei konnte gezeigt werden, dass aus allen Spendermäusen ein vergleichbares Volumen von ~ 1,4 ml Fettgewebe gewonnen werden kann. Zusätzlich war es bei einer Viabilität von > 90 % möglich, aus allen 7 - 12 Monate alten Tieren ~ 40,000 ad-MVF/ml Fettgewebe zu isolieren, wobei diese eine mittlere Länge von ~ 38 µm aufwiesen. Diese Ergebnisse zeigen, dass aus 7 - 12 Monate alten Spendermäusen eine standardisierte Isolation von ad-MVF möglich ist.

In einem **zweiten experimentellen Teil** wurde die Hypothese geprüft, ob eine homogenere Verteilung von ad-MVF in einer fließfähigen Matrix zu einer verbesserten *in vivo* Vaskularisierung führt. Hierzu wurden sowohl MWD als auch Einzelproben der Integra[®] Flowable Wound Matrix (FWM) mit einer identischen Anzahl von ad-MVF besiedelt. Auf diese Weise konnte gezeigt werden, dass FWM eine homogenere Verteilung von ad-MVF ermöglicht. Dies ging allerdings mit einer erhöhten Distanz einzelner ad-MVF zueinander einher und führte zu einer verlangsamten Netzwerkbildung. Entsprechend war auch die Vaskularisierung und Inkorporation der Matrices verzögert. Dieses Ergebnis zeigt, dass MWD zur Behandlung größerer Wunden eingesetzt werden sollte, während ad-MVF-besiedelte FWM eher in kleinen, irregulär geformten Wunden Anwendung finden könnte.

In einem **dritten experimentellen Teil** wurde die Hypothese geprüft, ob eine zu geringe Dichte von ad-MVF bewirkt, dass eine ausreichende Vaskularisierung implantierter Matrices nicht mehr erfolgen kann. Hierzu wurden MWD mit 3 verschiedenen Dichten von ad-MVF besiedelt. Es konnte gezeigt werden, dass eine Mindestdichte von ~ 80,000 ad-MVF/cm² MWD notwendig ist, um eine ausreichende Vaskularisierung und Inkorporation der Matrices zu erreichen. Dies ist im Speziellen für klinische Anwendungen wichtig, bei denen am Patienten große Defekte gedeckt werden müssen und/oder ein eingeschränktes Volumen an Fettgewebe für die Isolierung von ad-MVF vorhanden ist.

Neben dem Besiedeln von Matrices mit ad-MVF beschreibt der Einsatz der SVF aus Fettgewebe eine klinisch bereits angewandte Methode der Prävasikularisierung. In einem **vierten experimentellen Teil** wurde die Hypothese geprüft, ob eine Prävasikularisierung mit ad-MVF dem konventionellen SVF-basierten Ansatz überlegen ist. Obwohl ad-MVF- und

SVF-Isolate vergleichbare Anteile an Endothelzellen, perivaskulären Zellen, Adipozyten und Stammzellen aufwiesen, war die Viabilität von frisch isolierten ad-MVF höher. Weiterhin konnte gezeigt werden, dass SVF-besiedelte Matrices eine schlechtere Vaskularisierung aufweisen. Diese Ergebnisse zeigen, dass auf Grund ihres hohen Vaskularisierungspotentials ad-MVF gegenüber SVF-Einzelzellen für zukünftige Tissue Engineering-Ansätze deutlich besser geeignet sein könnten.

In einem **fünften experimentellen Teil** wurde die Hypothese geprüft, ob die anti-angiogene Wirkung von niedermolekularen Heparinen (LMWH), wie Enoxaparin (enox), die Netzwerkbildung von ad-MVF verlangsamt. Weiterhin wurde hypothetisiert, dass die anti-koagulativen Eigenschaften von enox zu vermehrten Einblutungen während der Netzwerkbildung innerhalb ad-MVF-besiedelter Matrices führen. Hierzu wurden ad-MVF von GFP⁺ C57BL/6 Mäusen isoliert, welche mit enox oder Vehikel behandelt wurden. Anschließend wurde MWD mit diesen ad-MVF besiedelt und passgenau in Vollhautdefekte innerhalb des Rückenhautkammermodells implantiert. Intravitalmikroskopische, histologische, und immunhistochemische Analysen konnten zeigen, dass enox weder die Netzwerkbildung von ad-MVF verschlechtert, noch Einblutungen innerhalb der Matrices begünstigt. Diese Ergebnisse belegen, dass eine Besiedelung von MWD mit ad-MVF als Prävascularisierungseinheiten bei gleichzeitig angewandter Thromboseprophylaxe problemlos möglich ist.

3. Introduction

As the largest organ of the human body skin does not only represent an important barrier for external threats, such as toxins and microorganisms, but also regulates the body temperature and maintenance of fluid homeostasis [ZHONG et al., 2010; SCHURR et al., 2012]. The vast variety of the skin's functions is based on the complex composition of the two main structural compartments, dermis and epidermis, as well as their ability to interact with each other and to form a highly specialized matrix structure [NORMAN, 1998; BARONI et al., 2012].

The epidermis, which is the outermost layer of the skin, is separated from the dermis through a basement membrane and consists of five different layers: *stratum basale* (basal layer), *stratum spinosum* (spinous layer), *stratum granulosum* (granular layer), *stratum lucidum* (clear layer), and *stratum corneum* (horny layer) [JOHNSTONE and FARLEY, 2005]. Stem cells, acting as regenerative elements, reside within the basal layer and are strongly attached to the underlying basement membrane in order to ensure the lifelong maintenance of the epidermis by their inexhaustible capacity to self-renew and to differentiate into all cell lineages [JENSEN et al., 1999; CANGKRAMA et al., 2013]. While cellular division exclusively takes place within this innermost layer of the epidermis, cells subsequently make their way through all other layers while progressively maturing and finally reaching the outermost *stratum corneum* [ZOUBOULIS et al., 2008]. Although the epidermis provides a stable environmental barrier for the first and initial protection of the organism against external threats, it is considered a rather thin cellular layer that highly depends on nutrient and biomechanical support from the underlying dermis [DALY, 1982].

The dermis mainly consists of collagen (type I + III) and elastin fibers, which are both responsible for the skin's overall elasticity and tensile strength [HUSSAIN et al., 2013]. Interestingly, biomechanical and compositional properties of the skin not only vary between anatomical regions, but are also age-related and, hence, change over time [GUNIN et al., 2014]. A loss of the skin's fundamental functions can be caused by various conditions, such as genetic disorders, chronic wounds, surgical interventions, or thermal trauma. Particularly the latter one can lead to skin defects of different severity levels classified by their wound depth and extent of tissue loss [EVERS et al., 2010; SHEVCHENKO et al., 2010]. Full-thickness skin defects, which are characterized by the complete destruction of both epidermis and dermis as well as the loss of all related and aforementioned regenerative elements, can particularly be caused by severe burns [PAPINI, 2004; SUPP and BOYCE, 2005; BELLAS et al., 2012]. Accordingly, the rapid re-establishment of damaged skin is inevitable in order to

maintain its fundamental protective functions. Although small full-thickness skin defects are able to heal through re-epithelialization from the edges, wounds exceeding 1 cm in diameter require special treatment after the excision of the damaged tissue [PAPINI, 2004].

In clinical practice, the gold standard for the treatment of full-thickness skin defects is split-thickness skin grafting (STSG) [KIRSNER et al., 1997; RUSZCZAK, 2003; VAN DER VEEN et al., 2010; MERUANE et al., 2012]. In this autologous approach, both epidermis and superficial parts of the dermis are harvested from a healthy skin donor site of the patient and subsequently transferred to the debrided wound bed [SHEVCHENKO et al., 2010]. After transplantation, capillaries of the skin graft connect to the vasculature of the underlying host tissue and, thus, allow the supply of nutrients ensuring graft tissue survival [SCHULTZ et al., 2003; SHEVCHENKO et al., 2010]. However, several difficulties are associated with STSG. Besides the common problem of scarring [NGUYEN et al., 2010; VAN DER VEEN et al., 2010], the lack of suitable donor sites is a crucial issue when burn wounds exceed 50 - 60 % of the total body surface area [MACNEIL, 2007; REID et al., 2007; BÖTTCHER-HABERZETH et al., 2010]. Furthermore, particularly wound beds with no adequate vascularization are unable to sufficiently re-connect with the implanted skin graft, resulting in a lack of oxygen and nutrient support.

To counteract these problems, various bioengineered acellular off-the-shelf matrices, such as Integra[®], Matriderm[®], Glyaderm[®], Biobrane[®], or Alloderm[®], have been introduced over the past decades [SUPP and BOYCE, 2005; ALRUBAIY and AL-RUBAIY, 2009; ZHONG et al., 2010; GRAHAM et al., 2013; SHAHROKHI et al., 2014; DEBELS et al., 2015]. When positioned within full-thickness skin defects, these matrices provide an immediate protection against dehydration and microorganisms and are progressively incorporated into the wound bed over time [DEBELS et al., 2015].

Out of the aforementioned skin matrices, particularly Integra[®] Matrix Wound Dressing (MWD; Integra Life Sciences, Ratingen, Germany) is frequently used in clinical applications since many years [HUNT et al., 2000; JENG et al., 2007; KHAN et al., 2010; MERUANE et al., 2012; THINDA et al., 2012; GRAHAM et al., 2013; HULSEN et al., 2014; SINGER et al., 2015]. MWD consists of cross-linked bovine type I collagen and shark cartilage glycosaminoglycan that form a 1.3 mm thick porous structure with an average pore size of 30 - 120 μm [MERUANE et al., 2012; REIFFEL et al., 2012; CHOI et al., 2013]. In clinical routine, MWD, which is covered with a silicone pseudo-epidermis, is initially implanted into the debrided wound bed. Only after a sufficient vascularization of the matrix, the silicone layer is removed and the matrix can be covered with a skin graft of the patient [FRUEH et al., 2016]. However, an adequate

vessel ingrowth into the matrix may still require up to 3 weeks. Since wound infection is a threat throughout this time, a rather slow vascularization represents a major problem of this two-step-procedure and requires further optimization strategies [SHEVCHENKO et al., 2010; VAN DER VEEN et al., 2010; DEBELS et al., 2015].

Over the past decades, various tissue engineering approaches have been developed to improve matrix vascularization. A common strategy is to stimulate the ingrowth of new blood vessels from the surrounding host tissue into implanted matrices via the process of angiogenesis, i.e. the development of new blood vessels from pre-existing ones [AUGER et al., 2013; BLANCO and GERHARDT, 2013]. To initiate this process, the host microvasculature needs to be activated by angiogenic growth factors, such as vascular endothelial growth factor (VEGF) or basic fibroblast growth factor (bFGF) [LASCHKE and MENGER, 2012]. One source of such growth factors may be the host tissue itself, which releases them due to tissue injury or as a consequence of an inflammatory response [LASCHKE et al., 2009]. The availability of such growth factors is not exclusively limited to their physiological niches. In fact, VEGF, bFGF, platelet-derived growth factor (PDGF), or angiogenin, are growth factors which are directly incorporated into matrices by coating technologies to improve their *in vivo* vascularization [LASCHKE and MENGER, 2012]. However, the survival of cells within matrices highly depends on their access to nutrients and oxygen. Since the transport of oxygen is limited to a diffusion distance of 150 - 200 μm , matrices that exceed a thickness of 400 μm in any dimension require rapid vascularization to ensure cell survival and oxygen influx as well as efflux of carbon dioxide and other cellular waste [AUGER et al., 2013]. Hence, although the coating with growth factors has been shown to enhance vascularization of seeded matrices [BAFFOUR et al., 1992], massive cell death still represents a major problem due to the long time needed for newly forming blood vessels to reach particularly core areas [PETITE et al., 2000].

To overcome this problem, several prevascularization strategies have been developed over the last decades. They focus on the generation of a preformed microvasculature within bioengineered matrices prior to their implantation [LASCHKE and MENGER, 2016]. One frequently used approach is the seeding of matrices with vessel-forming cells, such as endothelial progenitor cells (EPCs). These cells can be assigned into early and late EPCs, depending on the time of their appearance during *in vitro* cultivation [HUR et al., 2004; DUTTENHOEFER et al., 2013; SASAGAWA et al., 2016]. Whereas early EPCs contribute to vessel formation by the secretion of angiogenic growth factors, late EPCs differentiate into endothelial cells and form capillary-like tubes [HUR et al., 2004; LASCHKE and MENGER, 2016]. Besides the seeding of matrices with EPCs, various other cell types, such as mesenchymal

stem cells [FORMIGLI et al., 2015; PILL et al., 2015], keratinocytes [GRIFFITH et al., 2005; AUGER et al., 2013], glandular-derived stem cells [EGAÑA et al., 2009], adipose-derived stem cells [MERUANE et al., 2012], dermal fibroblasts [AUGER et al., 2013], and induced pluripotent stem cell-derived endothelial cells [CLAYTON et al., 2015] have also been suggested to be suitable for the prevascularization of matrices. However, all cell-based prevascularization strategies are typically associated with complex and time-consuming cell isolation and cultivation procedures [VAN DER VEEN et al., 2010; LASCHKE and MENGER, 2016]. To address these problems, the seeding of matrices with adipose tissue-derived microvascular fragments (ad-MVF) has recently emerged as a novel and highly promising prevascularization concept.

First described in 1975, ad-MVF from rats and mice have initially been used for the isolation of capillary endothelium in microcirculation and angiogenesis research as well as for functional sprouting assays [WAGNER et al., 1975; WAGNER and MATTHEWS, 1977; VARTANIAN et al., 2006]. Ad-MVF represent a randomized mixture of biologically intact arteriolar, capillary, and venular vessel segments that can easily be isolated in large amounts from adipose tissue by means of mechanical and enzymatic digestion [LASCHKE and MENGER, 2015; FRUEH et al., 2017]. During the past years, ad-MVF have been increasingly used in experimental models for the analysis of tissue vascularization, angiogenesis, inosculation, and network remodeling [LASCHKE and MENGER, 2012; MCDANIEL et al., 2014; FRUEH et al., 2017]. When compared to the aforementioned single cell seeding approaches, ad-MVF offer two main advantages. First, they can easily be isolated from adipose tissue within a relatively short isolation time of only ~ 10 minutes. Second, their intact vessel morphology, consisting of a central lumen, endothelium, and stabilizing mural cells, enables them to form interconnections with each other and the surrounding host tissue. This, in turn, leads to a rapid development of stable and blood-perfused networks within implanted matrices [LASCHKE and MENGER, 2015]. Furthermore, the length of isolated ad-MVF ranges between 40 - 180 μm [PILIA et al., 2014], allowing them to rapidly bridge wide distances within seeded matrices. Moreover, ad-MVF not only release pro-angiogenic growth factors, but also represent a rich source of stem cells and EPCs [MCDANIEL et al., 2014; LASCHKE and MENGER, 2016]. MCDANIEL et al. [2014] reported that stem cells within isolated ad-MVF reside within their physiological niche and, hence, exhibit an elevated proliferation rate as well as a higher differentiation and vessel-forming capacity when compared to adipose tissue-derived single stem cells. So far, several experimental studies have shown that ad-MVF accelerate matrix vascularization of random-pattern flaps [NAKANO et al., 1998], superficial myocardium [NAKANO et al., 1999], epicardial patches [SHEPHERD et al., 2007], volumetric muscle defects [PILIA et al., 2014], pancreatic encapsulating devices [HISCOX et

al., 2008], and matrices for tissue engineering [LASCHKE et al., 2012]. Besides these promising findings, it may be assumed that adipose tissue needed for the isolation of ad-MVF in patients could easily be harvested by liposuction during surgery. Subsequently, the isolated ad-MVF may be used as vascularization units in an intra-operative one-step procedure. Accordingly, the aim of the present doctoral thesis was to test several hypotheses, which are of crucial importance for a transfer of this novel approach into clinical practice.

For all *in vitro* and *in vivo* parts of this thesis, green fluorescent protein (GFP)⁺ C57BL/6 mice were used as donor animals for the harvesting of adipose tissue and the subsequent isolation of ad-MVF. The tissue of these animals appears green under blue light excitation [OKABE et al., 1997], enabling an easy identification of ad-MVF after their transplantation into GFP⁻ C57BL/6 recipient mice. Non-seeded and ad-MVF- or stromal vascular fraction (SVF)-seeded matrices were implanted into full-thickness skin defects within mouse dorsal skinfold chambers of GFP⁻ C57BL/6 recipient mice to analyze their vascularization, incorporation, oxygenation, and epithelialization by means of intravital fluorescence microscopy, photoacoustic imaging, histology, and immunohistochemistry over an observation period of 14 days.

Due to an increasing life expectancy, elderly people may be the main target population for future clinical approaches that could benefit from ad-MVF as prevascularization units [LASCHKE et al., 2014]. However, previous studies have shown that both network formation and vascular remodeling are markedly affected in implanted matrices seeded with ad-MVF isolated from aged donors [LASCHKE et al., 2014]. Based on these observations, the hypothesis of a **first set of experiments** was that older mice also exhibit reduced amounts of adipose tissue as well as lower numbers of ad-MVF when compared to younger animals. For this purpose, epididymal adipose tissue was removed from donor animals within the age range of 7 - 12 months for the isolation of ad-MVF. Subsequently, the average volume of fat tissue as well as the number of isolated ad-MVF was determined. Furthermore, the average length, cellular composition, viability, and overall length distribution of individual ad-MVF were assessed by means of light microscopy.

Besides MWD, Integra Life Sciences has developed a commercially available Flowable Wound Matrix (FWM) of identical composition for the treatment of complex and difficult-to-access wound sites with irregular geometries [TRUONG et al., 2005; GREENWOOD et al., 2009; HIRCHE et al., 2016]. Whereas MWD is a ready-to-use sheet matrix, FWM is delivered as granulate which needs to be hydrated with sterile saline to achieve the injectable matrix of

gel-like consistency. Although MWD and FWM exhibit an identical material composition, variations in sample preparation and application may lead to crucial differences in their architectural properties. According to other studies, this may induce differences in the host tissue response after implantation and, hence, crucially determine the healing process [DRUECKE et al., 2004]. Previous studies have also shown that the pore size of biologically engineered matrices tremendously regulates their vascularization once implanted. In detail, matrices with pore sizes smaller than 200 μm favor the formation of vascular networks with small vessels at high densities, whereas networks with larger blood vessels and lower densities preferentially grow deeper into matrices with a pore size larger than 200 μm [CHOI et al., 2013]. It is also known that both fiber length and diameter represent crucial determinants for the incorporation process of implanted matrices. Penetrating cells are responsible for an adequate and homogeneous tissue growth inside the matrices and can bridge pores through the fibers [MORONI et al., 2006]. Therefore, in a **second set of experiments** it was hypothesized that the differences in MWD and FWM sample preparation lead to variations in pore size, fiber thickness, and fiber length. To test this, non-seeded MWD and FWM were prepared according to the manufacturer's instructions and characterized by means of scanning electron microscopy and histology *in vitro*. Additionally, both matrices were implanted into full-thickness defects of C57BL/6 recipient mice to analyze their *in vivo* biocompatibility, vascularization, epithelialization, and tissue incorporation throughout an observation period of 14 days.

Since previous studies have demonstrated that ad-MVF are rather large and, hence, mainly trapped in the superficial layers of seeded MWD [FRUEH et al., 2017], within this second experimental section it was further hypothesized that a more homogeneous seeding of ad-MVF within FWM can be achieved and, hence, leads to improved matrix vascularization and incorporation. To test this, MWD and FWM were seeded with identical numbers of ad-MVF to assess their distribution and inter-fragment distance, i.e. the average distance of individual ad-MVF to each other. In addition, both ad-MVF-seeded matrices were implanted into full-thickness skin defects within mouse dorsal skinfold chambers of GFP⁻ C57BL/6 recipient mice to analyze their vascularization, epithelialization, and tissue incorporation.

As described above, ad-MVF are able to interconnect with each other and the surrounding host tissue to form intact microvascular networks [FRUEH et al., 2017]. FRUEH et al. [2017] also reported that seeded ad-MVF mostly remain at the superficial layers of MWD. This, in turn, leads to a high density of ad-MVF within these superficial areas. Since the growth rate of angiogenic sprouts is reported to be $\sim 5 \mu\text{m}/\text{h}$ [UTZINGER et al., 2015], the resulting relatively short distance between individual ad-MVF crucially determines the kinetics of the network formation process, leading to a rapid interconnection and onset of blood perfusion

within ad-MVF-seeded MWD. Accordingly, the hypothesis in a **third set of experiments** was that the seeding density of ad-MVF is a crucial determinant for the adequate vascularization and incorporation of matrices. To test this hypothesis, MWD was seeded with three different densities of ad-MVF and implanted into full-thickness skin defects within dorsal skinfold chambers of GFP⁻ C57BL/6 recipient mice to analyze their *in vivo* vascularization and incorporation.

Besides the novel ad-MVF-based approach, another common prevascularization strategy is the seeding of vessel-forming cells, such as endothelial cells or stem cells, onto matrices [STOSICH et al., 2007; SEEBACH et al., 2012]. However, blood vessels do not only exist of one specific cell type but exhibit a complex composition with an inner endothelial lining and surrounding vessel wall-stabilizing cell layers. Taking this into account, the SVF of adipose tissue is frequently used to induce the formation of microvascular networks [CERINO et al., 2017; LOCKHART et al., 2017]. The SVF results from the enzymatic digestion of fat tissue and is a mixture of endothelial cells, pericytes, smooth muscle cells, and stem cells [BOURIN et al., 2013; HASSAN et al., 2014; MAIJUB et al., 2015; CERINO et al., 2017; LOCKHART et al., 2017]. Of interest, the SVF is already evaluated in clinical trials for the regeneration of bone fractures or the treatment of idiopathic pulmonary fibrosis [TZOUVELEKIS et al., 2013; CHARLES-DE-SÁ et al., 2015; RIGOTTI et al., 2016; SAXER et al., 2016]. However, whereas ad-MVF form new microvascular networks via direct interconnection, SVF single cells form a microvasculature *de novo* by reassembling into new blood vessels, which may take a much longer time. Accordingly, the hypothesis of a **fourth set of experiments** was that the ad-MVF-based prevascularization of MWD is superior to the prevascularization with the SVF. To test this hypothesis, both ad-MVF and SVF single cells were isolated from adipose tissue of GFP⁺ C57BL/6 donor mice according to standard protocols. Subsequently, comparable amounts of the isolates were seeded onto MWD and implanted into full-thickness skin defects within dorsal skinfold chambers of GFP⁻ C57BL/6 mice to analyze their vascularization and incorporation *in vivo*.

In a **fifth set of experiments** it was hypothesized that the anti-angiogenic properties of low molecular weight heparins (LMWH), such as enoxaparin (enox), prevent the interconnection of seeded ad-MVF to microvascular networks. Enox is a frequently used drug for the daily thromboprophylactic treatment of hospitalized patients [LEIZOROVICZ et al., 1992; JØRGENSEN et al., 1993; BERGQVIST et al., 1996; MCLEOD et al., 2001; BERGQVIST et al., 2002; LASSEN et al., 2002; LEE et al., 2003; KAKKAR et al., 2008]. Of interest, studies have shown that the interaction of enox with tissue factor pathway inhibitor, tissue factor VIIa, and VEGF leads to a suppression of angiogenesis [DEBERGH et al., 2010; DOGAN et al., 2011]. Angiogenic sprout

formation, in turn, represents a crucial step in the reassembly of individual ad-MVF to newly developing microvascular networks as well as their interconnection with blood vessels of the surrounding host tissue [HOYING et al., 1996]. Besides its anti-angiogenic effect, enox also exhibits strong anti-coagulative properties, which can cause side effects, such as bleeding, during surgical interventions [RABAH et al., 1999; GERLACH et al., 2000; PETERSEN et al., 2004]. Accordingly, it was further hypothesized that enox-treatment increases the bleeding risk during network formation within ad-MVF-seeded MWD. Enox inhibits one major player of the coagulation cascade, factor Xa [SPRONK et al., 2014]. This ultimately prevents the conversion of prothrombin to thrombin, which has an essential role in the clotting process by converting soluble fibrinogen to fibrin [ESMON, 2014]. This factor Xa inhibition has been reported to be directly associated with acute bleeding [DOCKAL et al., 2014; CONNOLLY et al., 2016]. To test the two hypotheses of the fifth experimental section, ad-MVF were first isolated from epididymal fat pads of enox- and vehicle-treated GFP⁺ C57BL/6 donor mice. Subsequently, the isolated ad-MVF were seeded onto MWD and implanted into full-thickness skin defects within dorsal skinfold chambers of enox- and vehicle-treated GFP⁻ C57BL/6 recipient mice to analyze their vascularization, hemorrhage formation, and incorporation by means of intravital fluorescence microscopy, stereomicroscopy, histology, and immunohistochemistry over an observation period of 14 days.

4. Aim of the study

The aim of the present doctoral thesis was to test several hypotheses, which are of crucial importance for transferring the novel approach of ad-MVF-based matrix prevascularization into clinical practice.

In a **first set of experiments** it was hypothesized that older mice exhibit reduced amounts of adipose tissue as well as lower numbers of ad-MVF when compared to younger animals. The following questions were clarified:

- Do older mice contain less adipose tissue when compared to younger ones?
- Do older mice contain less numbers of ad-MVF in their adipose tissue when compared to younger ones?
- Does the cellular composition and/or length distribution of ad-MVF, isolated from older donor animals, vary from that of ad-MVF isolated from younger animals?

In a **second set of experiments** it was hypothesized that the differences in sample preparation between MWD and FWM lead to variations in pore size, fiber thickness, and fiber length. It was further hypothesized that a more homogeneous seeding of ad-MVF within FWM can be achieved and that this leads to improved matrix vascularization and incorporation. The following questions were clarified:

- Do the varying sample preparations of MWD and FWM lead to different pore sizes, fiber length, and fiber thicknesses?
- Can a more homogeneous distribution of ad-MVF within FWM be achieved when compared to MWD?
- Does a more homogeneous distribution of ad-MVF within FWM lead to an improved vascularization and incorporation *in vivo*?

In a **third set of experiments** it was hypothesized that the seeding density of ad-MVF is a crucial determinant for the adequate vascularization and incorporation of matrices. The following questions were clarified:

- Does a low density of ad-MVF lead to an insufficient vascularization and incorporation of seeded MWD?
- Does a low density of ad-MVF lead to a reduced oxygenation of seeded MWD?

In a **fourth set of experiments** it was hypothesized that the ad-MVF-based prevascularization of MWD is superior to the prevascularization with the SVF. The following questions were clarified:

- Do isolated ad-MVF exhibit a higher viability when compared to SVF single cells?
- Does an ad-MVF-based prevascularization lead to an improved vascularization and incorporation of seeded MWD when compared to a prevascularization with the SVF?

In a **fifth set of experiments** it was hypothesized that the anti-angiogenic properties of enox prevent the interconnection of seeded ad-MVF to microvascular networks within seeded MWD. It was further hypothesized that the anti-coagulative properties of enox increase the bleeding risk during network formation within ad-MVF-seeded MWD. The following questions were clarified:

- Do the anti-angiogenic properties of enox lead to reduced network formation within ad-MVF-seeded MWD?
- Do the anti-coagulative properties of enox lead to increased hemorrhage formation within ad-MVF-seeded MWD?

5. Materials and methods

5.1. Experimental animals

All experiments of the present doctoral thesis were approved by the local government animal protection committee (permit numbers: 08/2015, 33/2016, 29/2017) and conducted in accordance with the European legislation on the protection of animals (Directive 2010/63/EU) as well as the NIH guidelines on the care and use of laboratory animals (NIH publication # 85 - 23 Rev. 1985). Dorsal skinfold chambers were implanted in GFP⁻ C57BL/6 recipient mice (Institute for Clinical and Experimental Surgery, Saarland University, Homburg, Germany) with an age of 4 - 6 months and a body weight of 24 - 30 g. Epididymal fat pads were harvested from male GFP⁺ (C57BL/6-Tg(CAG-EGFP)1Osb/J donor mice (The Jackson Laboratory, Bar Harbor, ME, USA) with an age of 7 - 12 months and a body weight of > 30 g to guarantee large amounts of epididymal fat tissue containing a sufficient amount of ad-MVF or SVF single cells for the seeding and *in vivo* implantation of MWD and FWM or corresponding *in vitro* experiments. This transgenic mouse line is transfected with enhanced GFP cDNA under the control of a chicken β -actin promoter and cytomegalovirus enhancer [OKABE et al., 1997]. Accordingly, all tissues of these mice, except red blood cells or hair, appear green under blue light excitation, making it easy to detect GFP⁺ ad-MVF or SVF single cells in GFP⁻ recipient mice [OKABE et al., 1997].

5.2. Experimental model

5.2.1. MWD and FWM sample preparation

For the *in vitro* and *in vivo* analyses in all experimental sections, MWD samples were cut out of a 1.3 mm thick dermal regeneration template single layer without silicone sheet (Figures 1A and B; Integra Life Sciences) with a 4 mm biopsy punch (kai medical, kaiEurope GmbH, Solingen, Germany). For the second experimental section, samples of FWM were additionally generated according to the manufacturer's instructions (Integra Life Sciences) by hydrating 1.25 mg of granulated collagen-glycosaminoglycan with 15 μ L sterile 0.9 % NaCl. In detail, the dry collagen-glycosaminoglycan granulate was carefully placed in a petri dish under sterile conditions and a 20 mL pipette was used to evenly distribute the fluid over the granulate. Subsequently, fine tweezers were used to carefully admix both components to a homogeneous matrix with gel-like consistency (Figures 1C and D). Finally, the matrices were used for *in vitro* characterizations or implanted into full-thickness skin defects within dorsal skinfold chambers of GFP⁻ C57BL/6 recipient mice for *in vivo* analyses.

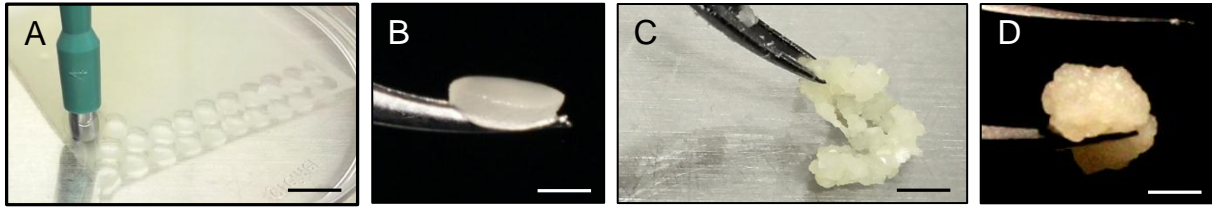


Figure 1. **A:** Cutting MWD samples out of a dermal regeneration template single layer with a 4 mm biopsy punch. Scale bar = 10 mm. **B:** MWD on the tip of a micro forceps after preparation. Scale bar = 2 mm. **C:** Careful homogenization of dry FWM granulate and 0.9 % NaCl inside a sterile petri dish. Scale bar = 2 mm. **D:** Gel-like FWM on the tip of a micro forceps after sample preparation. Scale bar = 2 mm.

5.2.2. Scanning electron microscopy

Scanning electron microscopy was used to observe the morphology of MWD and FWM samples. First, samples were fixed using 2 vol. % glutardialdehyde (Science Services GmbH, Munich, Germany) in 0.1 M sodiumcacodylate buffer at pH 7.4 (Carl Roth GmbH & Co KG, Karlsruhe, Germany) for 10 minutes at room temperature under slow movement. Subsequently, the samples were stored at 4 °C for 24 hours. Thereafter, the samples were washed with 0.1 M sodiumcacodylate buffer and incubated in osmium tetroxide (1 vol. % in 0.2 M sodiumcacodylate buffer) for 1 hour under slow movement and the absence of light. All samples were then washed four times for 10 minutes in distilled water (dH₂O) before being dehydrated by the incubation in an ascending ethanol series (70 vol. %, 80 vol. %, 90 vol. %, 96 vol. %, and 100 vol. %) under slow movement. By washing the samples in a mixture (50:50) of 100 vol. % ethanol and hexamethyldisilazane (Carl Roth GmbH Co KG), followed by washing in pure hexamethyldisilazane, the dehydration was completed. The samples were subsequently covered with hexamethyldisilazane, which evaporated over night. The next day, samples were transferred into conductive carbon adhesive tabs (Plano GmbH, Wetzlar, Germany) and sputtered to make them conductive as a prerequisite for the analysis. The sputtering was performed 3 times for each 60 seconds with gold (SCD 005, Balzers Union, Balzers, Liechtenstein). Then, additional sputtering was performed with carbon (SCD 030, Balzers Union). Lastly, the samples were analyzed by means of a FEI XL 30 ESEM FEG scanning electron microscope (FEI, Hillsboro, OR, USA) under high vacuum conditions at an acceleration voltage of 5 kV in secondary electrons mode.

5.2.3. Isolation of ad-MVF

For the isolation of ad-MVF, GFP⁺ C57BL/6 donor mice were anesthetized by an intraperitoneal injection of xylazine (25 mg/kg body weight; Rompun[®]; Bayer, Leverkusen, Germany) and ketamine (75 mg/kg body weight; Ursotamin[®]; Serumwerke Bernburg, Bernburg, Germany) [GREEN et al., 1981; SAHA et al., 2005]. Subsequently, the animals were transferred onto an operation table in supine position and placed under a stereomicroscope. Paws of the animals were immobilized by taping them to a surgical drape and the abdomen

was depilated with both a razor (AESCLAP ISIS Gt420, Tuttlingen, Germany) and depilatory cream (Asid[®]-med, ASID BONZ, Herrenberg, Germany) followed by disinfection (Octeniderm[®], Schülke & Mayr AG, Norderstedt, Germany) (Figure 2A). Thereafter, a midline laparotomy was performed to gain access to the epididymal fat pads (Figure 2B). Finally, the fat pads were harvested and transferred into a petri dish containing 15 mL Dulbecco's Modified Eagle Medium (DMEM) (PAN Biotech GmbH, Aidenbach, Germany) pre-heated to 37 °C (Figure 2C). Lastly, the animals were sacrificed by cervical dislocation.

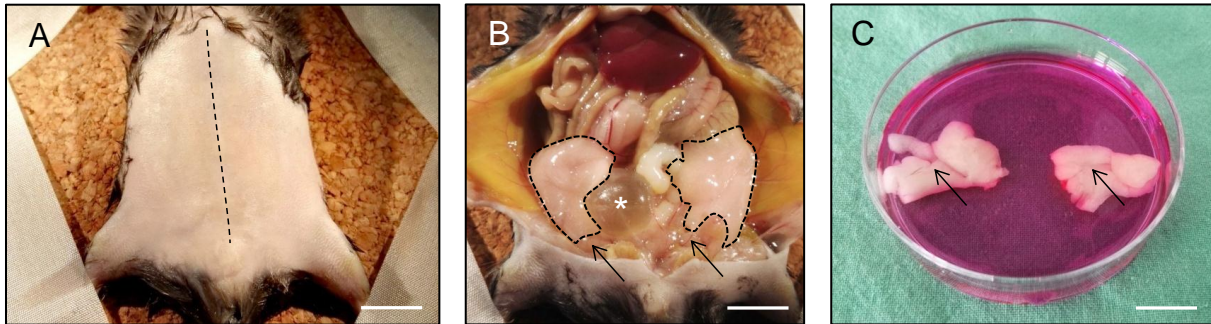


Figure 2. **A:** Immobilized, depilated, and disinfected animal in supine position before midline laparotomy (broken line). Scale bar = 10 mm. **B:** Opened abdomen with laterally unfolded abdominal walls to access the epididymal fat pads (white broken lines). Arrows = epididymis. Asterisk = bladder. Scale bar = 10 mm. **C:** Harvested epididymal fat pads (arrows) in 15 mL DMEM. Scale bar = 17 mm.

After their harvesting, the epididymal fat pads were washed thrice in phosphate-buffered saline (PBS) inside a laminar flow hood (Figure 3A). Subsequently, the fat tissue was transferred into a 14 mL polypropylene (PP) tube to assess its volume by means of the tube scale. Until a homogeneous suspension was achieved (Figure 3B), the fat tissue was minced mechanically with fine scissors. One volume of the minced tissue was then transferred into a beaker glass and two volumes of collagenase NB4G (0.5 U/mL) were added for enzymatic digestion.

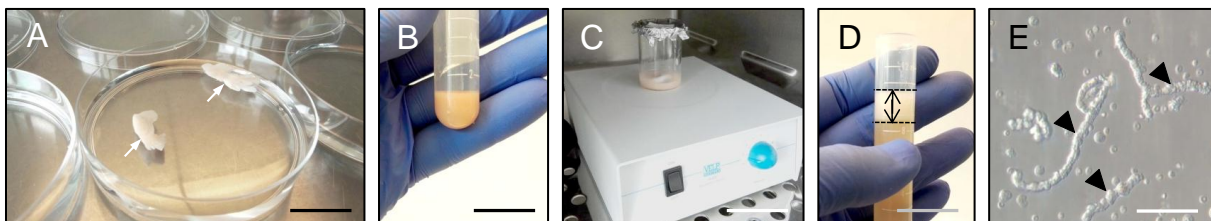


Figure 3. **A:** Harvested epididymal fat pads (arrows) in PBS during the washing process. Scale bar = 22 mm. **B:** Mechanically minced fat pads inside a 14 mL PP tube. Scale bar = 22 mm. **C:** Stirred fat tissue during enzymatic digestion. Scale bar = 50 mm. **D:** Fat supernatant (double arrow) after gravity separation. Scale bar = 26 mm. **E:** Isolated ad-MVF (arrowheads) at the end of the isolation process. Scale bar = 60 μ m.

Subsequently, the tissue was digested for ~ 10 minutes under gentle stirring inside an incubator at 37 °C and 5 % CO₂ (Figure 3C). A constant monitoring of 3 μ L fractions of the digested tissue was conducted by light microscopy (Leica DFC450C, Leica, Wetzlar,

Germany) to determine the time when the ad-MVF were sufficiently separated from the fat tissue and the digestion had to be stopped by neutralizing the collagenase activity with two volumes of PBS (+ 20 % fetal calf serum (FCS)). The cell-vessel suspension was then transferred into a 14 mL PP tube and incubated for 5 minutes at 37 °C to separate the remaining fat by gravity (Figure 3D). To remove remaining fat clots, a 500 µm mesh was subsequently used to filter the suspension (pluriSelect Life Science, Leipzig, Germany). Ad-MVF were then enriched to a pellet by centrifugation for 5 minutes at 600 x g. Finally, the supernatant was completely removed and the obtained pellet resuspended in the required final volume of PBS (+ 20 % FCS) for *in vitro* characterization or the seeding of MWD or FWM for *in vivo* analyses. A final microscopic observation confirmed the successful isolation of ad-MVF (Figure 3E). Noteworthy, the obtained pellet for matrix seeding not only contained purified ad-MVF but also single cells. Hence, the in the following sections called ad-MVF represented a cell-vessel suspension (Figure 4A).

5.2.4. Isolation of SVF single cells

To isolate SVF single cells, adipose tissue was harvested from the epididymal fat pads of GFP⁺ C57BL/6 mice and mechanically minced, as previously described in section 5.2.3. The tissue was then enzymatically digested with collagenase NB4G (0.5 U/mL) for 60 minutes under constant stirring inside an incubator at 37 °C and 5 % CO₂.

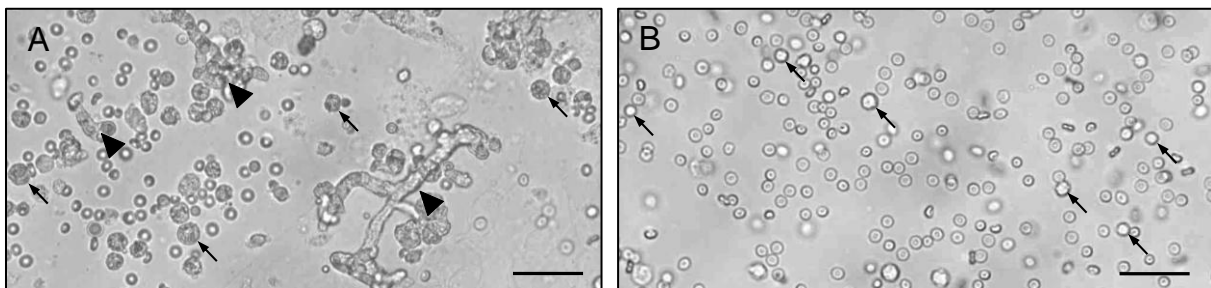


Figure 4. **A:** Cell-vessel suspension directly after the isolation of ad-MVF. Arrowheads = ad-MVF. Arrows = single cells. **B:** Single cells (arrows) representing the SVF at the end of the isolation process. Scale bars = 37 µm.

The digestion was stopped by neutralizing the enzymatic activity with two volumes of PBS (+ 20 % FCS) before the suspension was transferred into a 14 mL PP tube and incubated for 5 minutes at 37 °C to separate the remaining fat by gravity. Once the supernatant was successfully removed, the suspension was filtered through a 40 µm mesh to remove all undigested fat clots and ad-MVF. Single cells were collected, transferred into a 14 mL PP tube, and centrifuged for 5 minutes at 600 x g. The supernatant was then removed until 1 mL was left. Within this volume, the single cells were resuspended, transferred into a 1.5 mL tube, and centrifuged again under identical conditions. Finally, the isolated single cells, representing the SVF (Figure 4B), were used for *in vitro* characterization or seeded onto

MWD for *in vivo* analyses. Noteworthy, ~ 4,000,000 single cells represented the SVF isolate from 1 mL epididymal adipose tissue, corresponding to ~ 40,000 ad-MVF resulting from the isolation of an equivalent fat tissue volume.

5.2.5. Characterization of ad-MVF and SVF single cells

GFP⁺ animals of the first experimental section were assigned to 6 age groups (7, 8, 9, 10, 11, and 12 months old) and the average harvested fat tissue volume per mouse was assessed. After ad-MVF isolations in each age group, 10 % of the final cell-vessel suspension were diluted 1:10 in PBS and 100 μ L of this dilution transferred into a 96-well plate to assess the number of ad-MVF per mL as well as their average size and overall size distribution by means of microscopic counting and extrapolation. A Neubauer counting chamber was used to determine the total number of SVF single cells.

5.2.5.1. Viability

At the end of the isolation process, the final pellet of either ad-MVF or SVF single cells was resuspended in 1 mL PBS including 2 mg/mL bisbenzimidazole (Bb) and 1 mg/mL propidium iodide (PI) (Figures 5A-C). The suspension was incubated for 10 minutes at 37 °C and 5 % CO₂. Then, a 20 μ L fraction of each suspension was transferred into a petri dish and the viability of cells in ~ 50 randomly selected ad-MVF or ~ 1000 SVF single cells was assessed per isolate. For this purpose, Bb was used to stain all cell nuclei of ad-MVF and SVF single cells via binding to their DNA (Figure 5A). Since PI is a red fluorescent dye that only penetrates through damaged cell membranes, it was used as a marker for dead cells (Figures 5B and C) [DENGLER et al., 1995; SHI et al., 2007].

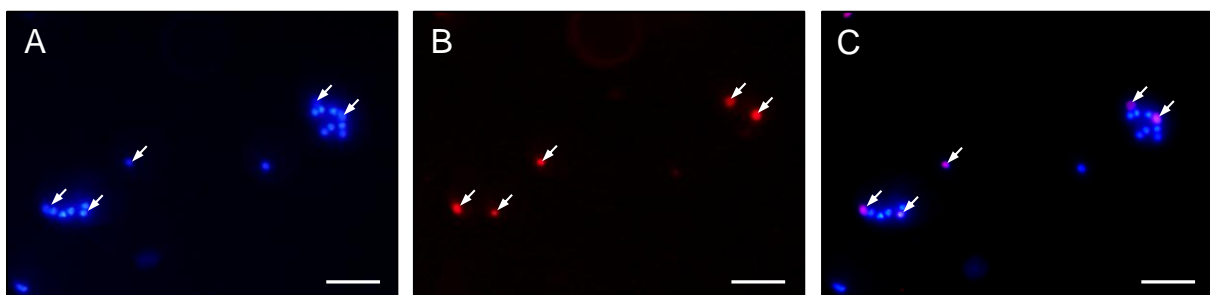


Figure 5. **A:** Bb staining of all ad-MVF cell nuclei. **B:** PI staining of damaged/dead cells. **C:** Merge of A and B, indicating which of the ad-MVF cells are damaged/dead. Arrows = damaged cellular fraction of ad-MVF. Scale bars = 60 μ m.

5.2.5.2. Cellular composition

The cellular composition of ad-MVF or SVF single cells was analyzed by means of flow cytometry. For this purpose, the isolated ad-MVF cell-vessel suspension was further digested into single cells with Accutase[®] (BioLegend, Fell, Germany) for 30 minutes. The resulting ad-

MVF single cells or SVF single cells were then analyzed for the expression of the endothelial cell marker CD31 and the perivascular cell marker α -smooth muscle actin (α -SMA) by using a monoclonal rat anti-mouse CD31-phycoerythrin (PE) antibody (BD Biosciences, Heidelberg, Germany) and a monoclonal rat anti-mouse α -SMA antibody (Thermo Fisher Scientific Inc., Waltham, MA, USA). Additionally, both cell populations were analyzed for the expression of the stromal/stem cell surface markers CD117, CD90, and CD29 by using a monoclonal rat anti-mouse CD117-fluorescein isothiocyanate (FITC) antibody (BD Biosciences) as well as a mouse anti-rat/mouse CD90-FITC antibody (BioLegend) and a monoclonal hamster anti-rat/mouse CD29-FITC antibody (BioLegend). Isotype identical rat IgG-PE or rat IgG-FITC (BD Biosciences), mouse IgG-FITC (BD Biosciences), and hamster IgG-FITC antibodies (BioLegend) served as controls. Finally, the cells were also analyzed for the expression of the adipocyte marker adipocyte-specific adhesion molecule (ASAM) by using a purified polyclonal sheep anti-mouse/human antibody (R&D Systems, Wiesbaden, Germany) followed by a secondary donkey anti-sheep IgG-Alexa488 antibody (Molecular Probes, Eugene, OR, USA). All flow cytometric analyses were performed by means of a FACScan (BD Biosciences). Data were assessed using the software package Cell-Quest Pro (BD Biosciences).

5.2.6. Seeding of MWD and FWM

For the second and fifth set of experiments, MWD samples were placed on a 500 μ m cell strainer and 15 μ L 0.9 % NaCl, containing ~ 15.000 ad-MVF (second set of experiments) or ~ 10.000 ad-MVF (fifth set of experiments), were transferred onto the matrices with a 20 μ L pipette (Eppendorf, Wesseling-Berzdorf, Germany) under the application of negative pressure to assure a sufficient seeding depth (Figures 6A-C).

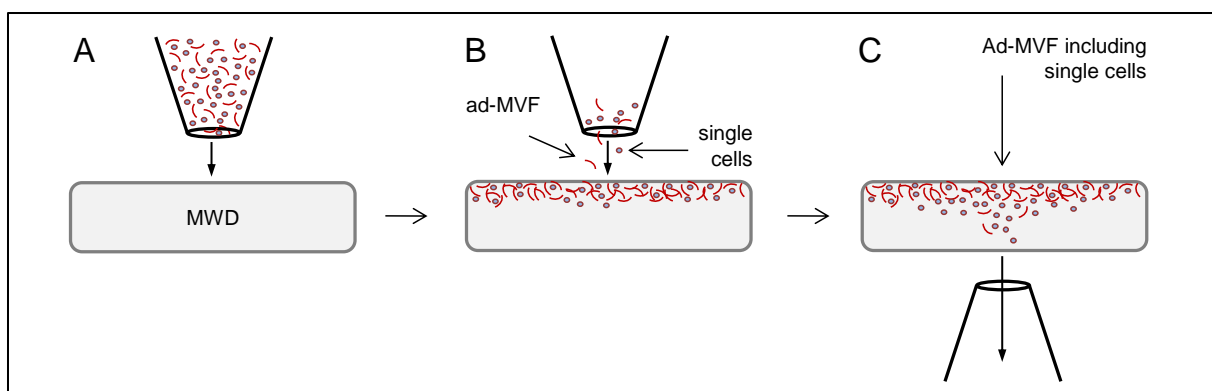


Figure 6. **A:** Ad-MVF cell-vessel suspension within a 20 μ L pipette before seeding. **B:** Seeding of the ad-MVF cell-vessel suspension onto a MWD sample. Note that the ad-MVF mainly remain at the superficial part of the matrix. **C:** Deeper penetration of single cells into MWD, initiated by the application of negative pressure from below the matrix.

For the second set of experiments, FWM was prepared according to the manufacturer's instructions by hydrating 1.25 mg of the granulated collagen-glycosaminoglycan with 15 μ L of 0.9 % NaCl, either containing \sim 15.000 ad-MVF or vehicle only. After the admixture process, the matrix presented a gel-like consistency and was used for *in vitro* characterization or *in vivo* analyses.

For the third set of experiments, different densities of ad-MVF were seeded onto MWD and subsequently analyzed *in vivo*. Besides the previously used number of \sim 15.000 ad-MVF, which was defined as a high density (HD) and served as control group, lower numbers of \sim 10.000 ad-MVF (medium density; MD) and \sim 5.000 ad-MVF (low density; LD) were additionally seeded in additional groups (Figure 7).

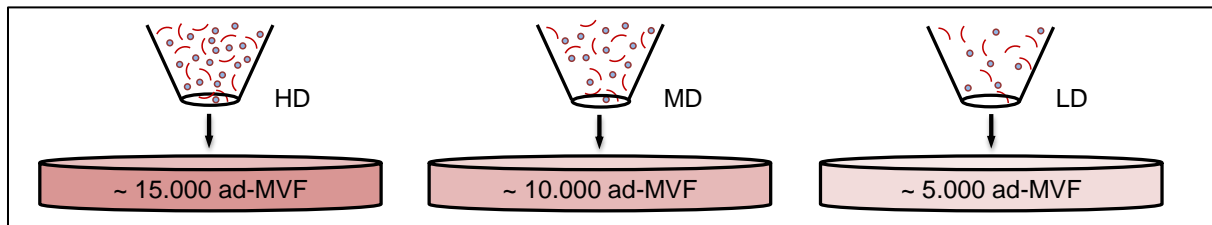


Figure 7. MWD was seeded with different numbers of ad-MVF, including \sim 15.000 (high density; HD), which served as control group, as well as \sim 10.000 (medium density; MD) and 5.000 ad-MVF (low density; LD).

For the fourth set of experiments, \sim 10.000 ad-MVF including \sim 200.000 single cells, resulting from a digestion of 250 μ L adipose tissue, were enriched to a final pellet and subsequently resuspended in 10 μ L 0.9 % NaCl for matrix seeding. All SVF single cells from 250 μ L adipose tissue, i.e. \sim 1,000,000 cells, were also resuspended in 10 μ L 0.9 % NaCl for the SVF-seeding of MWD, corresponding to the equivalent overall number of cells per ad-MVF-seeded matrix. Of note, to prevent the extraction of single cells from the seeded matrices, no negative pressure was applied during the seeding process in the fourth set of experiments.

5.2.7. Implantation of the dorsal skinfold chamber

To analyze implanted MWD or FWM *in vivo*, a modified mouse dorsal skinfold chamber model was used according to SORG et al. [2009]. First described in 1943, the dorsal skinfold chamber model can be used to study the microcirculation in living animals by means of intravital fluorescence microscopy [ALGIRE, 1943; PAPENFUSS et al., 1979; LEHR et al., 1993; LASCHKE et al., 2011]. For the implantation of the dorsal skinfold chamber (Irola Industriekomponenten GmbH & Co. KG, Schonach, Germany), which consists of two symmetrical titanium frames (Figure 8A), the mice were first anesthetized by intraperitoneal injection of ketamine and xylazine, as previously described.

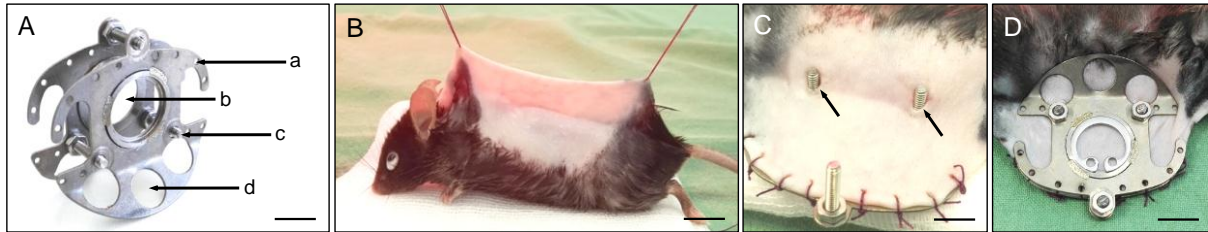


Figure 8. **A:** Dorsal skinfold chamber, consisting of two symmetrical titanium frames (*a* = holes for suturing the frame to the dorsal skinfold of the mouse, *b* = observation window, *c* = connecting screw, *d* = recess for weight reduction). Scale bar = 8 mm. **B:** Cranially and caudally affixed dorsal skinfold of a GFP⁺ C57BL/6 mouse. Scale bar = 8 mm. **C:** Screws (arrows) through the skin of the mouse to connect the second titanium frame. Scale bar = 5 mm. **D:** Connected second titanium frame including a snap ring for the hermetical closure of the chamber tissue. Scale bar = 9 mm.

As soon as a deep anesthesia of the animals was confirmed by toe pinch, the fur was first roughly and then chemically removed from the animals' back by means of a razor (Isis GT608, Aesculap GmbH, Suhl, Germany) and depilatory cream (asid-med crème, Asid Bonz GmbH, Herrenberg, Germany). To prevent cream-induced inflammatory irritations, the hair-free back was cleaned with both warm water and medical disinfectant spray (Schülke & Mayr AG, Zürich, Switzerland). Thereafter, the skinfold of the mice was cranially and caudally affixed at midline by two silk sutures (Figure 8B). One titanium frame of the chamber was fixed to the back side of the skinfold on its superior edge before two openings were prepared at the base of the skinfold in order to pass through the connecting screws from the back side to the front side (Figure 8C). By means of these screws, the second frame was connected to the first one. Screw nuts and the subsequent hermetical closure of the chamber tissue with a cover glass and a snap ring finalized the preparation procedure (Figure 8D). To maintain the body temperature throughout the operation procedure, the animals were constantly positioned near a heat source. Furthermore, eyes were covered with Bepanthen[®] moisturizing cream (Bayer Vital GmbH, Leverkusen, Germany) to prevent their desiccation. To further avoid postoperative alterations of the local microcirculation due to anesthesia and surgery, the mice were allowed to recover for 48 hours after the chamber preparation.

5.2.8. Preparation and filling of full-thickness skin defects

Forty-eight hours after implantation of the dorsal skinfold chamber, a full-thickness skin defect was created in the center of the observation window. For this purpose, the anesthetized mice were fixed on a Plexiglas stage and the skinfold chamber was horizontally positioned under a stereomicroscope (Leica M651, Leica). A 4 mm biopsy punch was used to carefully mark the outlines of the 4 mm defect on the skin of the mice (Figure 9A). Subsequently, microsurgical instruments were used to create a roundly shaped full-thickness skin defect by removing the epidermis, the dermis, and the underlying muscle layers including the panniculus carnosus muscle (Figure 9B).

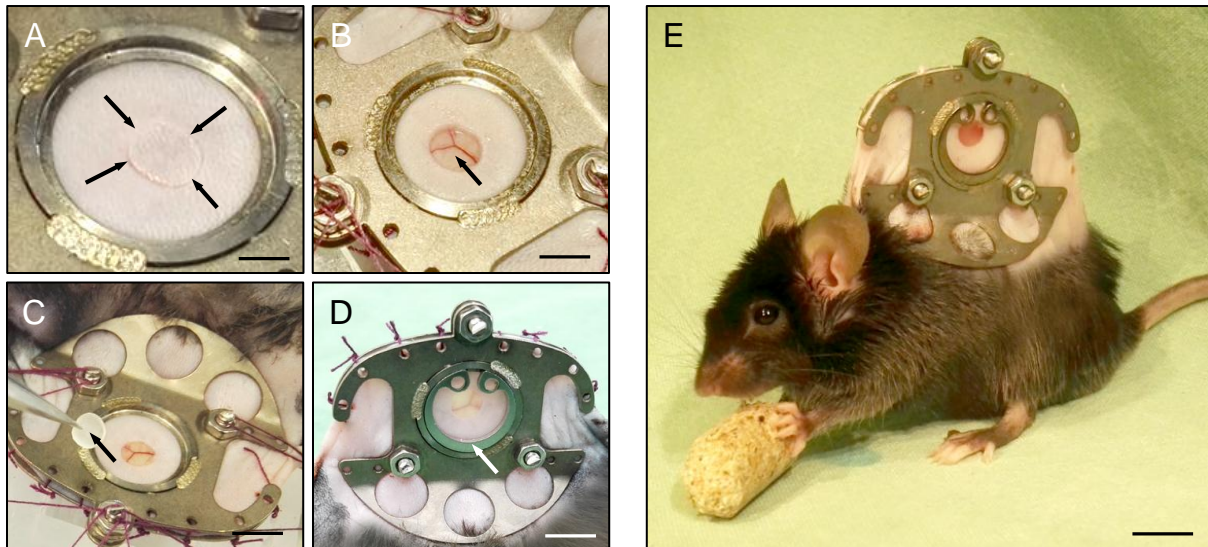


Figure 9. **A:** Outlines (arrows) of the skin defect, gently marked by a 4 mm biopsy punch. Scale bar = 3 mm. **B:** Full-thickness skin defect (arrow). Scale bar = 4 mm. **C:** Filling of the full-thickness skin defect with non-seeded MWD (arrow). Scale bar = 6.6 mm. **D:** Skin defect, covered with a cover glass that is fixed with a snap ring (arrow). Scale bar = 5 mm. **E:** GFP^{-/-} C57BL/6 recipient mouse showing normal behavior 48 hours after the creation of a full-thickness skin defect within the dorsal skinfold chamber. Scale bar = 9 mm.

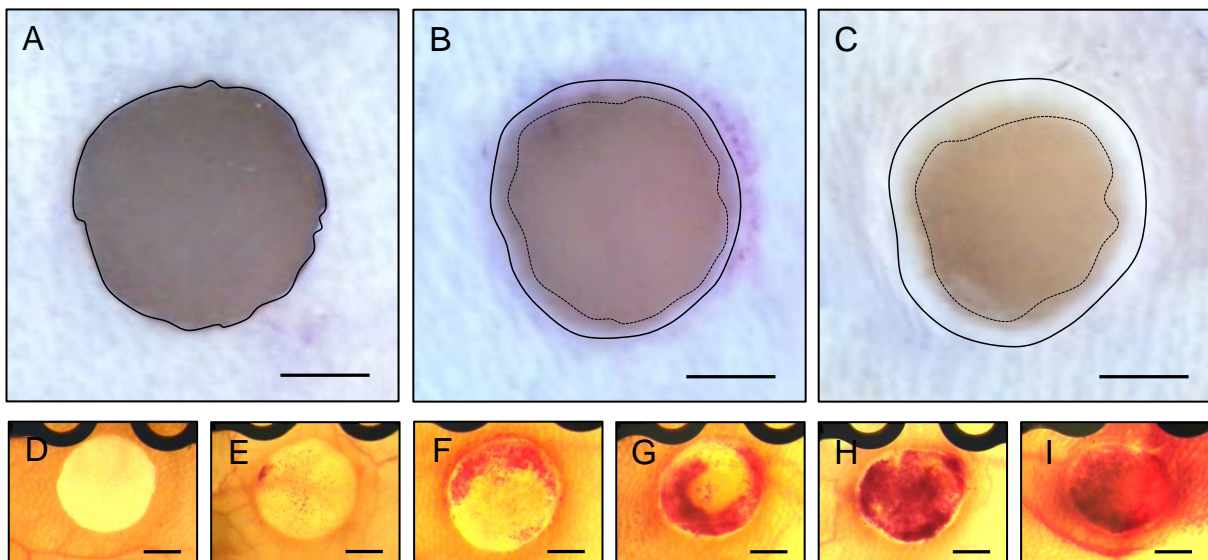


Figure 10. **A-C:** Epi-illumination stereomicroscopy of non-seeded MWD within the dorsal skinfold chamber of a GFP^{-/-} C57BL/6 recipient mouse on day 0 (A), 6 (B), and 14 (C) after implantation. Closed lines = matrix border. Broken lines = non-epithelialized area. Scale bars = 1.4 mm. **D-I:** Trans-illumination stereomicroscopy of ad-MVF-seeded MWD within the dorsal skinfold chamber of GFP^{-/-} C57BL/6 recipient mice, displaying different manifestations of matrix-induced bleedings according to a semi-quantitative hemorrhagic score, i.e. 1: No bleeding (D), 2: 1-25 % (E), 3: 26-50 % (F), 4: 51-75 % (G), 5: 76-100 % (H), 6: Bleeding exceeding matrix surface (I). Scale bars = 1.3 mm.

Directly after the creation of the full-thickness skin defect, non-seeded, ad-MVF-seeded, or SVF-seeded MWD or FWM were carefully placed into the wound bed (Figure 9C). After the matrices were inserted, the observation window of the chamber was closed by means of a removable cover glass and a snap ring (Figure 9D). Shortly after the implantation, the mice already showed normal behavior and eating habits (Figure 9E).

5.2.9. Stereomicroscopy

To analyze epithelialization (Figures 10A-C) and hemorrhage formation (Figures 10D-I) of the implanted matrices by means of planimetry, the anesthetized animals were fixed on a Plexiglas stage and the dorsal skinfold chamber was positioned under a stereomicroscope (Leica M651, Leica). The chamber tissue was then visualized in epi-illumination to detect epithelialized and non-epithelialized matrix areas. To allow a quantitative analysis by means of the computer-assisted system CapImage (Zeintl, Heidelberg, Germany), a DVD system was used to record all microscopic images. The epithelialized area (% of the total matrix area) was calculated by the equation: $(\text{Total matrix area} - \text{non-epithelialized matrix area}) / (\text{total matrix area}) * 100$. In addition, trans-illumination was used to evaluate the extent of hemorrhage formation (% of matrix surface area) by means of a semi-quantitative hemorrhagic score as follows: 1: No bleeding, 2: 1-25 %, 3: 26-50 %, 4: 51-75 %, 5: 76-100 %, 6: Bleeding exceeding matrix surface (Figures 10D-I).

5.2.10. Intravital fluorescence microscopy

Intravital fluorescence microscopy was used to analyze the *in vivo* vascularization of implanted MWD or FWM over time. By means of this technique, specifically dynamic processes, such as angiogenesis, can be repetitively visualized and recorded for the quantitative assessment of microhemodynamic parameters. For contrast enhancement, 0.1 mL of the plasma marker 5 % FITC-labeled dextran (150,000 Da; Sigma-Aldrich, Taufkirchen, Germany) were injected intravenously (i.v.) into the retrobulbar venous plexus of the anesthetized mice. Then, the observation window of the chamber was placed under an Axiotech microscope (Zeiss, Oberkochen, Germany). Images were recorded with a charge-coupled device video camera (FK6990; Pieper, Schwerte, Germany) and stored on DVD for off-line analyses. The analyses were performed by the computer-assisted off-line analysis system CapImage (Zeintl). The vascularization of implanted, non-seeded and ad-MVF-seeded MWD or FWM within the second, third, and fifth set of experiments was assessed in 12 regions of interest (ROIs), 6 along the total vertical and horizontal axis of each matrix (Figure 11A). The vascularization of implanted, ad-MVF- or SVF-seeded MWD in experimental section 4 was separately assessed in 4 ROIs of each matrix' center and border zones (Figure 11B). Each ROI that exhibited red blood cell (RBC)-perfused microvessels was defined as a perfused ROI (% of all counted ROIs). Furthermore, the functional microvessel density was measured as the total length of all RBC-perfused microvessels per ROI (cm/cm^2). Additionally, the diameter (d , μm) and the centerline RBC velocity (v , $\mu\text{m}/\text{s}$) of 40 randomly selected microvessels were assessed (Figures 12A and B). The latter parameter was measured using the line-shift method [DE VRIESE et al., 1995] (Figure 12D).

For this purpose, a measurement line is defined within the lumen of each blood vessel of interest and the blood flow is recorded in real-time for 10 seconds (Figure 12C).

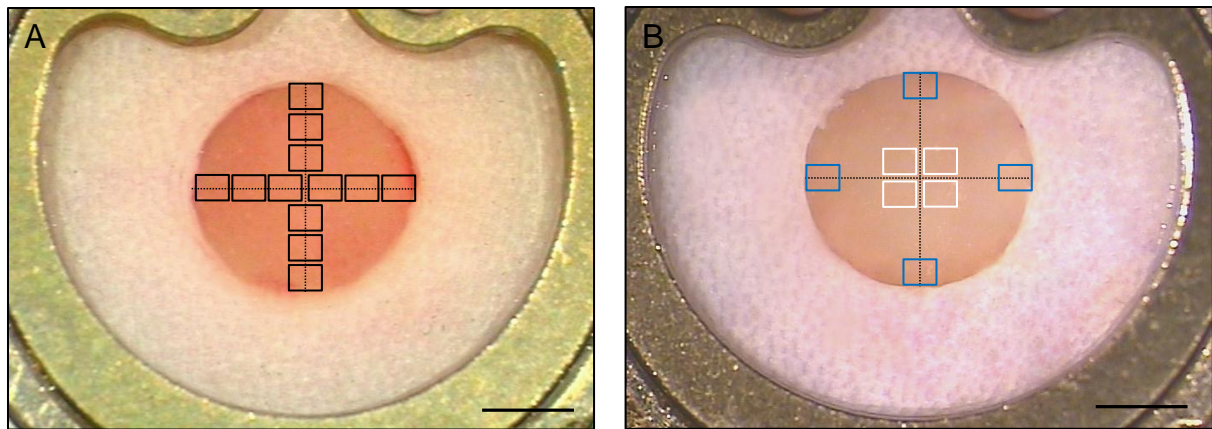


Figure 11. A, B: Overview of the dorsal skinfold chamber observation window showing defined ROIs for intravital fluorescence microscopic assessment of microhemodynamic parameters in experimental protocols 2, 3, and 5 (A) as well as 4 (B). Black frames in A = 12 ROIs along the vertical and horizontal axis of the matrix. Blue and white frames in B = border (blue) and center (white) zones of implanted matrices. Scale bars = 1.5 mm.

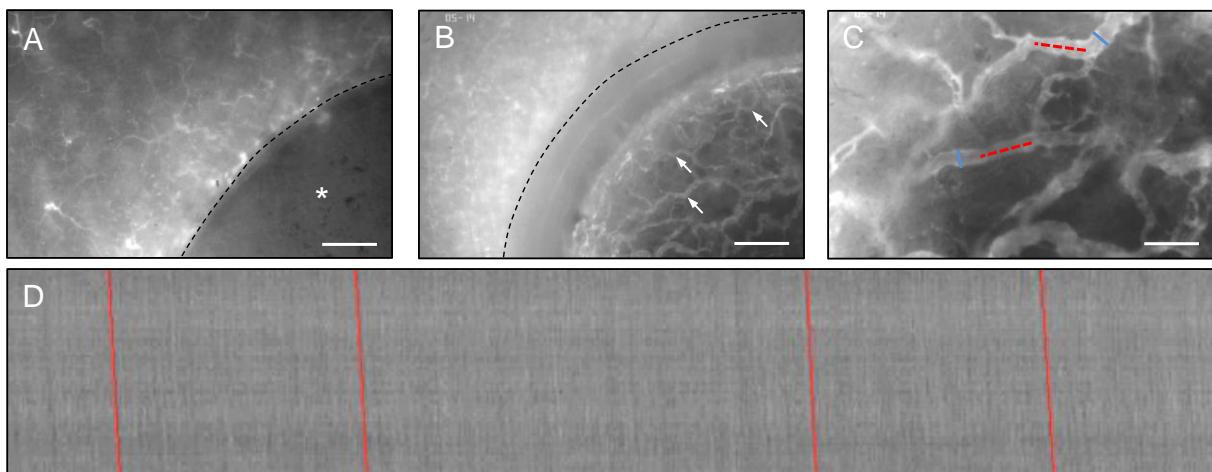


Figure 12. A: ROI of implanted MWD on day 0 (day of implantation), showing no microvessels within the matrix. Asterisk = matrix. Dotted line = matrix border. Scale bar = 500 μm . **B:** ROI with fully perfused MWD on day 14 after implantation into a full-thickness skin defect of a GFP⁺ C57BL/6 recipient mouse. Dotted line = matrix border. Arrows = microvessels. Scale bar = 500 μm . **C:** Measurement of microvessel diameter (blue lines) and centerline RBC velocity (dotted red lines). Scale bar = 100 μm . **D:** Illustration of the line shift diagram for the measurement of centerline RBC velocity. Red lines = Resulting slope from the measurement of the blood flow.

During this time, the grey value of every field of image is continuously created along the defined measurement line and stored on a memory unit. Accordingly, the computer generates a line-shift diagram based on all consecutive grey values. This diagram shows bright and dark lines that result from gaps inside the blood plasma or erythrocytes flowing along the measurement line (Figure 12D). Based on the slope of these lines, the final velocity is calculated. Additionally, vessel diameter and centerline RBC velocity were used to calculate the wall shear rate (γ , s^{-1}) of individual microvessels by means of the Newtonian definition $\gamma = 8 \times \frac{v}{d}$.

5.2.11. Ultrasound and photoacoustic imaging

Ultrasound and photoacoustic imaging were used to measure the hemoglobin oxygen saturation (sO_2) of non-seeded and ad-MVF-seeded MWD by means of a Vevo LAZR system (VisualSonics Inc., Toronto, ON, Canada) and a real-time microvisualization LZ550 linear-array transducer (VisualSonics Inc.). This transducer worked with a center frequency of 40 MHz. All samples were embedded in ultrasound gel (Aquasonic 100; Parker, Fairfield, NJ, USA) to prevent interference with ultrasound coupling. For *in vitro* analyses, freshly seeded, non-implanted MWD (Figures 13A and B) was first analyzed to assess the values of oxygenation within ad-MVF directly after their seeding onto the matrix.

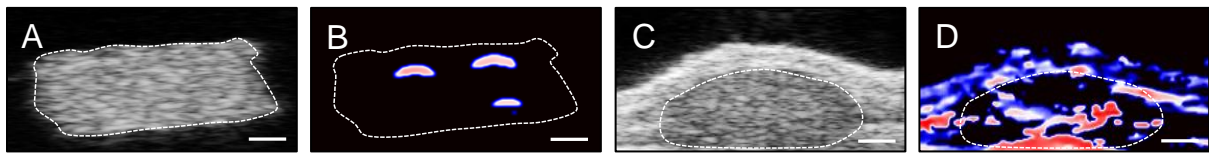


Figure 13. A-D: B-mode ultrasound (A, C) and photoacoustic imaging (B, D) of ad-MVF-seeded MWD directly after seeding (A, B) as well as 14 days after implantation into full-thickness skin defects within dorsal skinfold chambers of GFP⁻ C57BL/6 recipient mice (C, D). Broken lines = matrix border. Red areas = high oxygenation. Blue areas = low oxygenation. Black areas = No oxygenation. Scale bars = 600 μ m.

To further assess the oxygenation of implanted, ad-MVF-seeded matrices *in vivo* (Figures 13C and D), chamber-equipped mice were first anesthetized with 1.5 % isoflurane in air and fixed in prone position on a heated stage. Both heart rate and breathing rate were constantly monitored while the body temperature was maintained at 37 °C (THM100; Indus Instruments, Houston, TX, USA). Noise signalling, which may originate from the titanium frames, was prevented by covering the skinfold chamber with a 3 mm soft polyvinyl chloride (PVC) mask (Sagustu International GmbH, Bruchmühlbach-Miesau, Germany). To achieve three-dimensional high-resolution B-mode ultrasound images, the scanhead was driven by a linear motor, acquiring two-dimensional images at regular spatial intervals, parallelly and uniformly spaced at 150 μ m intervals over the entire matrix. Photoacoustic images were taken to detect sO_2 within the samples at 850 nm with a two-dimensional gain of 34 dB *in vitro* and 32 dB *in vivo* [RICH and SESHADRI, 2015]. All values were calculated by means of the Vevo LAB software (FUJIFILM VisualSonics Inc.).

5.2.12. Tail vein bleeding time

In the fifth set of experiments, the tail vein bleeding time was measured in enox- and vehicle-treated animals. For this purpose, a transverse incision over the lateral tail vein was made. The cut was performed where the diameter of the tail was ~ 2.5 mm. This was ~ 25 mm proximal from the tail tip (Figure 14A). The tail was immediately placed in 0.9 % NaCl, pre-heated to ~ 37 °C, and the time from the incision to the cessation of bleeding was measured as tail vein bleeding time [BROZE et al., 2001] (Figures 14B-D).

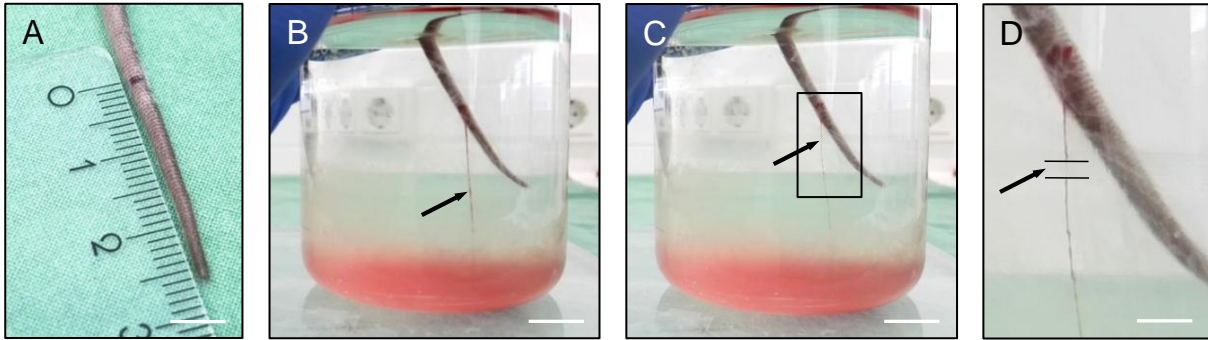


Figure 14. **A:** For the assessment of the tail vein bleeding time, the cut position was marked ~ 25 mm proximal from the tail tip. Scale bar = 6 mm. **B:** Tail placed inside 37 °C warm 0.9 % NaCl directly after incision. Leaking blood forming a downward moving thread (arrow). Scale bar = 20 mm. **C:** Cessation of bleeding, as defined as the time point when the blood flow exhibits gaps (arrow). Scale bar = 20 mm. **D:** Insert of C, showing the time point of cessation. Arrow = gap of broken blood thread, indicating the cessation of bleeding. Scale bar = 5 mm.

5.3. Histology

For histological analyses, all analyzed MWD specimens were fixed in formalin (Carl Roth GmbH & Co. KG, Karlsruhe, Germany). To prevent FWM samples of the second experimental section from dissolving in formalin, they were embedded in Tissue-tek[®] O.C.T. compound (A. Hartenstein GmbH, Würzburg, Germany) with following quick-freezing in liquid nitrogen at -196 °C. All samples were subsequently cut into 3 µm thick sections and processed for histological analyses.

5.3.1. Matrix incorporation

First, a hematoxylin and eosin (HE) staining was performed according to standard procedures (Figure 15).

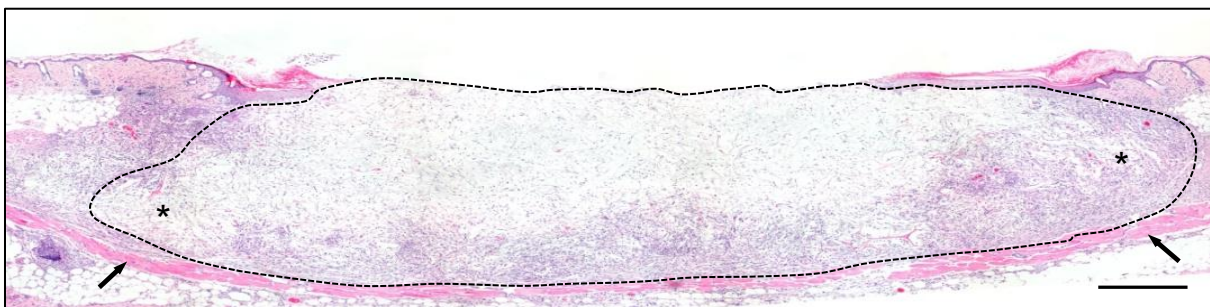


Figure 15. Representative HE staining of non-seeded MWD on day 14 after implantation into a full-thickness skin defect within a dorsal skinfold chamber of a GFP⁻ C57BL/6 recipient mouse. Broken line = matrix border. Asterisks = border zones of the matrix. Arrows = panniculus carnosus muscle of the dorsal skinfold chamber preparation. Scale bar = 350 µm.

To assess fiber length (Figure 16A), fiber thickness (Figure 16B), and pore size (Figure 16C) of non-implanted MWD and FWM in the second experimental section, 5 randomly selected ROIs per HE-stained section were analyzed by using a BX60 microscope (Olympus, Hamburg, Germany) and the imaging software cellSense Dimension 1.11 (Olympus).

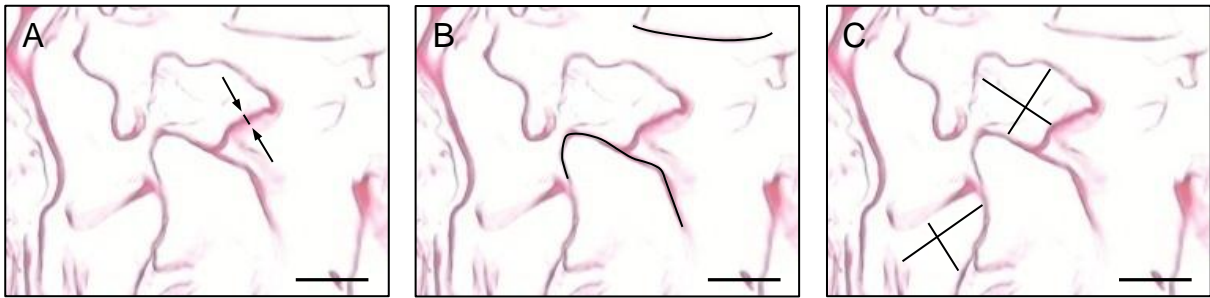


Figure 16. A-C: Representative HE staining of FWM for the *in vitro* measurement of fiber thickness (A; black line, arrows), fiber length (B; black lines), and interfiber distance (C; black lines). Scale bars = 40 μm .

5.3.2. Collagen content

The reddish appearance of Sirius red under polarized light [JUNQUEIRA et al., 1979; RADHIKA et al., 2016] was used to visualize mature collagen fibers in normal skin and within non-seeded, ad-MVF-seeded, or SVF-seeded MWD and FWM (Figures 17A-C) in 4 ROIs of each sample using a BX60 microscope (Olympus) and the imaging software cellSense Dimension 1.11 (Olympus). The total collagen ratio (%) was assessed by dividing the density of collagen fibers within the matrices with the density of collagen fibers of the normal skin.

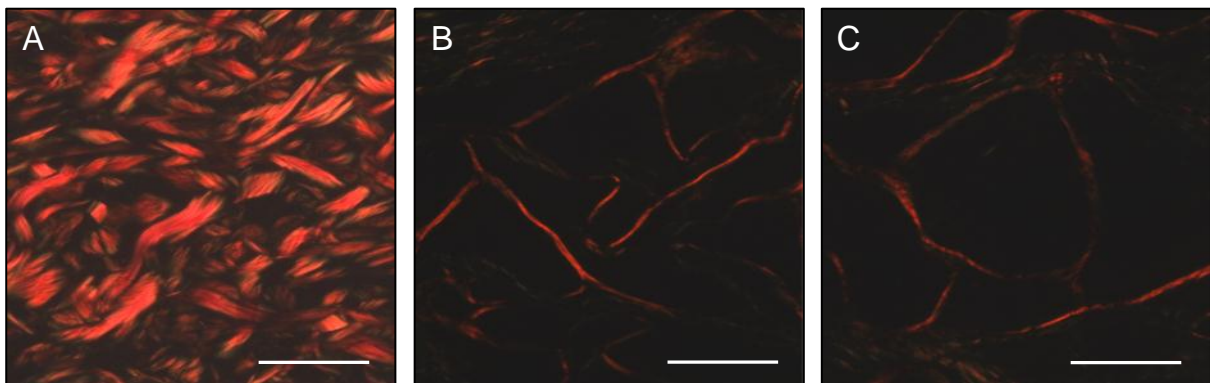


Figure 17. A-C: Polarized light microscopy of Sirius red-stained sections of normal skin (A) as well as ad-MVF-seeded, vehicle-treated (B) and enox-treated (C) MWD 14 days after implantation into full-thickness skin defects within dorsal skinfold chambers of GFP⁻ C57BL/6 recipient mice. Scale bars = 125 μm .

5.4. Immunohistochemistry

5.4.1. Epithelialization

To confirm the stereomicroscopic results of matrix epithelialization on day 14 after implantation, sections of the largest cross-sectional diameter of ad-MVF or SVF-seeded MWD or FWM were incubated with a rabbit polyclonal anti-cytokeratine antibody (1:100; Abcam, Cambridge, UK) as primary antibody followed by a biotinylated goat anti-rabbit IgG antibody (ready-to-use; Abcam) as secondary antibody. The biotinylated antibody was detected by peroxidase-labeled-streptavidin (1:50; Sigma-Aldrich) and 3-amino-9-ethylcarbazole (Abcam) was used as chromogen.

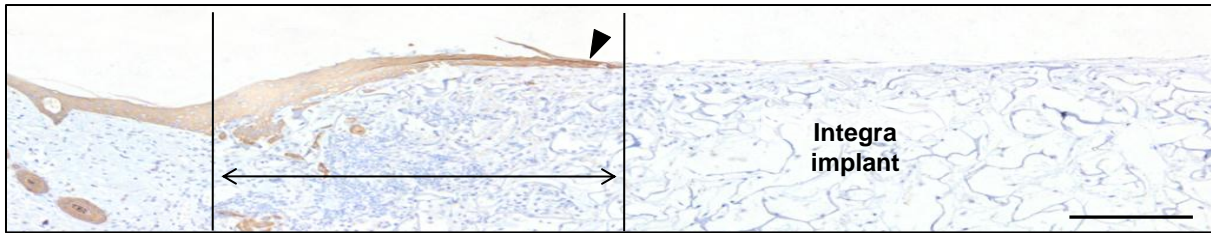


Figure 18. Immunohistochemical detection of the cytokeratine⁺ epithelial layer (arrowhead) covering non-seeded MWD on day 14 after implantation into a full-thickness skin defect within a dorsal skinfold chamber of a GFP⁻ C57BL/6 recipient mouse. The double arrow indicates the epithelialized part of the matrix. Scale bar = 125 μ m.

To assess the cytokeratine⁺ epithelial layer (Figure 18), a BZ-8000 microscopic system (Keyence, Osaka, Japan) was used and the total matrix diameter was measured. Subsequently, the length of the epithelialized matrix surface was detected. Matrix epithelialization was then calculated as: length of cytokeratine⁺ epithelial layer / total diameter of matrix * 100.

5.4.2. Microvessel density

To assess the density of GFP⁺ microvessels within implanted MWD and FWM, further samples were co-stained using a monoclonal rat anti-mouse antibody against the endothelial cell marker CD31 (1:100; Dianova, Hamburg, Germany) and a polyclonal goat antibody against GFP (1:200; Rockland Immunochemicals, Limerick, PA, USA) while a goat anti-rat-IgG Alexa555 (1:200; Life Technologies, Ober-Olm, Germany) and a biotinylated donkey anti-goat antibody (1:20; Dianova) served as secondary antibodies. The biotinylated antibody was detected by streptavidin-Alexa488 (1:50; Life Technologies) and cell nuclei were stained with Hoechst 33342 (2 μ g/mL; Sigma-Aldrich). This co-staining (Figures 19A-C) allowed the detection of GFP⁺ microvessels, which originated from the seeded ad-MVF of GFP⁺ C57BL/6 donor mice, within GFP⁻ C57BL/6 recipient animals.

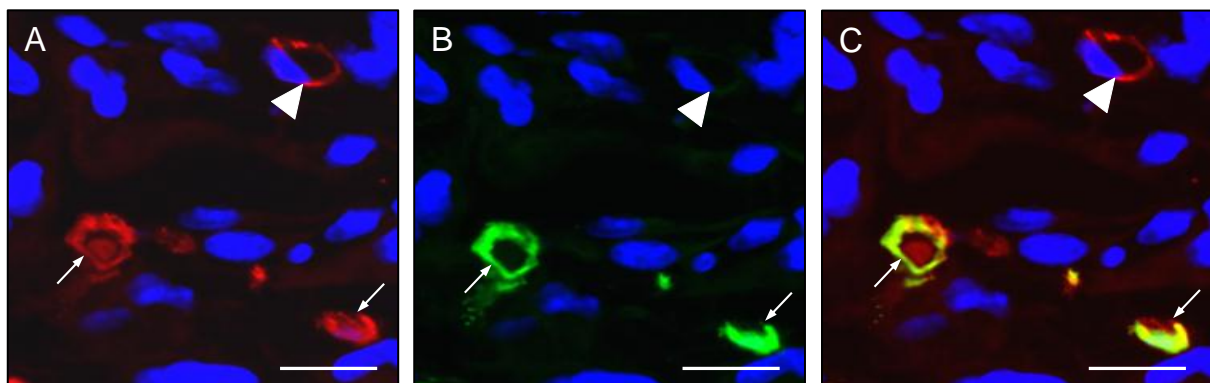


Figure 19. A-C: Immunohistochemical detection of CD31⁺/GFP⁺ microvessels in ad-MVF-seeded MWD on day 14 after implantation into a full-thickness skin defect within a dorsal skinfold chamber of a GFP⁻ C57BL/6 recipient mouse. C = overlay of A (showing CD31⁺ microvessels) and B (showing GFP⁺ microvessels originating from the seeded ad-MVF cell-vessel suspension). Arrows = CD31⁺/GFP⁺ microvessels. Arrowhead = CD31⁺/GFP⁻ microvessel. Scale bars = 15 μ m.

Hence, the density of CD31⁺ (mm⁻²) microvessels as well as the fraction of CD31⁺/GFP⁺ microvessels (%) could be quantitatively analyzed within the matrices on day 14 after implantation. In experimental section 2, the density of CD31⁺ microvessels, which was assessed within 20 randomly selected ROIs within ad-MVF-seeded MWD and FWM, was used to generate the coefficient of variation (cv). For this purpose, the standard deviation of the microvessel density was divided by its mean.

5.4.3. Cell apoptosis and proliferation

For the identification of apoptotic cleaved caspase-3⁺ (Figure 20A) and proliferating Ki67⁺ (Figure 20B) cells within the matrices, histological sections were incubated with a rabbit polyclonal anti-cleaved caspase-3 antibody (1:100; New England Biolabs, Frankfurt, Germany) and a rabbit polyclonal anti-Ki67 antibody (1:500; Abcam) as primary antibodies followed by a biotinylated goat anti-rabbit IgG antibody (ready-to-use; Abcam) as secondary antibody. The biotinylated antibody was detected by peroxidase-labeled-streptavidin (1:50; Sigma-Aldrich) and 3-amino-9-ethylcarbazole (Abcam) was used as chromogen. The sections were counterstained with Mayer's hemalaun (Merck, Darmstadt, Germany).

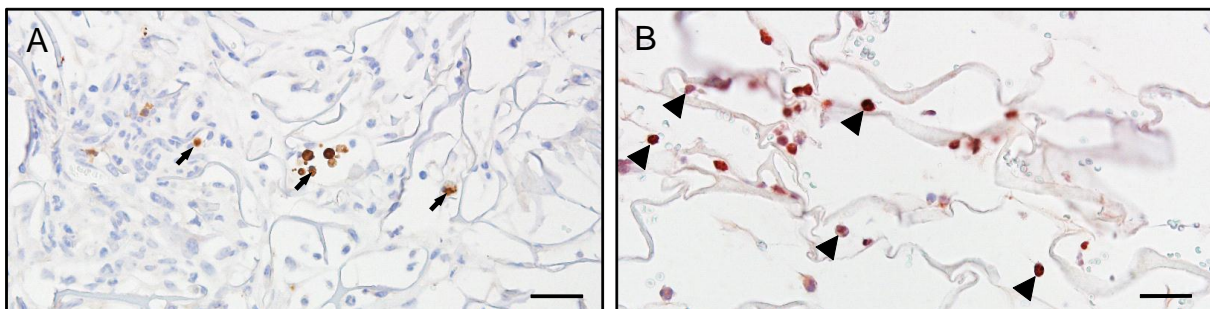


Figure 20. A, B: Immunohistochemical detection of apoptotic cleaved caspase-3⁺ (A; arrows) and proliferating Ki67⁺ cells (B; arrowheads) in ad-MVF-seeded FWM on day 14 after implantation into full-thickness skin defects within mouse dorsal skinfold chambers of GFP⁻ C57BL/6 recipient mice. Scale bars = 50 μ m.

5.4.4. Immune cell infiltration

To assess the number of myeloperoxidase (MPO)⁺ neutrophilic granulocytes, MAC387⁺ or CD68⁺ macrophages, and CD3⁺ lymphocytes within the matrices (Figures 21A-C), sections were incubated with a rabbit polyclonal anti-MPO antibody (1:100; Abcam), a rabbit polyclonal anti-MAC387 antibody (1:50; Abcam) or a rabbit polyclonal anti-CD68 antibody, and a rabbit polyclonal anti-CD3 antibody (1:100; Abcam) as primary antibodies followed by a biotinylated goat anti-rabbit IgG antibody (ready-to-use; Abcam). The biotinylated antibody was detected by peroxidase-labeled-streptavidin (1:50; Sigma-Aldrich) and 3-amino-9-ethylcarbazole (Abcam) was used as chromogen. The sections were counterstained with Mayer's hemalaun (Merck) and the number of immune cells (mm⁻²) was quantitatively assessed in 6 randomly selected ROIs per section by means of light microscopy (BX60).

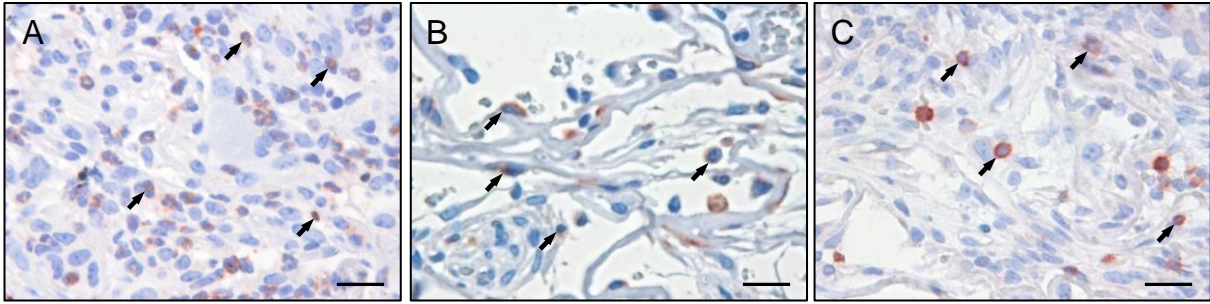


Figure 21. A-C: Immunohistochemical detection of MPO^+ neutrophilic granulocytes (A, arrows), $MAC387^+$ macrophages (B, arrows), and $CD3^+$ lymphocytes (C, arrows) in ad-MVF-seeded MWD on day 14 after implantation into full-thickness skin defects within mouse dorsal skinfold chambers of GFP^- C57BL/6 recipient mice. Scale bars = 37 μm .

5.5. Experimental protocol

5.5.1. Experimental protocol 1: Characterization of ad-MVF

In the first set of experimental, ad-MVF isolates from GFP^+ C57BL/6 donor mice ($n = 18$), assigned to 6 different age groups (7, 8, 9, 10, 11, and 12 months old), were characterized. The volume of isolated epididymal fat from each donor mouse as well as the amount of isolated ad-MVF per mL adipose tissue and their average length was determined ($n = 3$ per age group). To gain further insights into the cellular composition of ad-MVF, a fraction of each isolate was parallelly analyzed by means of flow cytometry ($n = 3$ per age group). Furthermore, samples from all isolates ($n = 18$) were used to assess the ad-MVF size distribution. For this purpose, the length of ~ 100 randomly selected ad-MVF per isolate was measured.

Accordingly, the following groups were investigated in this experimental section:

- Ad-MVF of 7 months old donor animals ($n = 3$)
- Ad-MVF of 8 months old donor animals ($n = 3$)
- Ad-MVF of 9 months old donor animals ($n = 3$)
- Ad-MVF of 10 months old donor animals ($n = 3$)
- Ad-MVF of 11 months old donor animals ($n = 3$)
- Ad-MVF of 12 months old donor animals ($n = 3$)

5.5.2. Experimental protocol 2: MWD vs. FWM

In the second set of experiments, samples of both non-seeded MWD ($n = 3$) and FWM ($n = 3$) were prepared and their surface morphologies were characterized by means of scanning electron microscopy. Additionally, MWD ($n = 3$) and FWM ($n = 3$) were prepared to analyze their fiber thickness, fiber length, and interfiber distance *in vitro* using HE-staining. To assess the cv of the microvessel density within ad-MVF-seeded MWD ($n = 3$) and FWM ($n = 3$), the

matrices were seeded with a comparable number of ~ 15.000 ad-MVF and analyzed by means of light microscopy.

For *in vivo* analyses, non-seeded MWD (n = 8) and FWM (n = 8) as well as ad-MVF-seeded MWD (n = 11) and FWM (n = 11) were implanted into full-thickness skin defects within dorsal skinfold chambers of 38 GFP⁻ C57BL/6 recipient mice. To assess epithelialization and vascularization of the matrices, the mice were repetitively analyzed by means of stereomicroscopy and intravital fluorescence microscopy on day 0 (day of implantation) as well as 3, 6, 10, and 14 (Figure 22). At the end of the 2-week observation period, the animals were sacrificed by means of cervical dislocation and the dorsal skinfold chamber preparations were processed for histological and immunohistochemical analyses of microvessel density, collagen content, apoptotic cell death and proliferation, epithelialization, and immune cell infiltration. For additional immunohistochemical analyses at an earlier time point, animals of ad-MVF-seeded matrices (n = 3 per group) were already sacrificed on day 6 after implantation.

Accordingly, the following groups were investigated in this experimental section:

- Non-seeded, non-implanted MWD (control group, n = 3)
- Non-seeded, non-implanted FWM (n = 3)
- Non-seeded, implanted MWD (control group, n = 8)
- Non-seeded, implanted FWM (n = 8)
- Ad-MVF-seeded, non-implanted MWD (control group, n = 3)
- Ad-MVF-seeded, non-implanted FWM (n = 3)
- Ad-MVF-seeded, implanted MWD (control group, n = 11)
- Ad-MVF-seeded, implanted FWM (n = 11)

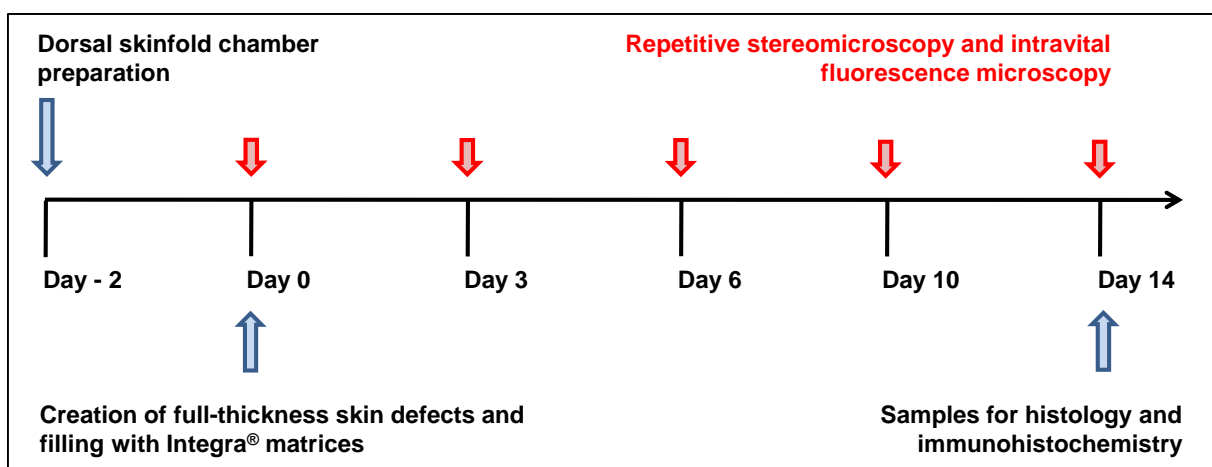


Figure 22. Schematic outline of the experimental protocol used for experimental protocols 2, 3, and 4.

5.5.3. Experimental protocol 3: Ad-MVF seeding density

In the third set of experiments, ad-MVF were isolated from 8 GFP⁺ donor mice and seeded onto MWD in a high density (HD; ~ 15.000 ad-MVF; n = 8), a medium density (MD; ~ 10.000 ad-MVF; n = 8), and a low density (LD: ~ 5.000 ad-MVF; n = 8). Importantly, ~ 15.000 ad-MVF represent the number of fragments for seeding of MWD used in the identical setting of previous studies [FRUEH et al., 2017]. Therefore, the HD group served as a control group. All seeded matrices were subsequently used to fill full-thickness skin defects of 24 GFP⁻ C57BL/6 recipient mice. According to Figure 22, repetitive stereomicroscopy and intravital fluorescence microscopy were used to assess the epithelialization, hemorrhage formation, and vascularization of the matrices over time. Furthermore, photoacoustic images of 3 matrices per group were acquired on day 0 and 14 to detect the sO₂ levels within the seeded matrices. On day 14, the mice were sacrificed by means of cervical dislocation and the dorsal skinfold chamber preparations were processed for histological and immunohistochemical analyses of microvessel density, collagen content, immune cell infiltration, and epithelialization.

Accordingly, the following groups were investigated in this experimental section:

- Ad-MVF-seeded, implanted MWD (HD, control group, n = 8)
- Ad-MVF-seeded, implanted MWD (MD, n = 8)
- Ad-MVF-seeded, implanted MWD (LD, n = 8)

5.5.4. Experimental protocol 4: Ad-MVF vs. SVF single cells

In the fourth set of experiments, epididymal donor fat tissue was harvested from 8 GFP⁺ C57BL/6 donor mice to subsequently analyze the viability and composition of SVF single cells (n = 4) and ad-MVF (n = 4) by means of fluorescence microscopy and flow cytometry *in vitro*.

For *in vivo* analyses, both SVF single cells and ad-MVF were isolated from adipose tissue of 8 GFP⁺ C57BL/6 donor mice and subsequently seeded onto 16 MWD samples. These matrices were then implanted into full-thickness skin defects within dorsal skinfold chambers of 16 GFP⁻ C57BL/6 recipient mice. According to Figure 22, repetitive stereomicroscopy and intravital fluorescence microscopy were used to assess the epithelialization, hemorrhage formation, and vascularization of the matrices over time. On day 14, the mice were sacrificed by means of cervical dislocation and the dorsal skinfold chamber preparations were processed for histological and immunohistochemical analyses of microvessel density, collagen content, and epithelialization.

Accordingly, the following groups were investigated in this experimental section:

- Ad-MVF-seeded, implanted MWD (control group, n = 8)
- SVF-seeded, implanted MWD (n = 8)

5.5.5. Experimental protocol 5: Enox treatment

In the fifth set of experiments, ad-MVF were isolated from 3 enox- (8 mg/kg dissolved in 100 μ L 0.9 % NaCl, subcutaneously (s.c.)) and 3 vehicle-treated (100 μ L 0.9 % NaCl, s.c.) GFP⁺ C57BL/6 donor mice and seeded onto 16 MWD samples. Thereafter, the matrices were implanted into full-thickness skin defects of enox- and vehicle-treated GFP⁻ C57BL/6 recipient mice. Importantly, the used enox dosage of 8 mg/kg corresponded to the clinically used dose of 0.5 mg/kg for thromboprophylactic treatment of hospitalized patients [CHOUSSAT et al., 2002; SANDERINK et al., 2002; REAGAN-SHAW et al., 2008; RONDINA et al., 2010]. After the implantation of ad-MVF-seeded MWD, the recipient animals were continuously treated daily with either enox (8 mg/kg dissolved in 100 μ L 0.9 % NaCl) or vehicle (100 μ L 0.9 % NaCl) throughout the observation period of 2 weeks. According to Figure 23, repetitive stereomicroscopy and intravital fluorescence microscopy were used to assess the epithelialization, hemorrhage formation, and vascularization of the matrices over time.

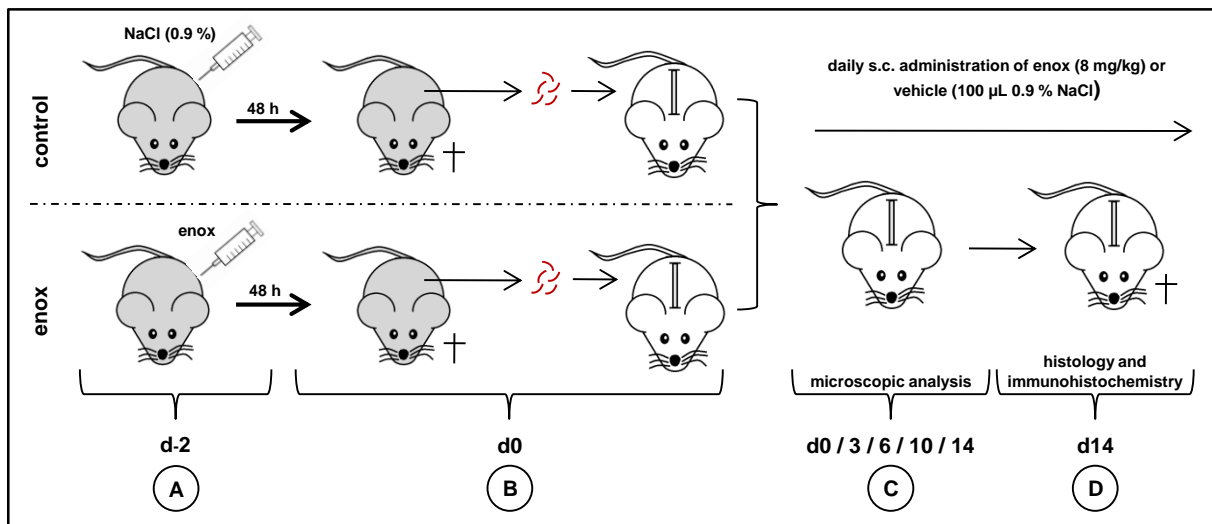


Figure 23. **A:** GFP⁺ donor mice were pretreated once daily with enox or vehicle for 48 hours. **B:** Ad-MVF were harvested from the epididymal fat pads of the donor animals, seeded onto MWD, and implanted into full-thickness skin defects within dorsal skinfold chambers of GFP⁻ C57BL/6 mice. **C:** Enox-treated ad-MVF were exclusively transferred into recipient mice, which received daily s.c. injections of enox from the day of chamber preparation until the end of the *in vivo* experiments. Accordingly, vehicle-treated ad-MVF were exclusively transferred into recipient mice, which received daily injections of vehicle. The matrices were microscopically analyzed on day 0 (day of implantation), 3, 6, 10, and 14. **D:** At the end of the 2-week observation periods, the dorsal skinfold chamber preparations were processed for histological and immunohistochemical analyses.

On day 14, a tail vein bleeding test was performed to confirm the anti-coagulative effect of enox. Thereafter, the mice were sacrificed and the dorsal skinfold chamber preparations were processed for histological and immunohistochemical analyses of microvessel density, collagen content, and epithelialization (Figure 23).

Accordingly, the following groups were investigated in this experimental section:

- Ad-MVF-seeded, vehicle-treated implanted MWD (control group, n = 8)
- Ad-MVF-seeded, enox-treated implanted MWD (n = 8)

5.6. Statistical analyses

All data were first tested for normal distribution and equal variance. Differences between the groups of experimental section 1, 2, 4, and 5 were analyzed by the unpaired Student's t-test (SigmaPlot 11.0; Jandel Corporation, San Rafael, CA, USA). In section 3, differences between the groups were analyzed by ANOVA followed by the Student-Newman-Keuls post hoc test (SigmaPlot) to compensate for the α -error according to Bonferoni probabilities when comparing multiple groups. All values are expressed as mean \pm standard error of the mean (SEM). Statistical significance was accepted for a value of $p < 0.05$.

6. Results

6.1. Characterization of ad-MVF

6.1.1. Length distribution

Epididymal fat pads were separately harvested from GFP⁺ donor animals of 6 different age groups. Interestingly, no significant differences in the available volume of adipose tissue were found between 7 - 12 months old donor animals (Figure 24A). Accordingly, ~ 1.4 mL of such fat tissue could be harvested from all mice for the following isolation of ad-MVF. The isolation process further revealed that ~ 40.000 ad-MVF could be isolated from 1 mL adipose tissue (Figure 24B). Microscopic analyses further showed a comparable average ad-MVF length of ~ 38 μ m in all age groups (Figure 25A). Of interest, ~ 70 % of the isolated ad-MVF from all age groups exhibited an average length of 21 - 50 μ m (Figure 25B).

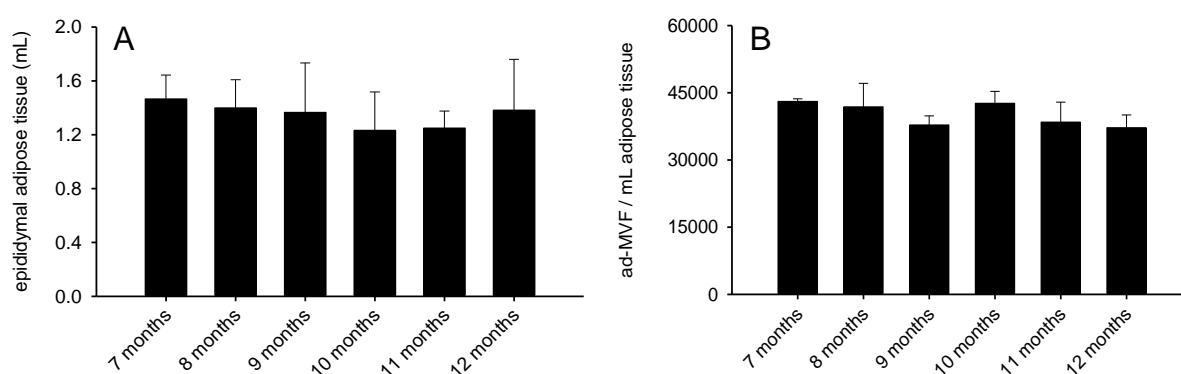


Figure 24. A, B: Volume of available epididymal adipose tissue (mL) (A) and number of isolated ad-MVF (ad-MVF per mL adipose tissue) (B) from 7, 8, 9, 10, 11, and 12 months old GFP⁺ C57BL/6 donor mice ($n = 3$ per group). Mean \pm SEM.

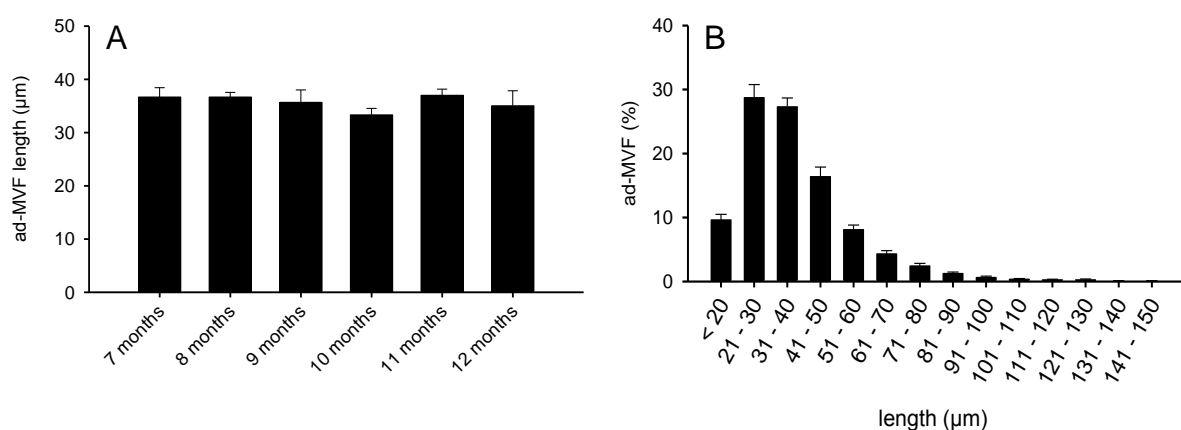


Figure 25. A: Length of ad-MVF (μ m) from 7, 8, 9, 10, 11, and 12 months old GFP⁺ donor mice ($n = 3$ per group). Mean \pm SEM. **B:** Length distribution of ad-MVF (%) from 7-12 months old GFP⁺ C57BL/6 donor mice ($n = 18$). Mean \pm SEM.

6.1.2. Cellular composition

A comparable cellular composition of ad-MVF from donor mice of different ages was revealed by means of flow cytometry. The ad-MVF contained 21 - 30 % CD31⁺ endothelial cells, 15 - 20 % α -SMA⁺ perivascular cells, and 5 - 10 % ASAM⁺ adipocytes as well as 45 - 58 %, 7 - 10 %, and 6 - 11 % cells expressing the stromal/stem cell surface markers CD29, CD117, and CD90, respectively (Table 1).

| Age (months) | CD31 | α -SMA | ASAM | CD29 | CD117 | CD90 |
|--------------|----------------|----------------|---------------|----------------|---------------|----------------|
| 7 | 30.0 \pm 1.8 | 16.1 \pm 1.4 | 9.1 \pm 0.9 | 48.3 \pm 3.6 | 9.1 \pm 1.0 | 7.9 \pm 0.6 |
| 8 | 27.4 \pm 1.6 | 19.8 \pm 1.8 | 5.1 \pm 0.3 | 51.0 \pm 2.5 | 7.2 \pm 1.1 | 6.4 \pm 1.1 |
| 9 | 25.7 \pm 0.9 | 15.5 \pm 1.6 | 7.8 \pm 1.0 | 50.3 \pm 3.7 | 7.1 \pm 0.5 | 7.2 \pm 0.6 |
| 10 | 23.9 \pm 5.1 | 14.8 \pm 2.5 | 9.7 \pm 1.7 | 57.7 \pm 2.8 | 9.8 \pm 1.4 | 10.8 \pm 1.5 |
| 11 | 20.8 \pm 0.5 | 16.4 \pm 2.1 | 8.4 \pm 0.5 | 44.9 \pm 5.1 | 8.0 \pm 0.8 | 6.9 \pm 0.7 |
| 12 | 24.7 \pm 4.7 | 20.1 \pm 1.7 | 6.6 \pm 1.7 | 51.2 \pm 7.4 | 7.9 \pm 1.2 | 8.6 \pm 1.9 |

Table 1. Cellular expression (%) of CD31, α -SMA, ASAM, CD29, CD117, and CD90 in ad-MVF isolated from the epididymal fat pads of 7-12 months old GFP⁺ C57BL/6 donor mice (n = 3 per group), as assessed by flow cytometric analysis. Mean \pm SEM.

6.2. MWD vs. FWM

6.2.1. Non-seeded MWD and FWM

6.2.1.1. Surface morphology

According to 5.2.2., both non-implanted, non-seeded MWD and FWM were first characterized by means of scanning electron microscopy in order to observe possible variations in their surface morphologies due to varying sample preparations. Of interest, this analysis revealed slight differences in the overall morphology of both matrices (Figures 26A-F).

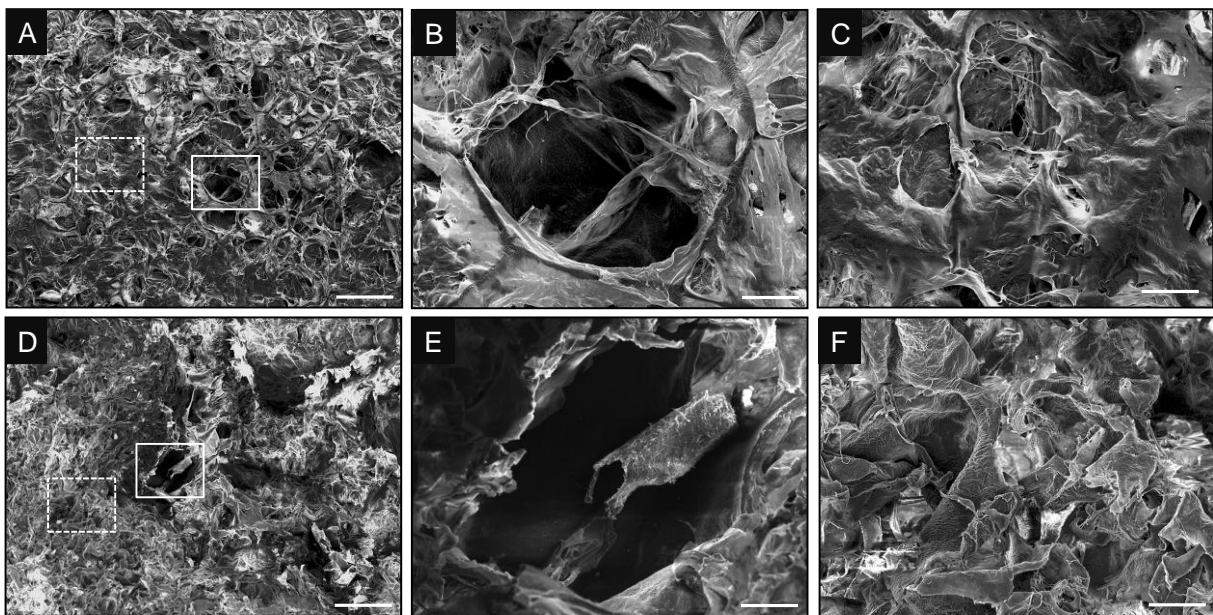


Figure 26. A-F: Scanning electron microscopy of non-seeded, non-implanted MWD (A-C) and FWM (D-F) directly after sample preparation. B, E: Higher magnifications of pore-rich areas (closed frames in A, D) of MWD (B) and FWM (E). C, F: Higher magnifications of areas with low porosity and higher material density (dotted frames in A, D) of MWD (C) and FWM (F) samples. Scale bars: A, D = 150 μm ; B, C, E, F = 25 μm .

Whereas the sheet-like MWD (Figures 26A-C) exhibited a mostly planar surface, the gel-like FWM (Figures 26D-F) presented a more fissured and irregular surface. Although both matrix types showed slight differences in their overall morphology, higher magnifications revealed that the random distribution of pore-rich areas with lower material density (Figures 26B and E) and areas of low porosity and a higher material density (Figures 26C and F) was comparable in both matrices.

To further assess the effect of varying sample preparations on the material properties of MWD and FWM, HE-stained histological sections were analyzed. It could be shown that fiber thickness ($\sim 2 \mu\text{m}$), fiber length ($\sim 120 \mu\text{m}$), and interfiber distance ($\sim 45 \mu\text{m}$) were comparable in both matrices, as quantitatively assessed by means of light microscopy (Figures 27A-E).

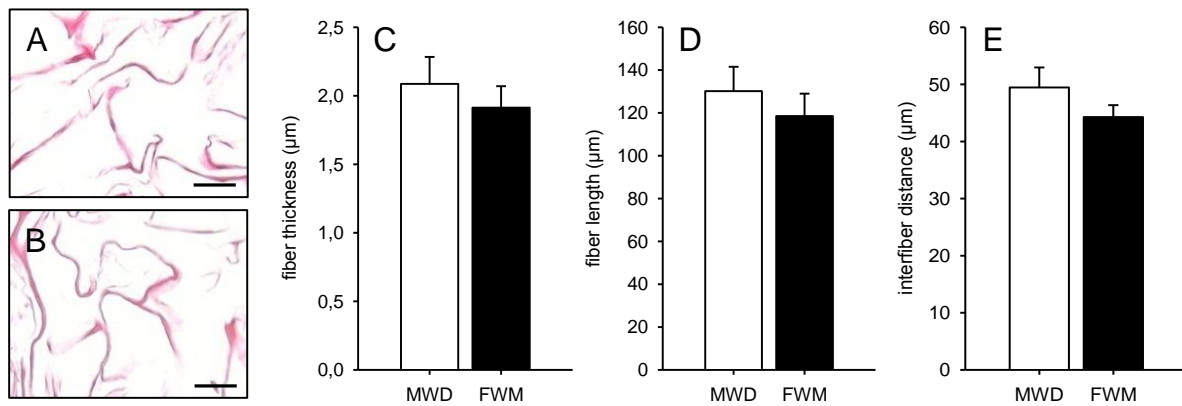


Figure 27. **A, B:** HE-stained sections of MWD (A) and FWM (B) directly after sample preparation. Scale bars = 40 μm . **C-E:** Fiber thickness (μm) (C), fiber length (μm) (D), and interfiber distance (μm) (E) of MWD (white bars, $n = 3$) and FWM (black bars, $n = 3$), as assessed by quantitative histological analyses. Mean \pm SEM.

6.2.1.2. Epithelialization

For *in vivo* analyses, the matrices were implanted into full-thickness skin defects within dorsal skinfold chambers of GFP⁻ C57BL/6 recipient mice and repetitively analyzed for 2 weeks. Epi-illumination stereomicroscopy was used to quantify the epithelialization of MWD and FWM over time (Figures 28A-G). This analysis revealed a comparable epithelialization of both matrices. To further confirm these findings, additional immunohistochemical analyses were performed. These analyses showed that a cytokeratine⁺ epithelial layer covered $29.1 \pm 7.7\%$ (MWD) and $37.8 \pm 6.7\%$ (FWM) of the matrices' surfaces on day 14 after implantation into full-thickness skin defects within dorsal skinfold chambers of C57BL/6 recipient mice (Figures 29A and B).

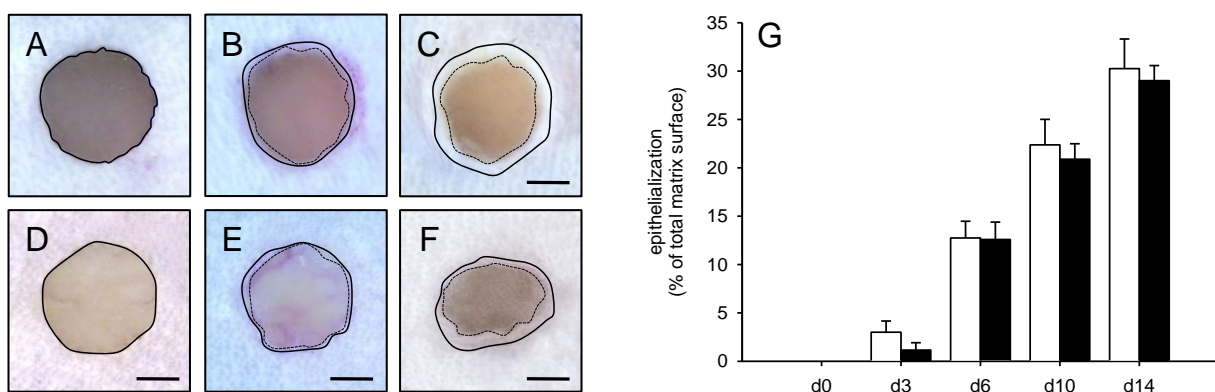


Figure 28. **A-F:** Stereomicroscopic images of full-thickness skin defects in dorsal skinfold chambers of GFP⁻ C57BL/6 recipient mice filled with either MWD (A-C) or FWM (D-F) directly after implantation (A, D) as well as on day 6 (B, E) and 14 (C, F). Closed lines = matrix borders. Dotted lines = non-epithelialized matrix areas. Scale bars = 1.5 mm. **G:** Epithelialization (% of total matrix surface) of implanted MWD (white bars, $n = 8$) and FWM (black bars, $n = 8$), as assessed by planimetric analysis of stereomicroscopic images. Mean \pm SEM.

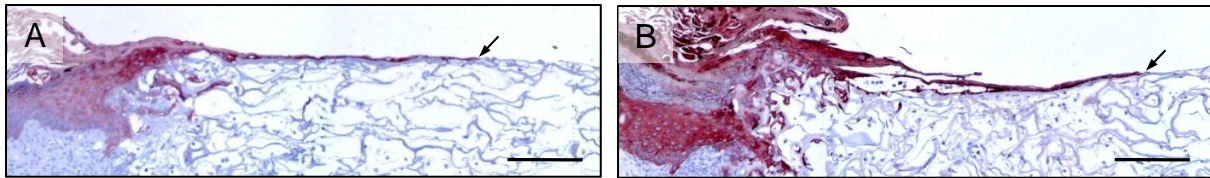


Figure 29. A, B: Immunohistochemical detection of the cytokeratine⁺ epithelial layer (arrows) covering MWD (A) and FWM (B) on day 14 after implantation into full-thickness skin defects within dorsal skinfold chambers of C57BL/6 recipient mice. Scale bars = 145 μm .

6.2.1.3. Vascularization and incorporation

HE-stained sections revealed a comparable ingrowth of vascularized granulation tissue into the pores of MWD and FWM on day 14 after implantation into full-thickness skin defects of C57BL/6 recipient mice (Figures 30A and B). Of interest, the infiltrated granulation tissue was mainly observed in the border zones of both matrices whereas their centers only contained a few migrated single cells. Additionally, a relatively low collagen content was found in both MWD and FWM when compared to normal skin (Figures 31A-D), indicating a rather poor incorporation into the surrounding host tissue on day 14. In line with these findings, only a few CD31⁺ microvessels ($\sim 50 \text{ mm}^{-2}$) were detected inside the pores of both matrices (Figures 32A-C).

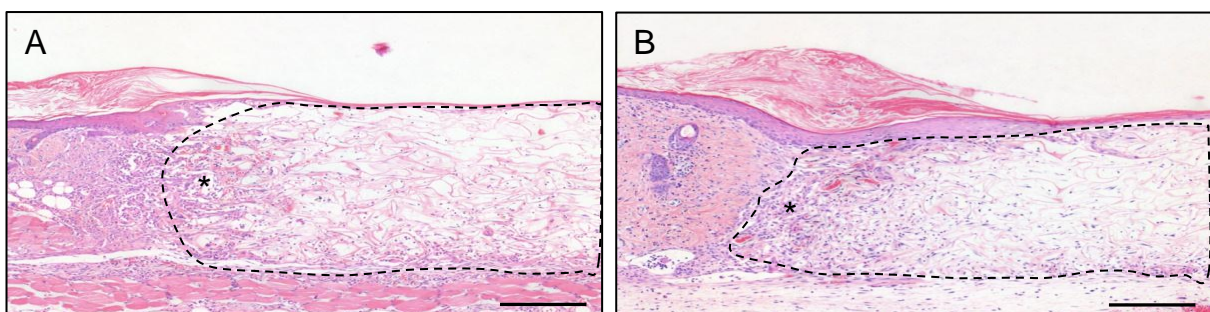


Figure 30. A, B: HE-stained sections of non-seeded MWD (A) and FWM (B) on day 14 after implantation into full-thickness skin defects within dorsal skinfold chambers of C57BL/6 recipient mice. The ingrowth of granulation tissue is found primarily in the border zones of the matrices (A, B; asterisks). Broken lines = matrix borders. Scale bars = 300 μm .

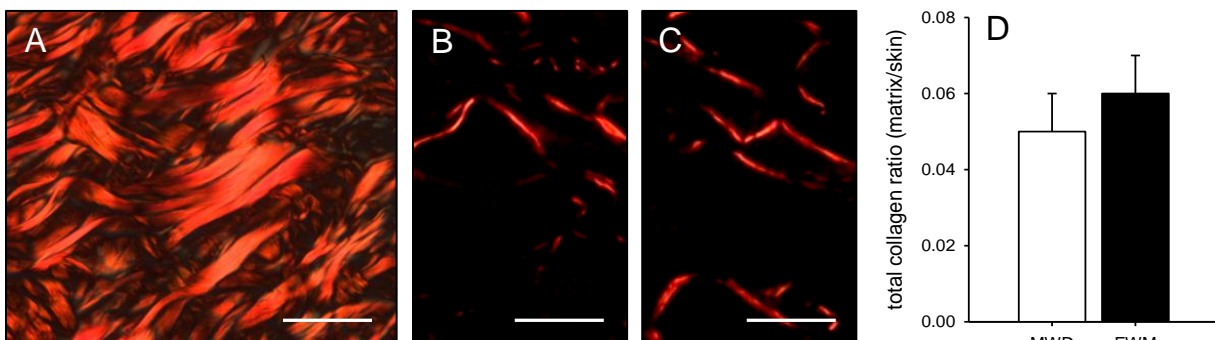


Figure 31. A-C: Sirius red-stained sections of normal skin (A) as well as non-seeded MWD (B) and FWM (C) on day 14 after implantation into full-thickness skin defects within dorsal skinfold chambers of GFP⁻ C57BL/6 recipient mice. Scale bars = 40 μm . **D:** Total collagen ratio (matrix/skin) of implanted MWD (white bars, $n=8$) and FWM (black bars, $n=8$), as assessed by quantitative histological analysis. Mean \pm SEM.

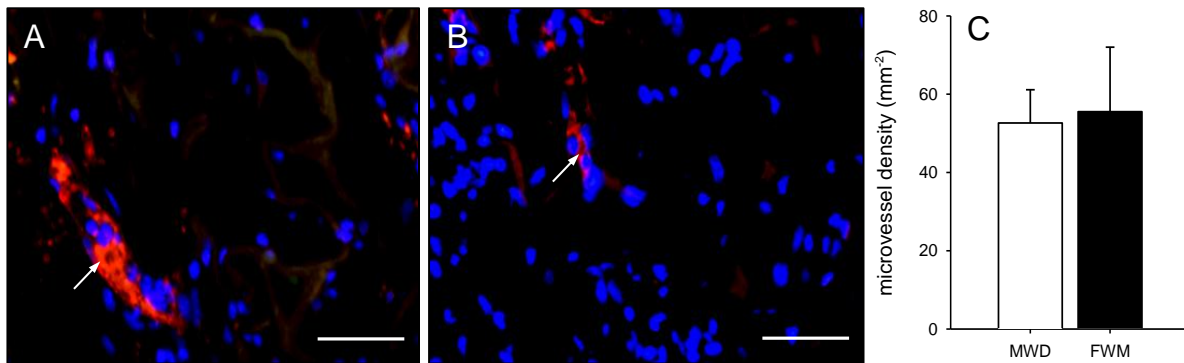


Figure 32. A, B: Immunofluorescent detection of CD31⁺ microvessels (arrows) within MWD (A) and FWM (B) on day 14 after implantation into full-thickness skin defects within dorsal skinfold chambers of C57BL/6 recipient mice. Scale bars = 40 μm. **C:** Microvessel density (mm⁻²) of implanted MWD (white bars, n = 8) and FWM (black bars, n = 8), as assessed by quantitative immunohistochemical analysis. Mean ± SEM.

6.2.1.4. Biocompatibility

Immunohistochemistry was used to assess the number of MPO⁺ neutrophilic granulocytes, MAC387⁺ macrophages, and CD3⁺ lymphocytes infiltrating non-seeded MWD and FWM on day 14 after implantation (Figures 33A-C). All three types of immune cells comparably infiltrated the matrices. Neutrophilic granulocytes represented the majority of the detected immune cells. Their density (~ 200 mm⁻²) was markedly higher when compared to those of infiltrated macrophages (~ 40 mm⁻²) and lymphocytes (~ 10 mm⁻²). These findings indicate a comparable *in vivo* biocompatibility of both matrices.

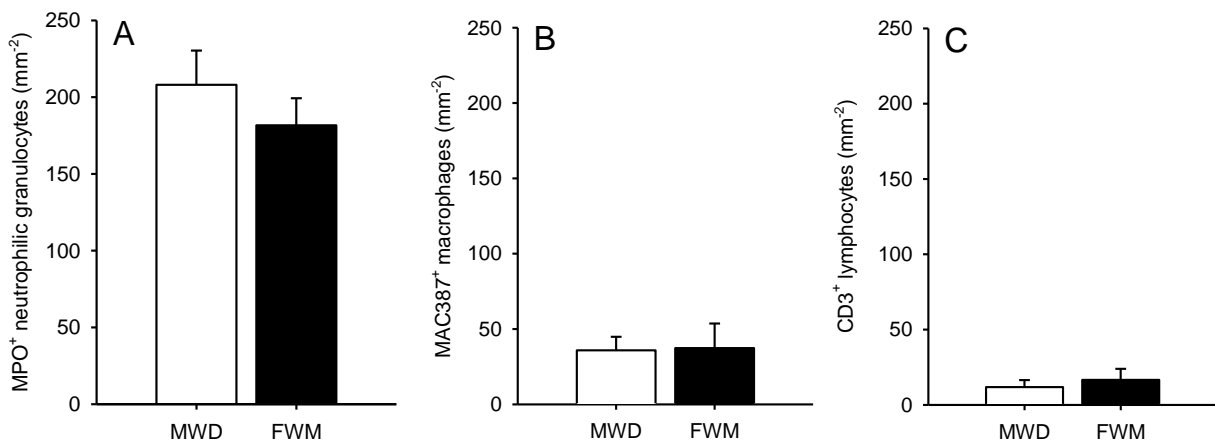


Figure 33. A-C: MPO⁺ neutrophilic granulocytes (mm⁻²) (A), MAC387⁺ macrophages (mm⁻²) (B), and CD3⁺ lymphocytes (mm⁻²) (C) within MWD (white bars, n = 8) and FWM (black bars, n = 8) on day 14 after implantation into full-thickness skin defects within dorsal skinfold chambers of GFP⁻ C57BL/6 recipient mice, as assessed by quantitative immunohistochemical analysis. Mean ± SEM.

6.2.2. Ad-MVF-seeded MWD and FWM

6.2.2.1. Ad-MVF distribution

As a flowable matrix, FWM may allow a more homogeneous distribution of ad-MVF during sample preparation when compared to MWD. To test this hypothesis, MWD and FWM samples were seeded with an identical number of ~ 15,000 ad-MVF. Of interest, HE-stained sections (Figures 34A and B) of the matrices revealed that the ad-MVF were exclusively localized on the surface of MWD whereas ad-MVF in FWM exhibited a more homogeneous distribution. To further confirm these findings, the distribution of CD31⁺ microvessels (Figures 34C and D) was assessed throughout the entire matrix. The calculated cv of the microvessel density was lower within FWM (Figure 34E) when compared to MWD. Accordingly, the inter-fragment distance, i.e. the distance in between individual ad-MVF, was 15-fold higher in FWM when compared to MWD (Figure 34F).

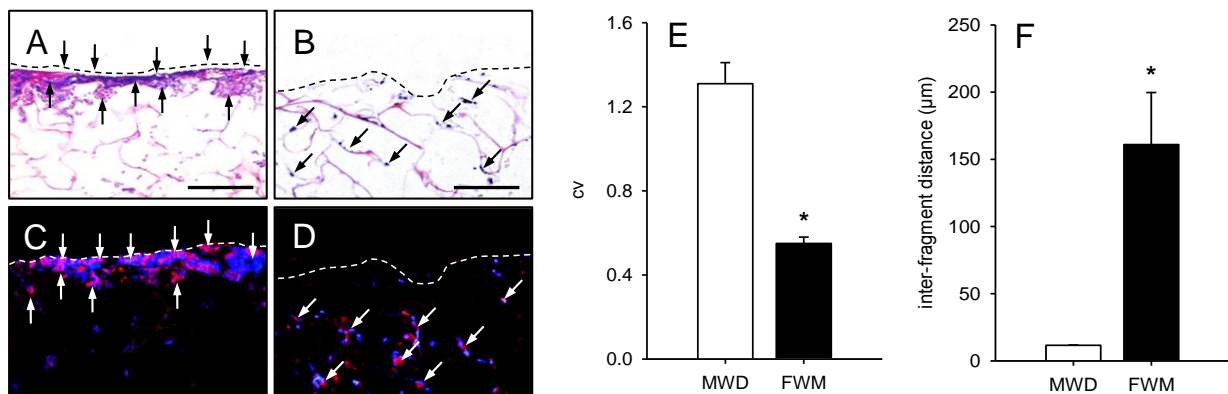


Figure 34. **A-D:** HE-stained and immunofluorescent sections of MWD (A, C) and FWM (B, D) directly after seeding within ad-MVF. Broken line = matrix border. Arrows = ad-MVF. The immunofluorescent sections were stained with an antibody against CD31 (C, D; red) and Hoechst 33342 (C, D; blue). Scale bars = 100 μm. **E, F:** Cv (E) and inter-fragment distance (μm) (F) of ad-MVF-seeded MWD (white bars; n = 3) and FWM (black bars; n = 3). Mean ± SEM. *p < 0.05 vs. MWD.

6.2.2.2. Vascularization and incorporation

The dorsal skinfold chamber model was used to repetitively analyze the *in vivo* vascularization and incorporation of ad-MVF-seeded MWD and FWM by means of intravital fluorescence microscopy. The analysis of both matrices revealed that seeded ad-MVF reassembled into new microvascular networks and formed interconnections with the microvasculature of the surrounding host tissue. This resulted in an early onset of blood perfusion (Figures 35A-F) on day 3 after implantation. Interestingly, both kinetics and extent of this process were significantly diminished in ad-MVF-seeded FWM. When compared to ad-MVF-seeded MWD, FWM exhibited a reduced number of perfused ROIs between day 10 and 14 as well as a lower functional microvessel density on day 14 (Figures 35G and H). Analyzed microhemodynamic parameters in both groups revealed a decreasing diameter of blood-perfused microvessels over time. Furthermore, both centerline RBC velocity and wall

shear rate progressively increased in microvessels of ad-MVF-seeded MWD and FWM (Table 2).

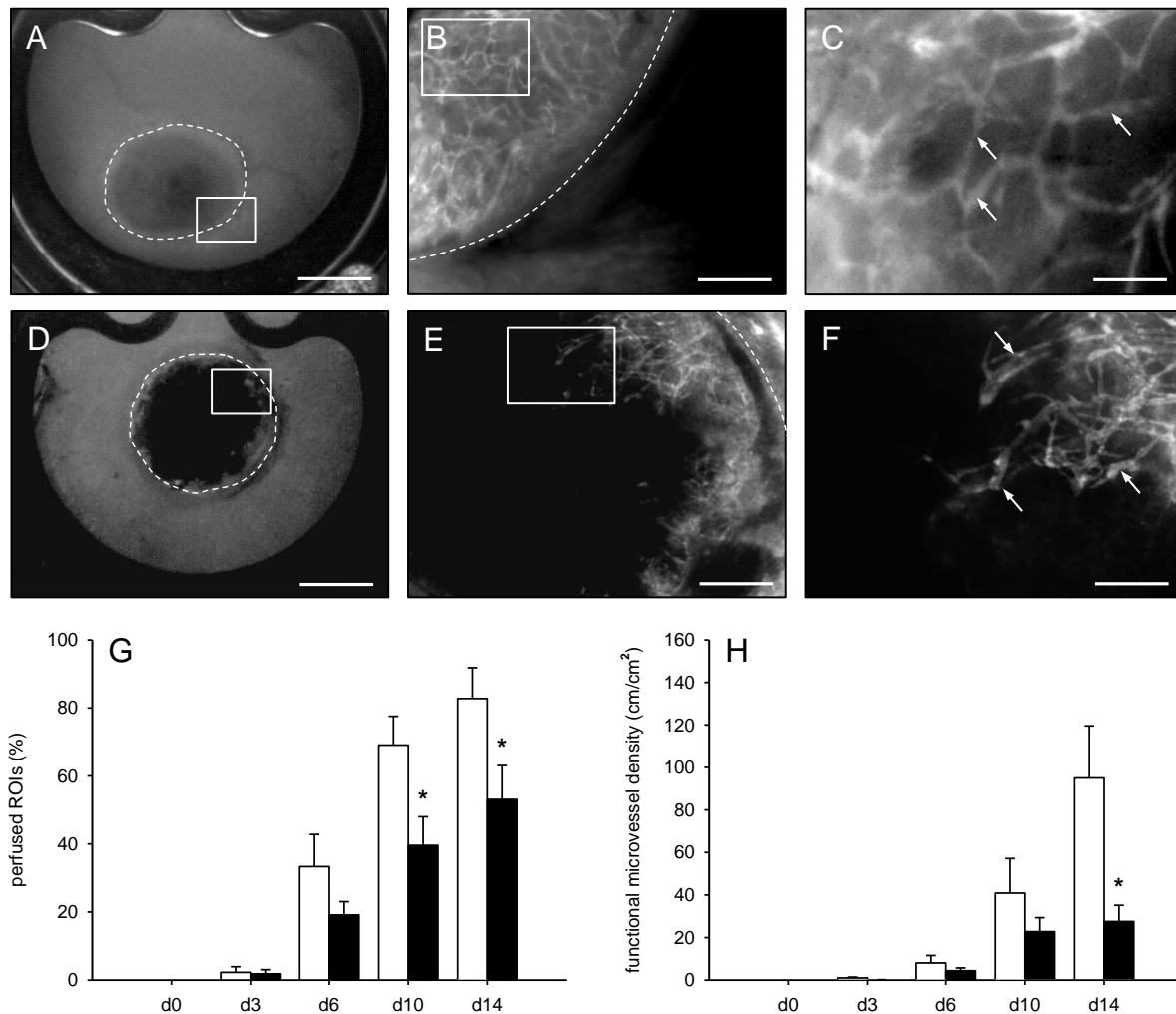


Figure 35. **A-F:** Intravital fluorescence microscopy (blue light epi-illumination with 5 % FITC-labeled dextran 150,000 i.v.) of implanted, ad-MVF-seeded MWD (A-C) and FWM (D-F) on day 14 after implantation into full-thickness skin defects within dorsal skinfold chambers of GFP⁺ C57BL/6 recipient mice. Broken line = matrix border. Arrows = perfused microvessels. B, E = inserts in A, D. C, F = inserts in B, E. Scale bars: A, D = 2 mm; B, E = 400 μ m; C, F = 100 μ m. **G, H:** Perfused ROIs (%) (G) and functional microvessel density (cm/cm²) (H) of ad-MVF-seeded MWD (white bars; n = 8) and FWM (black bars; n = 8). Mean \pm SEM. *p < 0.05 vs. MWD.

Although not proven to be significant at each time point, the diameter, centerline RBC velocity, and wall shear rate of microvessels within FWM were reduced when compared to MWD (Table 2). After 14 days, analyses of HE-stained sections showed that all pores of ad-MVF-seeded MWD were completely filled with a dense vascularized granulation tissue whereas FWM only contained a few infiltrated single cells within its center zones (Figures 36A-D). Additional immunohistochemical analyses revealed that ad-MVF-seeded FWM contained a significantly lower number of CD31⁺ microvessels (\sim 120 mm⁻²) when compared to MWD (\sim 210 mm⁻²) (Figures 37A-C). CD31/GFP co-staining revealed that \sim 93 % and \sim 80 % of all detected microvessels in MWD and FWM originated from GFP⁺ ad-MVF (Figures

38A-D).

| | d0 | d3 | d6 | d10 | d14 |
|---|----|------------------|-------------------|------------------|------------------|
| <i>Diameter (μm)</i> | | | | | |
| MWD | - | 27.5 \pm 8.6 | 27.4 \pm 2.6 | 22.3 \pm 2.7 | 18.1 \pm 1.5 |
| FWM | - | 23.3 \pm 5.2 | 32.9 \pm 5.4 | 16.8 \pm 0.1* | 14.7 \pm 0.9 |
| <i>Centerline RBC velocity ($\mu\text{m/s}$)</i> | | | | | |
| MWD | - | 150.6 \pm 65.9 | 428.9 \pm 111.8 | 696.4 \pm 66.0 | 643.3 \pm 79.2 |
| FWM | - | 62.5 \pm 25.5 | 101.1 \pm 37.6 | 420.3 \pm 89.7 | 461.9 \pm 60.7 |
| <i>Wall shear rate (s^{-1})</i> | | | | | |
| MWD | - | 59.6 \pm 21.5 | 136.4 \pm 42.7 | 268.7 \pm 37.4 | 292.9 \pm 51.6 |
| FWM | - | 19.7 \pm 7.8 | 25.8 \pm 11.2* | 203.3 \pm 44.4 | 250.5 \pm 24.3 |

Table 2. Diameter (μm), centerline RBC velocity ($\mu\text{m/s}$), and wall shear rate (s^{-1}) of blood vessels within ad-MVF-seeded MWD and FWM directly (d0) as well as on day 3, 6, 10, and 14 after implantation into full-thickness skin defects within dorsal skinfold chambers of GFP⁻ C57BL/6 recipient mice. Mean \pm SEM. * $p < 0.05$ vs. MWD.

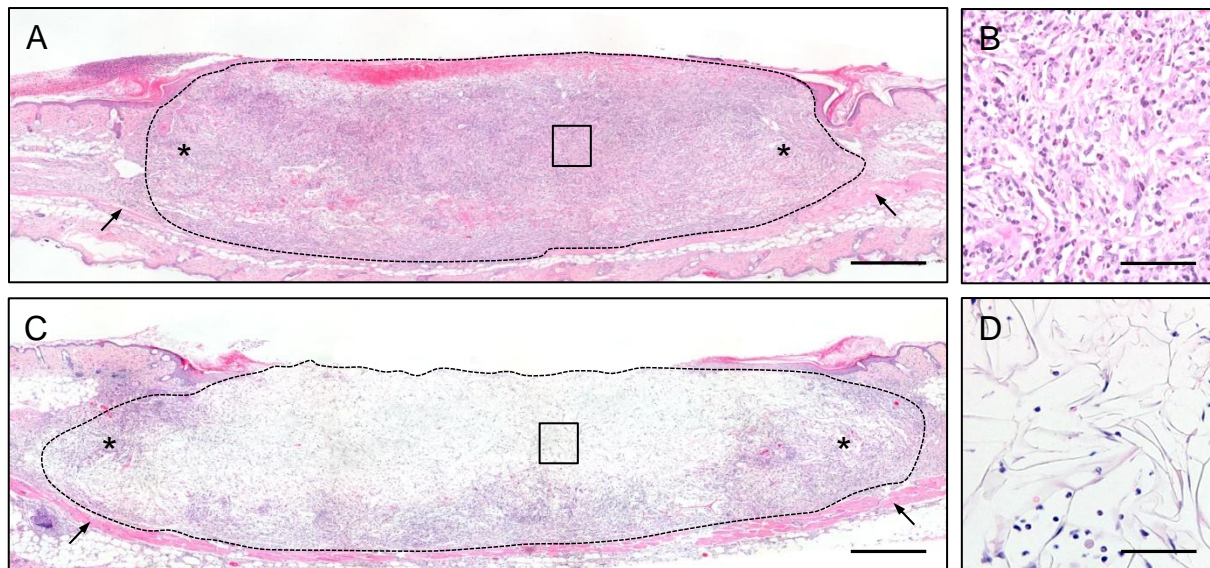


Figure 36. A-D: HE-stained sections of ad-MVF-seeded MWD (A, B) and FWM (C, D) on day 14 after implantation into full-thickness skin defects within dorsal skinfold chambers of GFP⁻ C57BL/6 recipient mice. Broken lines = matrix borders. Asterisks = border zones. Arrows = panniculus carnosus muscle of the dorsal skinfold chamber preparation. B, D = insert in A, C. Scale bars: A, C = 350 μm ; B, D = 50 μm .

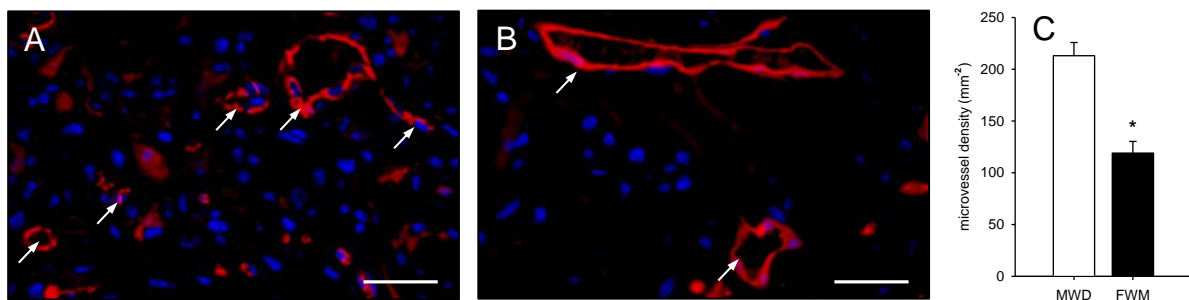


Figure 37. A, B: Immunohistochemical detection of CD31⁺ microvessels (arrows) in ad-MVF-seeded MWD (A) and FWM (B) on day 14 after implantation into full-thickness skin defects within dorsal skinfold chambers of GFP⁻ C57BL/6 recipient mice. Scale bars = 30 μm . **C:** Microvessel density (mm^{-2}) of ad-MVF-seeded MWD (white bar; $n = 8$) and FWM (black bar; $n = 8$). Mean \pm SEM. * $p < 0.05$ vs. MWD.

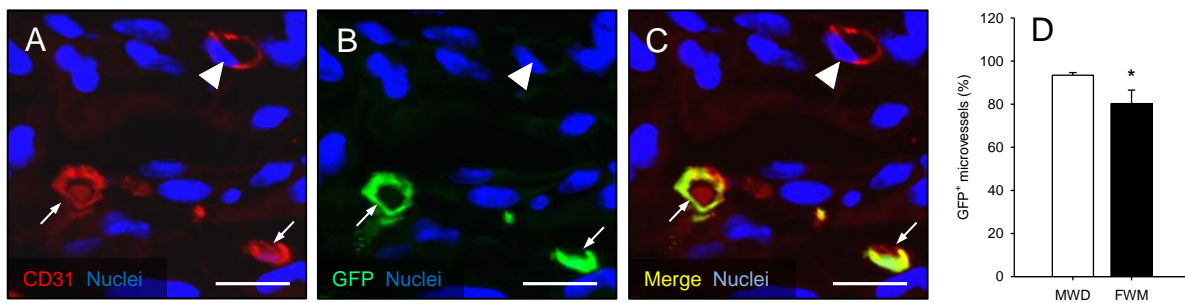


Figure 38. **A, B:** Immunohistochemical detection of microvessels in ad-MVF-seeded FWM on day 14 after implantation into full-thickness skin defects within dorsal skinfold chambers of GFP⁻ C57BL/6 recipient mice. Arrows = CD31⁺ (red) / GFP⁺ (green) microvessels. Arrowhead = CD31⁺ / GFP⁻ microvessel. **C:** Merge of A and B. Scale bars = 15 μ m. **D:** GFP⁺ microvessels (%) in ad-MVF-seeded MWD (white bar; n = 8) and FWM (black bar; n = 8). Mean \pm SEM. *p < 0.05 vs. MWD.

Additional Sirius red-staining was used to detect mature collagen type I fibers by their reddish appearance under polarized light. This analysis revealed a lower collagen ratio in FWM when compared to MWD (Figures 39A-D).

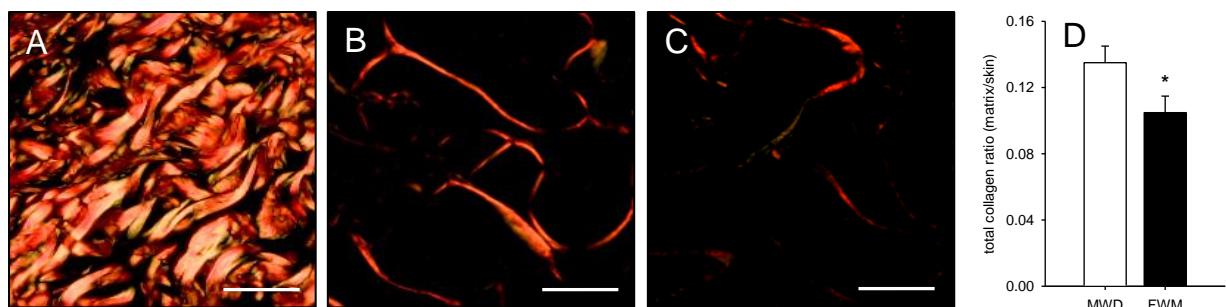


Figure 39. **A-C:** Sirius red-stained sections of normal skin (A) as well as ad-MVF-seeded MWD (B) and FWM (C) on day 14 after implantation into full-thickness skin defects within dorsal skinfold chambers of GFP⁻ C57BL/6 recipient mice. Scale bars = 125 μ m. **D:** Total collagen ratio (matrix/skin) of ad-MVF-seeded MWD (white bar; n = 8) and FWM (black bar; n = 8). Mean \pm SEM. *p < 0.05 vs. MWD.

6.2.2.3. Epithelialization

Repetitive epi-illumination microscopy showed a diminished epithelialization of FWM between day 6 and 14 when compared to MWD (Figures 40A-G). Immunohistochemical detection of the cytokeratine⁺ epithelial layer further revealed that 74.0 \pm 13.5 % of the MWD surface was covered with a cytokeratine⁺ epithelial layer, whereas only 39.9 \pm 4.3 % of the FWM surface exhibited an epithelial coverage on day 14 after implantation into full-thickness skin defects within dorsal skinfold chambers of GFP⁻ C57BL/6 recipient mice (Figures 41A and B).

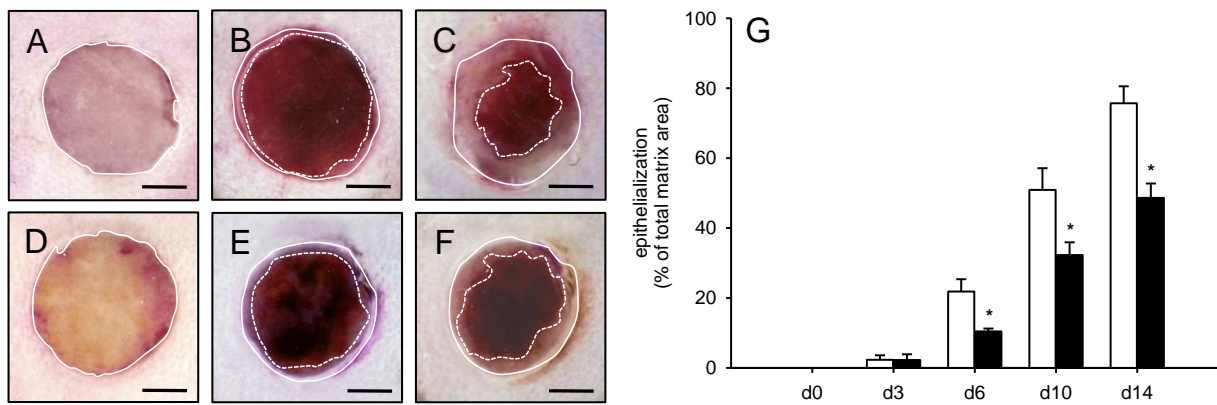


Figure 40. A-F: Stereomicroscopic images of full-thickness skin defects in dorsal skinfold chambers of GFP⁻ C57BL/6 mice filled with either ad-MVF-seeded MWD (A-C) or FWM (D-F) directly after implantation (A, D) as well as on day 6 (B, E) and 14 (C, F). Closed lines = matrix borders. Dotted lines = non-epithelialized areas. Scale bars = 1.5 mm. **G:** Epithelialization (% of total matrix area) of implanted ad-MVF-seeded MWD (white bars; n = 8) and FWM (black bars; n = 8). Mean ± SEM. *p < 0.05 vs. MWD.

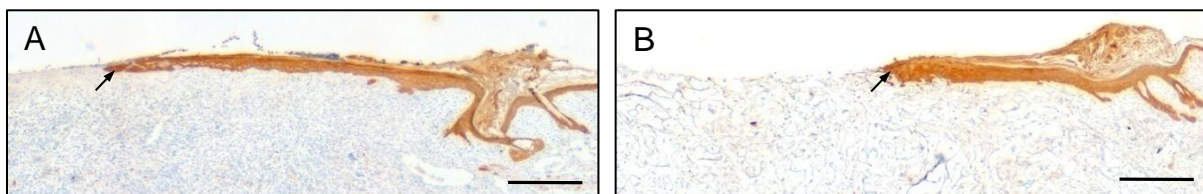


Figure 41. A, B: Immunohistochemical detection of the cytokeratine⁺ epithelial layer (arrows) covering MWD (A) and FWM (B) on day 14 after implantation into full thickness skin defects within dorsal skinfold chambers of GFP⁻ C57BL/6 recipient mice. Scale bars = 145 μm.

6.2.2.4. Apoptotic cell death and proliferation

Immunohistochemical analyses further revealed that ad-MVF-seeded FWM contained a significantly higher number of cleaved caspase-3⁺ apoptotic cells (5.3 ± 0.8 %) as well as a lower number of proliferating Ki67⁺ cells (48.8 ± 21.6 %) when compared to ad-MVF-seeded MWD (3.1 ± 1.0 % and 81.1 ± 2.0 %) on day 6 (Figures 42A-D).

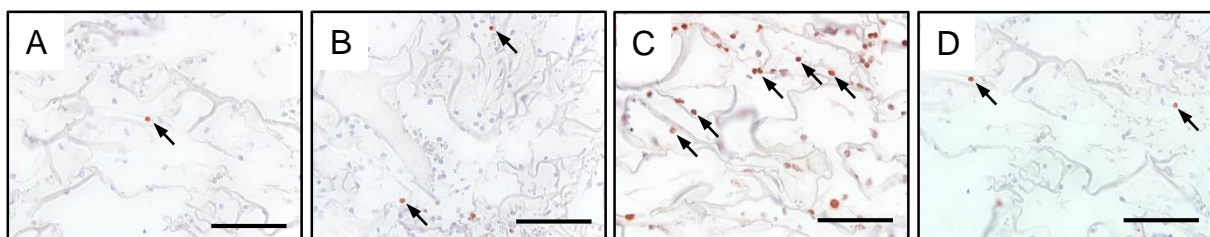


Figure 42. A-D: Immunohistochemical detection of apoptotic cleaved caspase-3⁺ (A, B; arrows) and proliferating Ki67⁺ cells (C, D; arrows) in ad-MVF-seeded MWD (A, C) and FWM (B, D) on day 6 (A, C) and 14 (B, D) after implantation into full-thickness skin defects within dorsal skinfold chambers of GFP⁻ C57BL/6 recipient mice. Scale bars = 50 μm.

However, at the end of the 14-day observation period, both matrices exhibited comparable numbers of 1.5 ± 0.3 % (MWD) and 1.2 ± 0.1 % (FWM) cleaved caspase-3⁺ apoptotic cells as well as 10.4 ± 1.3 % (MWD) and 11.7 ± 2.1 % (FWM) Ki67⁺ proliferating cells.

6.3. Ad-MVF seeding density

6.3.1. Vascularization and incorporation

In this experimental section, MWD was seeded with three different densities (HD, MD, LD) of GFP⁺ ad-MVF to determine the lowest density needed to maintain a sufficient vascularization and incorporation of the matrix. Full-thickness skin defects within dorsal skinfold chambers of GFP⁻ C57BL/6 mice were filled with the seeded MWD to repetitively visualize and analyze its vascularization by means of intravital fluorescence microscopy over time (Figures 43A-I). In all groups, an onset of blood perfusion was detected on day 6 after implantation (Figure 43J). Throughout the observation time of 14 days, the density of perfused microvessels continuously increased (Figure 43K). This was associated with typical signs of vascular maturation and remodeling, i.e. the reduction of diameters as well as the increase of centerline RBC velocities and wall shear rates of individual microvessels within the matrices (Table 3).

| | d0 | d3 | d6 | d10 | d14 |
|---|----|----|------------------|------------------|-------------------|
| <i>Diameter (μm)</i> | | | | | |
| HD | - | - | 31.5 \pm 1.0 | 23.5 \pm 1.7 | 17.2 \pm 1.2 |
| MD | - | - | 31.7 \pm 1.8 | 24.1 \pm 1.5 | 19.5 \pm 1.4 |
| LD | - | - | 28.9 \pm 0.5 | 22.5 \pm 0.6 | 21.2 \pm 0.9 |
| <i>Centerline RBC velocity ($\mu\text{m/s}$)</i> | | | | | |
| HD | - | - | 229.2 \pm 51.0 | 450.5 \pm 58.5 | 497.6 \pm 78.9 |
| MD | - | - | 176.2 \pm 53.5 | 419.6 \pm 78.3 | 438.8 \pm 100.9 |
| LD | - | - | 148.1 \pm 50.7 | 302.5 \pm 36.1 | 392.4 \pm 66.8 |
| <i>Wall shear rate (s^{-1})</i> | | | | | |
| HD | - | - | 58.8 \pm 13.0 | 141.0 \pm 17.8 | 243.2 \pm 47.8 |
| MD | - | - | 42.6 \pm 11.8 | 137.5 \pm 20.6 | 187.9 \pm 45.1 |
| LD | - | - | 41.0 \pm 13.8 | 151.2 \pm 30.3 | 151.2 \pm 30.3 |

Table 3. Diameter (μm), centerline RBC velocity ($\mu\text{m/s}$), and wall shear rate (s^{-1}) of microvessels in HD ($n = 8$), MD ($n = 8$), and LD ($n = 8$) ad-MVF-seeded MWD on day 6, 10, and 14 after implantation into full-thickness skin defects within dorsal skinfold chambers of GFP⁻ C57BL/6 recipient mice, as assessed by intravital fluorescence microscopy and computer-assisted image analysis. Mean \pm SEM.

The process of vascularization was comparable in HD and MD ad-MVF-seeded matrices. Furthermore, no significant differences in morphological and microhemodynamic parameters were detected between the groups (Figures 43J and K, Table 3). LD ad-MVF-seeded matrices, on the other hand, showed a rather weak vascularization with lower numbers of perfused ROIs and a diminished functional microvessel density between day 6 and 14 (Figures 43J and K). Matrix-induced hemorrhages correlated with the extent of vascularization and could be mainly seen during the early phase of microvascular network formation on day 6. Of interest, the hemorrhagic score of HD and MD ad-MVF-seeded MWD was higher on day 6 and 10 when compared to LD ad-MVF-seeded MWD.

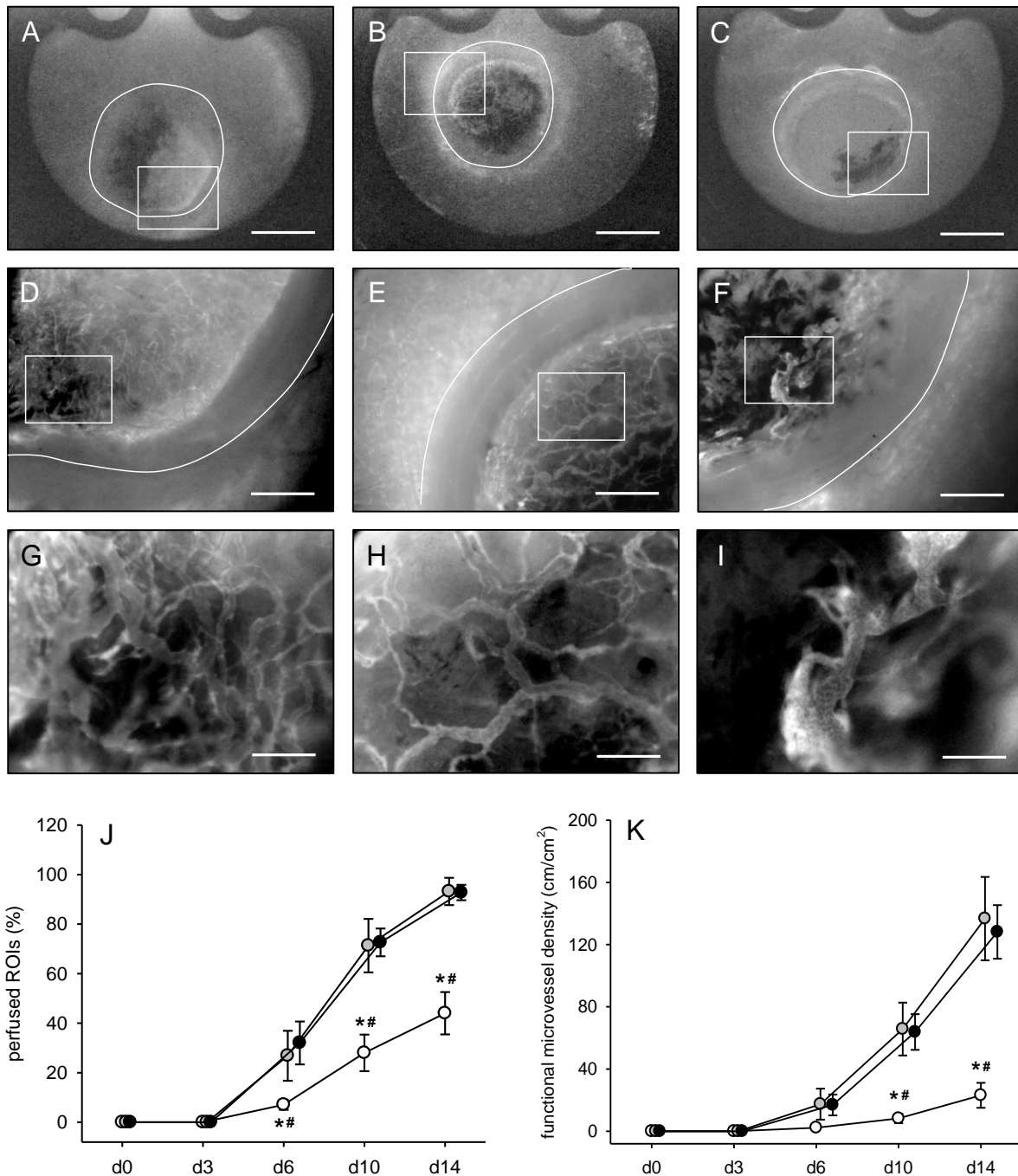


Figure 43. A-I: Intravital fluorescence microscopy (blue light epi-illumination, 5 % FITC-labeled dextran) of HD (A, D, G), MD (B, E, H), and LD (C, F, I) ad-MVF-seeded MWD on day 14 after implantation into full-thickness skin defects within dorsal skinfold chambers of GFP C57BL/6 mice. A-C = overview of the chamber observation window. D-F = higher magnification of inserts in A-C. G-I = higher magnification of inserts in D-F. Note that the HD and MD ad-MVF-seeded matrices exhibit an improved vascularization when compared to LD ad-MVF-seeded ones. Scale bars: A-C = 2.5 mm; D-F = 500 μ m; G-I = 125 μ m. **J, K:** Perfused ROIs (%) (J) and functional microvessel density (cm/cm^2) (K) of HD (black circles, $n = 8$), MD (grey circles, $n = 8$), and LD (white circles, $n = 8$) ad-MVF-seeded MWD, as assessed by intravital fluorescence microscopy and computer-assisted image analysis. Means \pm SEM. * $p < 0.05$ vs. HD ad-MVF-seeded MWD; # $p < 0.05$ vs. MD ad-MVF-seeded MWD.

Additional photoacoustic imaging was used to first detect oxygenation of ad-MVF-seeded matrices *in vitro* immediately after their seeding (Figures 44A-F). According to the different seeding densities, LD ad-MVF-seeded, non-implanted matrices contained significantly lower

sO₂ levels when compared to HD ad-MVF-seeded samples (Figure 44G). Fourteen days after implantation, the oxygenation levels were markedly increased when compared to those directly after seeding. Noteworthy, LD ad-MVF-seeded matrices exhibited reduced sO₂ levels when compared to HD ad-MVF-seeded matrices (Figures 44H-M). In line with the intravital microscopic findings, MD and HD groups were comparable (Figures 44G and N).

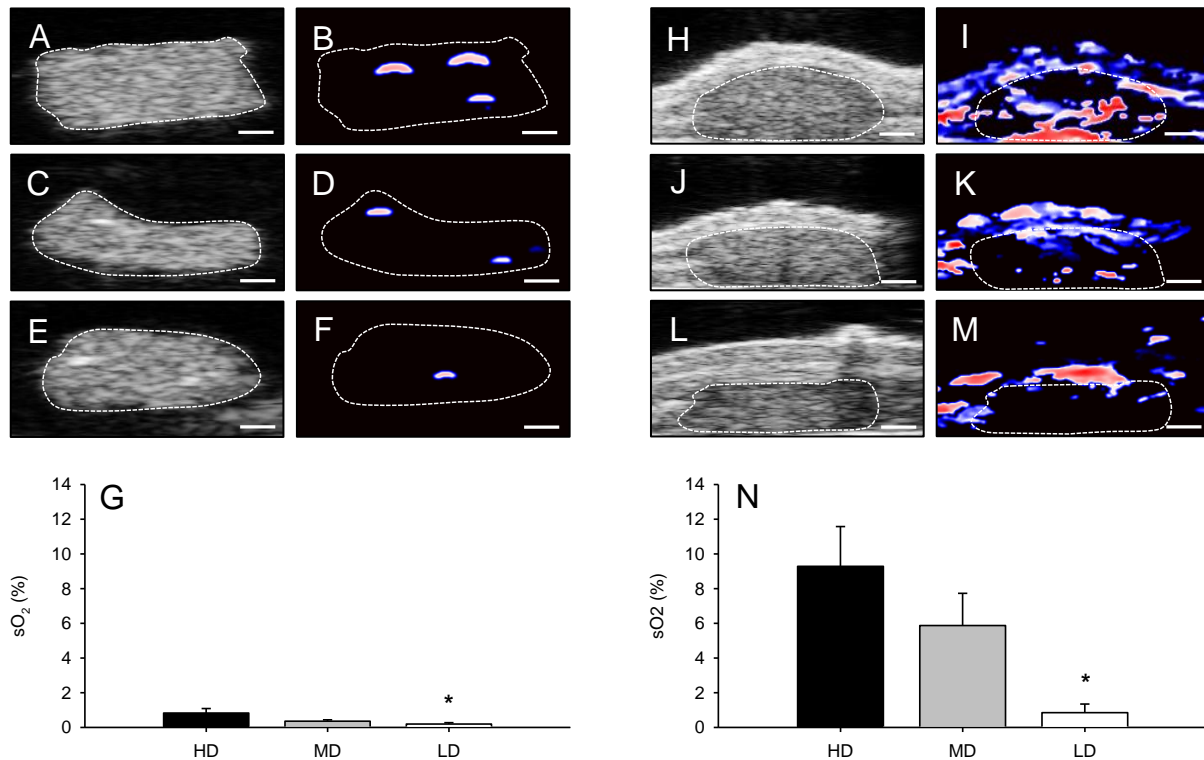


Figure 44. **A-F:** B-mode ultrasound (A, C, E) and photoacoustic imaging (B, D, F) of freshly HD (A, B), MD (C, D) and LD (E, F) ad-MVF-seeded MWD directly after the seeding procedure. Scale bars = 600 μ m. Red areas = high oxygenation. Blue areas = low oxygenation. **G:** sO₂ (%) within freshly HD (black bar, n = 3), MD (grey bar, n = 3), and LD (white bar, n = 3) ad-MVF-seeded MWD. **H-M:** B-mode ultrasound (H, J, L) and photoacoustic imaging (I, K, M) of HD (H, I), MD (J, K) and LD (L, M) ad-MVF-seeded MWD on day 14 after implantation into full-thickness skin defects within dorsal skinfold chambers of GFP⁺ C57BL/6 recipient mice. Red areas = high oxygenation. Blue areas = low oxygenation. Black areas = no oxygenation. Scale bars = 600 μ m. **N:** sO₂ (%) within HD (black bar, n = 3), MD (grey bar, n = 3), and LD (white bar, n = 3) ad-MVF-seeded MWD on day 14 after implantation. Means \pm SEM. *p < 0.05 vs. HD ad-MVF-seeded MWD.

On day 14 after implantation, HE-stained sections revealed that LD ad-MVF-seeded matrices exhibited a dense vascularization exclusively in the border zones and only a few invaded single cells in their center (Figures 45E and F). In contrast, HD and MD ad-MVF-seeded matrices exhibited a dense vascularized granulation tissue throughout the entire matrix (Figures 45A-D). Additional analyses of Sirius red-stained sections showed that LD ad-MVF-seeded matrices contained a reduced amount of mature collagen fibers when compared to HD and MD ad-MVF-seeded matrices (Figures 45G-K).

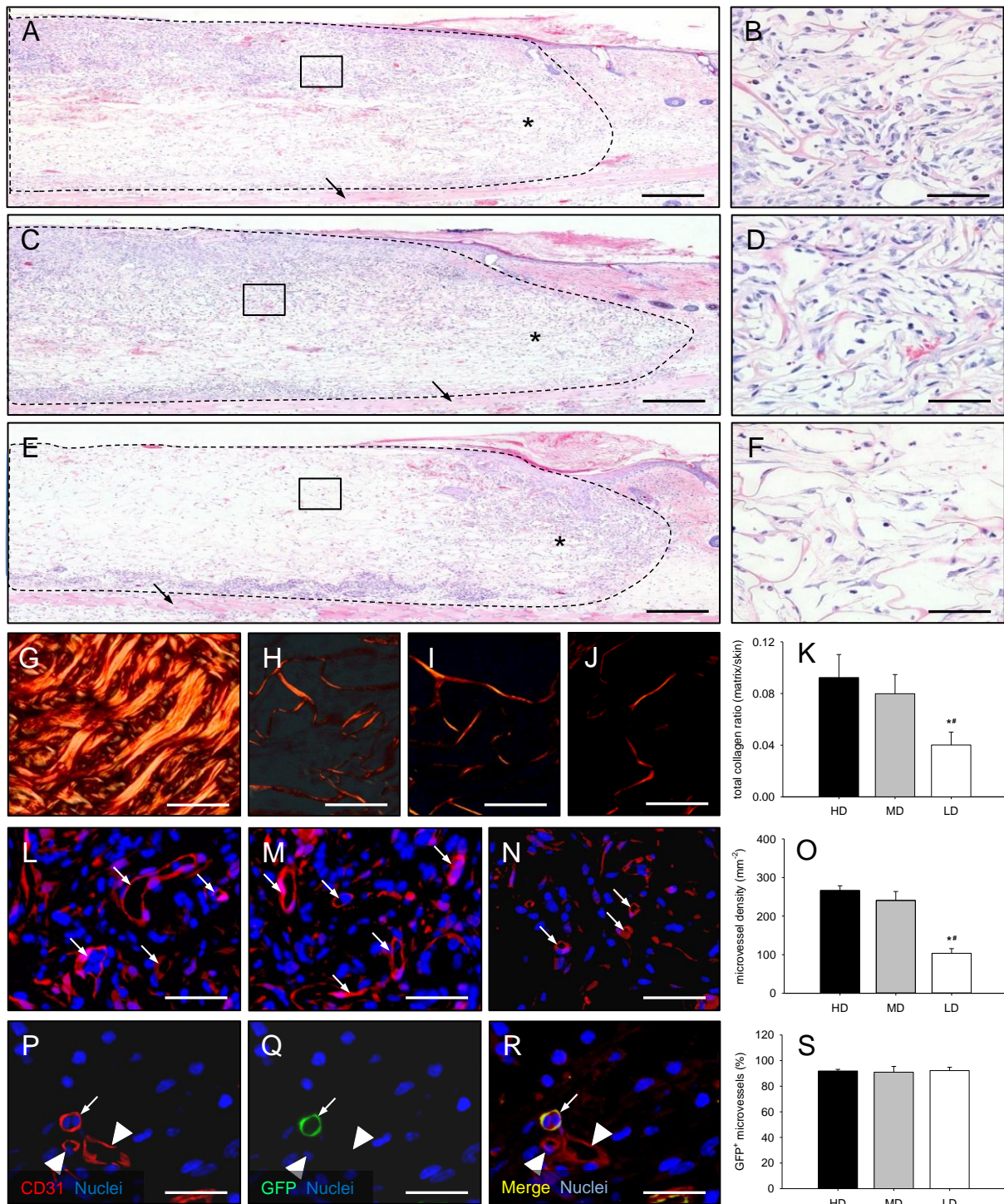


Figure 45. **A-F:** HE-stained sections of HD (A, B), MD (C, D), and LD (E, F) ad-MVF-seeded MWD on day 14 after implantation into full-thickness skin defects within dorsal skinfold chambers of GFP⁻ C57BL/6 mice. Broken lines = matrix borders. Asterisks = border zones. Arrows = panniculus carnosus muscle. B, D, F = inserts in A, C, E. Scale bars A, C, E = 200 μ m; B, D, F = 50 μ m. **G-J:** Sirius red-stained sections of normal skin (G) as well as HD (H), MD (I), and LD (J) ad-MVF-seeded MWD. Scale bars = 45 μ m. **K:** Total collagen ratio (matrix/skin) within HD (black bar, n = 8), MD (grey bar, n = 8) and LD (white bar, n = 8) ad-MVF-seeded MWD. Means \pm SEM. **p* < 0.05 vs. HD ad-MVF-seeded MWD; #*p* < 0.05 vs. MD ad-MVF-seeded MWD. **L-N:** CD31⁺ microvessels (arrows) in HD (L), MD (M), and LD (N) ad-MVF-seeded matrices. Scale bars = 45 μ m. **O:** Microvessel density (mm⁻²) within HD (black bar, n = 8), MD (grey bar, n = 8), and LD (white bar, n = 8) ad-MVF-seeded MWD. Means \pm SEM. **p* < 0.05 vs. HD ad-MVF-seeded MWD; #*p* < 0.05 vs. MD ad-MVF-seeded MWD. **P-R:** CD31⁺/GFP⁺ microvessel (arrow) in a HD ad-MVF-seeded MWD. Arrowheads = CD31⁺/GFP⁻ microvessels. Scale bars = 45 μ m. **S:** GFP⁺ microvessels (%) within HD (black bar, n = 8), MD (grey bar, n = 8) and LD (white bar, n = 8) ad-MVF-seeded MWD. Means \pm SEM.

In line with the intravital fluorescence microscopic findings, the density of CD31⁺ microvessels was significantly reduced in LD ad-MVF-seeded matrices when compared to HD and MD ad-MVF-seeded matrices (Figures 45L-O). Furthermore, the immunohistochemical detection of CD31⁺/GFP⁺ vessels revealed that ~ 90 % of all microvessels originated from the GFP⁺ ad-MVF in all three experimental groups (Figures 45P-S).

6.3.2. Immune cell infiltration

Immunohistochemical detection of MPO⁺ neutrophilic granulocytes, CD68⁺ macrophages, and CD3⁺ lymphocytes (Figures 46A-C) showed that the infiltration of all three immune cell types was markedly reduced in LD ad-MVF-seeded matrices when compared to HD and MD ad-MVF-seeded matrices.

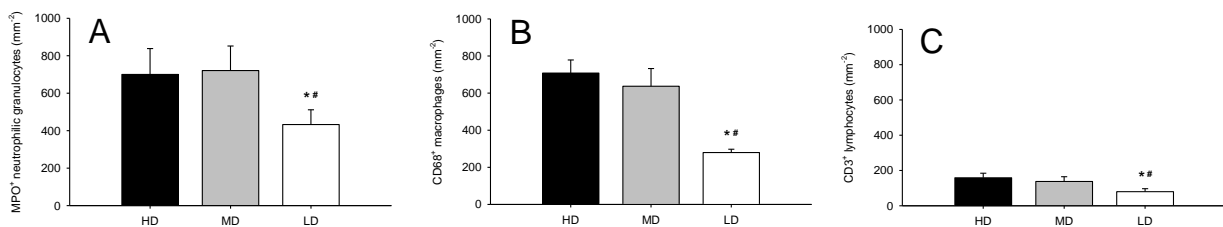


Figure 46. A-C: MPO⁺ neutrophilic granulocytes (mm⁻²) (A), CD68⁺ macrophages (mm⁻²) (B), and CD3⁺ lymphocytes (mm⁻²) (C) within HD (black bars, n = 8), MD (grey bars, n = 8), and LD (white bars, n = 8) ad-MVF-seeded MWD on day 14 after implantation into full-thickness skin defects within dorsal skinfold chambers of GFP⁺ C57BL/6 mice. Means ± SEM. *p < 0.05 vs. HD ad-MVF-seeded MWD; #p < 0.05 vs. MD ad-MVF-seeded MWD.

6.3.3. Epithelialization

The repetitive stereomicroscopic analysis of matrix epithelialization revealed a comparable epithelialization of HD (Figures 47A and D) and MD (Figures 47B and E) ad-MVF-seeded MWD, whereas the epithelialized surface of LD (Figures 47C and F) ad-MVF-seeded MWD was significantly reduced on day 10 and 14 (Figures 47C, F, and G). These findings were further confirmed by immunohistochemical staining of the epithelial layer on day 14 after implantation (Figures 48A-D). Accordingly, both HD (Figure 48A) and MD (Figure 48B) ad-MVF-seeded matrices exhibited a comparable cytokeratine⁺ epithelial layer, covering 75.0 ± 6.5 % and 66.0 ± 7.7 % of their surfaces, whereas LD (Figure 48C) ad-MVF-seeded matrices showed an epithelial coverage of only 57.0 ± 6.3 %.

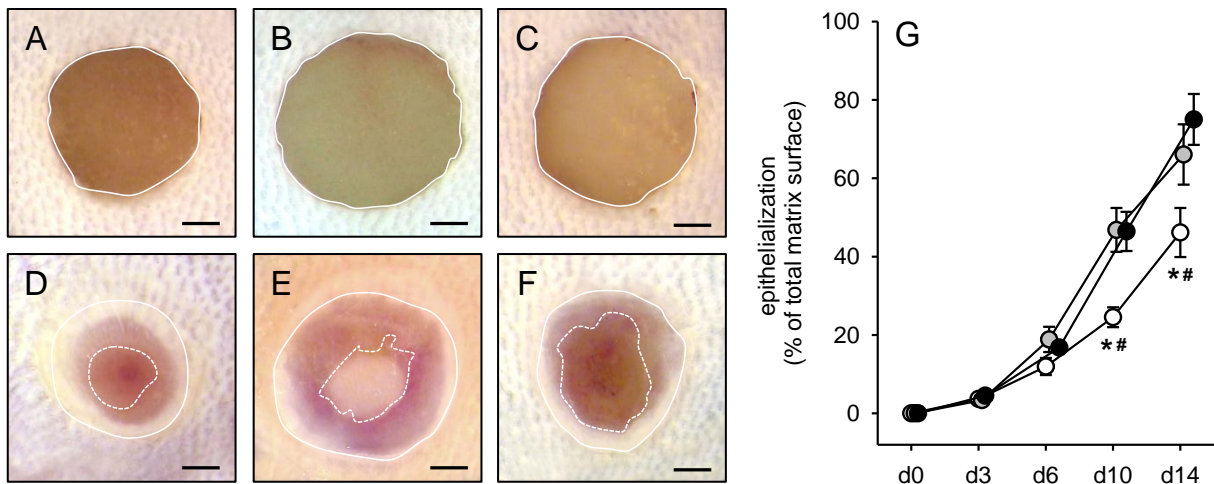


Figure 47. A-F: Stereomicroscopic images of implanted HD (A, D), MD (B, E), and LD (C, F) ad-MVF-seeded MWD directly (A-C) as well as on day 14 (D-F) after implantation into full-thickness skin defects within dorsal skinfold chambers of GFP⁺ C57BL/6 recipient mice. Scale bars = 750 μ m. **G:** Epithelialization (% of total matrix surface) of HD (black circles, n = 8), MD (grey circles, n = 8), and LD (white circles, n = 8) ad-MVF-seeded MWD, as assessed by planimetric analysis of stereomicroscopic images. Means \pm SEM. *p < 0.05 vs. HD ad-MVF-seeded MWD; #p < 0.05 vs. MD ad-MVF-seeded MWD.

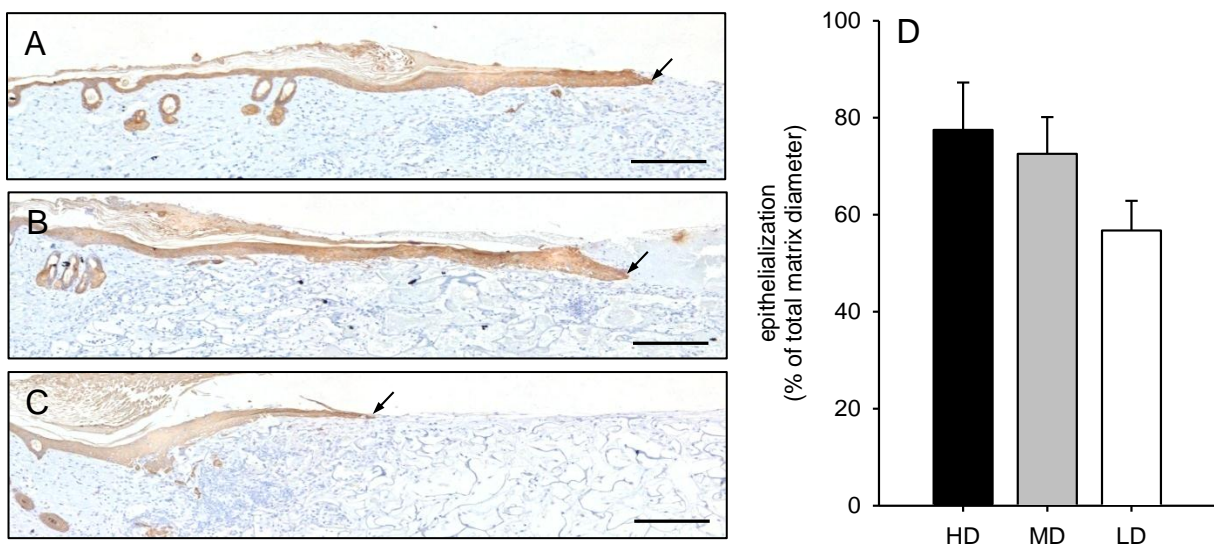


Figure 48. A-C: Immunohistochemical detection of the cytokeratine⁺ epithelial layer (arrows) covering HD (A), MD (B), and LD (C) ad-MVF-seeded MWD on day 14 after implantation into full-thickness skin defects within dorsal skinfold chambers of GFP⁺ C57BL/6 recipient mice. Scale bars = 0.8 mm. **D:** Epithelialization (% of total matrix diameter) of HD (black bar, n = 8), MD (grey bar, n = 8), and LD (white bar, n = 8) ad-MVF-seeded MWD, as assessed by immunohistochemical analysis. Means \pm SEM.

6.4. Ad-MVF vs. SVF single cells

6.4.1. Viability and cellular composition

In this experimental section it was analyzed whether the ad-MVF-based prevascularization of MWD is superior to the prevascularization with the SVF. After the isolation of SVF single cells (Figure 48A) and the ad-MVF cell-vessel suspension (Figure 48B), a viability test was performed to determine the cellular survival rate for both isolates prior to their seeding onto MWD. It could be demonstrated that $95.1 \pm 1.6 \%$ of all ad-MVF cells and only $81.8 \pm 0.6 \%$ ($p < 0.05$) of all SVF single cells were viable (Figures 48C and D). Flow cytometric analyses further revealed a comparable composition of both ad-MVF and SVF single cells (Table 4).

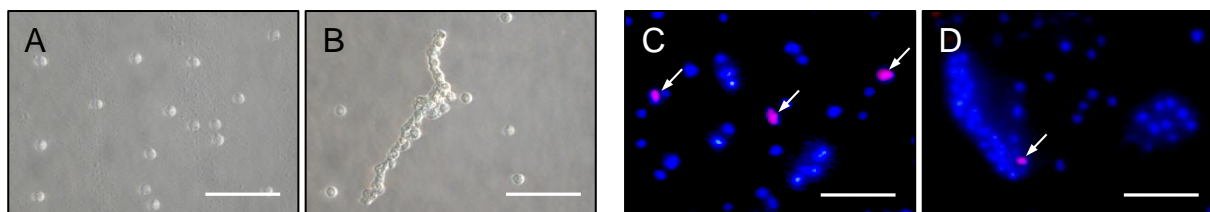


Figure 48. **A, B:** Light microscopy of SVF single cells (A) and ad-MVF (B). Scale bars = 50 μm . **C, D:** Bb/PI viability staining of SVF single cells (C) and ad-MVF (D). Blue cells = Bb staining of all nuclei. Red cells = PI staining of dead/damaged cells. Arrows = damaged cellular fraction of SVF single cells (C) and ad-MVF (D). Scale bars = 50 μm .

| | CD31 | α -SMA | ASAM | CD29 | CD90 | CD117 |
|---------------|----------------|----------------|----------------|----------------|----------------|----------------|
| SVF | 34.4 ± 7.3 | 17.3 ± 1.2 | 14.4 ± 3.2 | 47.6 ± 4.7 | 10.4 ± 3.3 | 12.7 ± 3.3 |
| Ad-MVF | 18.0 ± 3.2 | 16.4 ± 2.3 | 13.0 ± 1.6 | 47.5 ± 4.7 | 7.1 ± 2.3 | 9.2 ± 1.7 |

Table 4. Cellular expression (%) of CD31, α -SMA, ASAM, CD29, CD90, and CD117 within SVF and ad-MVF isolates from the epididymal fat pads of GFP⁺ C57BL/6 mice, as assessed by flow cytometric analysis. Mean \pm SEM.

6.4.2. Vascularization, hemorrhage formation, and incorporation

Unlike SVF single cells that form new blood vessels *de novo*, ad-MVF rapidly bridge wide distances throughout the seeded matrices by interconnecting to each other. Because of this, ad-MVF-seeded matrices showed blood-perfused ROIs within their center zones earlier than SVF single cell-seeded ones. Hence, center and border zones of the matrices were analyzed separately in the fourth experimental section. Repetitive intravital fluorescence microscopy of implanted MWD (Figures 49A-F) revealed that first blood-perfused microvessels could be observed on day 6 after implantation (Figures 49G and H). Throughout the following observation period, the density of microvessels increased in both groups. Of interest, ad-MVF-seeded matrices exhibited a higher fraction of perfused ROIs and a higher functional microvessel density within their border zones when compared to SVF-seeded MWD on day 14 (Figures 49G and I). This divergent degree of vascularization was even more pronounced within the center zones of the matrices (Figures 49H and J). Whereas ad-MVF-seeded MWD

was completely vascularized on day 14, SVF-seeded matrices only exhibited 25 % perfused ROIs. Furthermore, the functional microvessel density of SVF-seeded MWD was significantly diminished when compared to that of ad-MVF-seeded MWD on day 14 (Figure 49J).

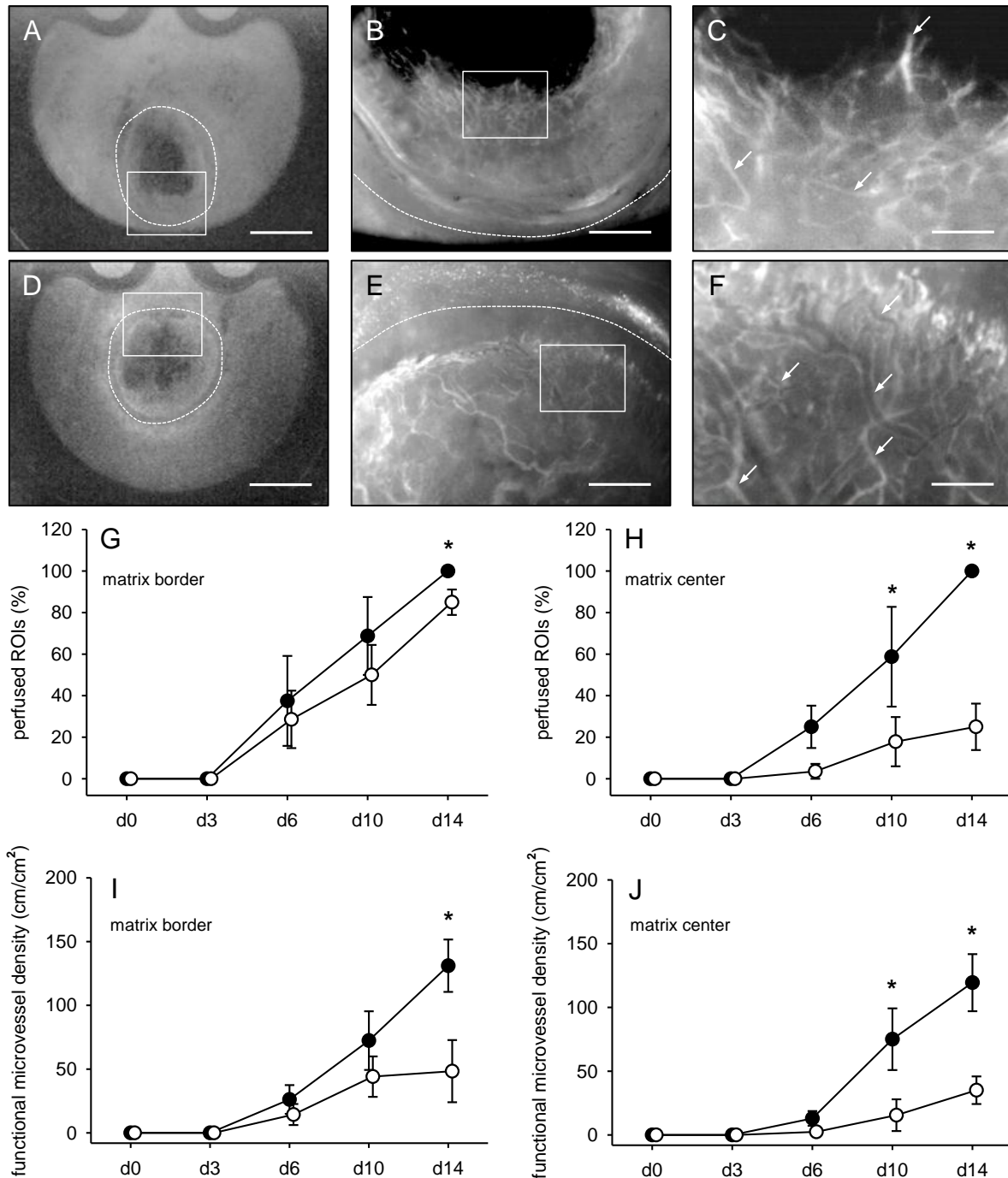


Figure 49. A-F: Intravital fluorescence microscopy (blue light epi-illumination with contrast enhancement by 5 % FITC-labeled dextran) of SVF- (A-C) and ad-MVF-seeded (D-F) MWD on day 14 after implantation into full-thickness skin defects within dorsal skinfold chambers of GFP⁻ C57BL/6 recipient mice. Dotted lines = matrix borders. Arrows = perfused blood vessels. B, E = higher magnifications of inserts in A and D. C, F = higher magnifications of inserts in B and E. Scale bars: A, D = 2.4 mm, B, E = 500 μ m; C, F = 125 μ m. **G-J:** Fraction of perfused ROIs (%) (G, H) and functional microvessel density (cm/cm²) (I, J) in the border (G, I) and center zones (H, J) of SVF- (white circles, n = 8) and ad-MVF-seeded (black circles, n = 8) MWD on day 0, 3, 6, 10, and 14 after implantation into full-thickness skin defects within GFP⁻ C57BL/6 recipient mice, as assessed by intravital fluorescence microscopy. Means \pm SEM. * $p < 0.05$ vs. SVF-seeded MWD.

The measurement of microhemodynamic parameters revealed that the diameter of individual microvessels within border and center zones of both groups decreased over time (Table 5). This was associated with an increase of the centerline RBC velocity and wall shear rate (Table 5). There were no significant differences of microhemodynamic parameters of individual microvessels between SVF- and ad-MVF-seeded matrices throughout the 14-day observation period. Trans-illumination stereomicroscopy was used to analyze whether SVF single cells or ad-MVF induce hemorrhage formation within the matrices (Figures 50A-F). It was shown that bleedings were elevated between day 6 and 10 of microvascular network formation. However, no significant differences in hemorrhage formation could be observed between SVF- and ad-MVF-seeded MWD (Figure 50G).

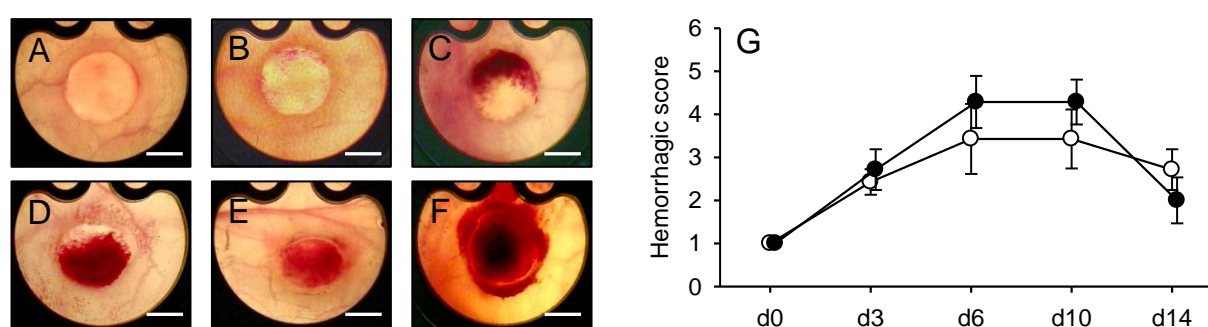


Figure 50. A-F: Trans-illumination stereomicroscopy of ad-MVF-seeded MWD within the dorsal skinfold chamber of GFP⁺ C57BL/6 recipient mice, displaying different manifestations of matrix-induced bleedings according to a semi-quantitative hemorrhagic score, i.e. 1: No bleeding (A), 2: 1-25 % (B), 3: 26-50 % (C), 4: 51-75 % (D), 5: 76-100 % (E), 6: Bleeding exceeding matrix surface (F). Scale bars = 1.3 mm. **G:** Hemorrhagic score of vehicle- (white circles; n = 8) and enox-treated (black circles; n = 8) ad-MVF-seeded MWD, as assessed by trans-illumination stereomicroscopy.

| | d0 | d3 | d6 | d10 | d14 |
|---|----|----|-------------------|-------------------|-------------------|
| <i>Diameter (μm)</i> | | | | | |
| Matrix border (SVF) | - | - | 32.0 \pm 2.6 | 18.3 \pm 1.6 | 17.6 \pm 1.4 |
| Matrix border (ad-MVF) | - | - | 27.4 \pm 3.6 | 19.2 \pm 0.8 | 17.6 \pm 1.9 |
| Matrix center (SVF) | - | - | 30.6 \pm 1.3 | 23.1 \pm 2.9 | 15.7 \pm 1.4 |
| Matrix center (ad-MVF) | - | - | 21.9 \pm 9.9 | 22.8 \pm 1.2 | 20.4 \pm 3.2 |
| <i>Centerline RBC velocity ($\mu\text{m/s}$)</i> | | | | | |
| Matrix border (SVF) | - | - | 299.8 \pm 102.8 | 307.8 \pm 71.7 | 657.7 \pm 158.2 |
| Matrix border (ad-MVF) | - | - | 117.6 \pm 47.3 | 284.7 \pm 102.7 | 311.9 \pm 51.8 |
| Matrix center (SVF) | - | - | 133.1 \pm 84.1 | 388.2 \pm 67.7 | 483.7 \pm 82.0 |
| Matrix center (ad-MVF) | - | - | 182.3 \pm 121.3 | 332.9 \pm 113.5 | 309.8 \pm 26.2 |
| <i>Wall shear rate (s^{-1})</i> | | | | | |
| Matrix border (SVF) | - | - | 75.2 \pm 23.3 | 125.1 \pm 20.3 | 291.8 \pm 45.8 |
| Matrix border (ad-MVF) | - | - | 33.1 \pm 11.9 | 116.8 \pm 31.6 | 150.7 \pm 31.9 |
| Matrix center (SVF) | - | - | 35.9 \pm 23.6 | 145.9 \pm 33.2 | 245.7 \pm 55.5 |
| Matrix center (ad-MVF) | - | - | 58.5 \pm 17.8 | 121.3 \pm 44.6 | 130.5 \pm 28.9 |

Table 5. Diameter, centerline RBC velocity, and wall shear rate of individual microvessels within the border and center zones of SVF- and ad-MVF-seeded MWD on day 0 (day of implantation) as well as 3, 6, 10, and 14 days after implantation into full-thickness skin defects within dorsal skinfold chambers of GFP⁺ C57BL/6 recipient mice. Mean \pm SEM.

At the end of the 2-week observation period, the matrices were histologically and immunohistochemically analyzed. HE-stained sections revealed a comparable infiltration of a dense vascularized granulation tissue within the border zones of SVF- (3697 ± 373 cells/mm²) and ad-MVF-seeded (4515 ± 347 cells/mm²) NWD (Figures 51A and C). Interestingly, ad-MVF-seeded matrices exhibited a significantly higher number of infiltrated single cells within their center zones (3465 ± 433 cells/mm²) when compared to SVF-seeded matrices (1884 ± 485 cells/mm²) (Figures 51B and D).

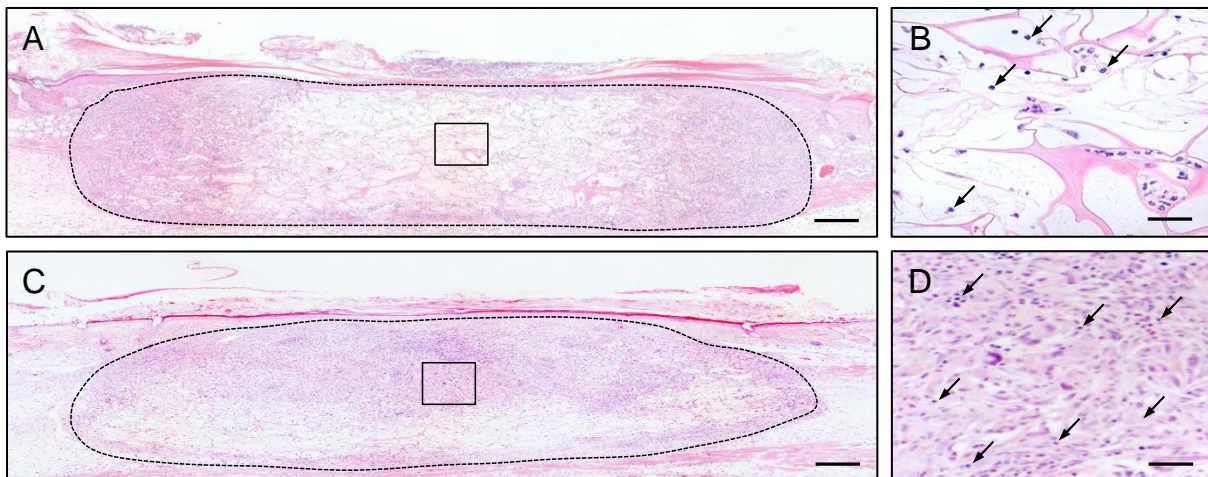


Figure 51. A-D: HE-stained sections of SVF- (A, B) and ad-MVF-seeded (C, D) MWD on day 14 after implantation into full-thickness skin defects within dorsal skinfold chambers of GFP⁺ C57BL/6 recipient mice. Broken lines = matrix. Frames = center zones of the matrices. B, D = higher magnifications of closed frames in A and C. Scale bars: A, C = 260 μ m; B, D = 40 μ m.

Although not proven to be significant, detection of Sirius red-stained sections revealed that SVF-seeded MWD contained less mature collagen fibers within its center zones when compared to ad-MVF-seeded MWD, indicating an improved incorporation of ad-MVF-seeded matrices on day 14 (Figures 52A-D). Immunohistochemical analyses showed a significantly higher density of CD31⁺ microvessels in both border and center zones of ad-MVF-seeded MWD when compared to SVF-seeded MWD (Figures 53A-E).

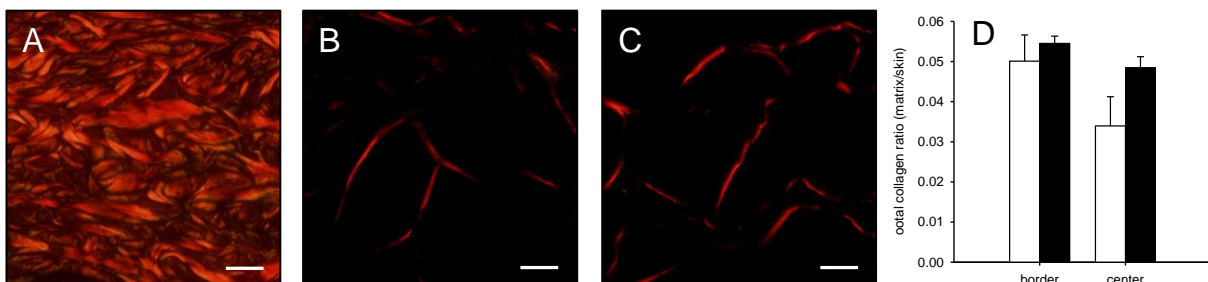


Figure 52. A-C: Polarized light microscopy of Sirius red-stained sections of normal skin (A) as well as SVF- (B) and ad-MVF-seeded (C) matrices. Scale bars = 25 μ m. **D:** Total collagen ratio (matrix/skin) in the border and center zones of SVF- (white bars, n = 8) and ad-MVF-seeded (black bars, n = 8) matrices on day 14, as assessed by histology. Means \pm SEM.

Of interest, CD31/GFP co-stainings revealed that ~ 90 % of all detected microvessels in the center zones of all matrices originated from the seeded GFP⁺ isolates. Whereas the border zones of ad-MVF-seeded matrices also contained > 90 % GFP⁺ microvessels, only ~ 67 % of all microvessels within the border zones of SVF-seeded matrices were GFP⁺ (Figures 53F-I).

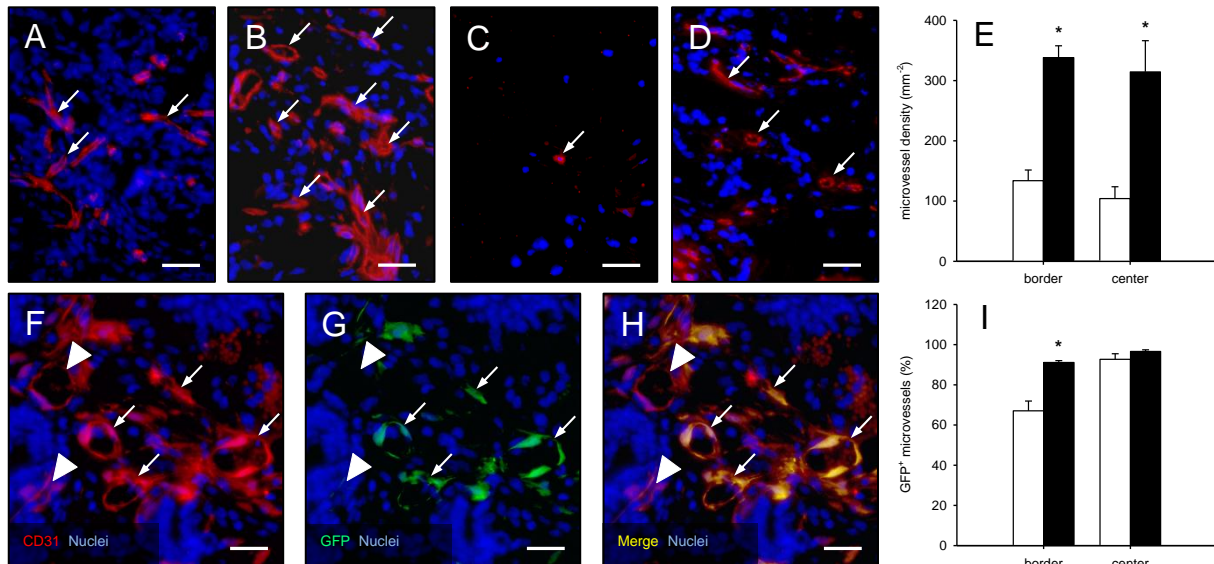


Figure 53. A-D: Immunohistochemical detection of CD31⁺ microvessels (arrows) within the border (A, C) and center (B, D) zones of SVF- (C, D) and ad-MVF-seeded (A, B) matrices. Scale bars = 25 μm. E: Microvessel density (mm⁻²) in the border and center zones of SVF- (white bars, n = 8) and ad-MVF-seeded (black bars, n = 8) MWD on day 14, as assessed by immunohistochemistry. Means ± SEM. *p < 0.05 vs. SVF-seeded MWD. F-H: CD31⁺/GFP⁺ microvessels (% , arrows) in ad-MVF-seeded MWD. Arrowheads = CD31⁺/GFP⁻ microvessels. Scale bars = 45 μm. I: GFP⁺ microvessels (%) within the border and center zones of SVF- (white bars, n = 8) and ad-MVF-seeded (black bars, n = 8) MWD. Means ± SEM. *p < 0.05 vs. SVF-seeded MWD.

6.4.3. Epithelialization

Repetitive stereomicroscopic analyses of the matrices revealed a comparable epithelialization of SVF- and ad-MVF-seeded MWD (Figures 54A-G). On day 14 after implantation, these findings were further confirmed by the detection of a cytokeratine⁺ epithelial layer covering ~ 80 % of both matrices' surfaces (Figures 55A-C).

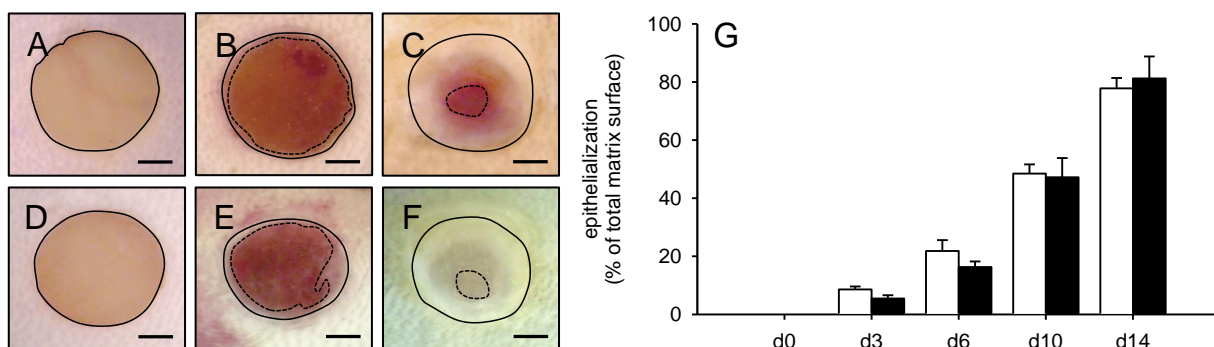


Figure 54. A-F: Stereomicroscopic images showing the epithelialization of implanted SVF- (A-C) and ad-MVF-seeded (D-F) MWD directly (A, D) as well as on day 6 (B, E) and 14 (C, F) after implantation into full-thickness skin defects within dorsal skinfold chambers of GFP⁻ C57BL/6 recipient mice. Scale bars = 1 mm. G: Epithelialization (% of total matrix diameter) of SVF- (white bars, n = 8) and ad-MVF-seeded (black bars, n = 8) MWD on day 0, 3, 6, 10, and 14 after implantation. Means ± SEM.

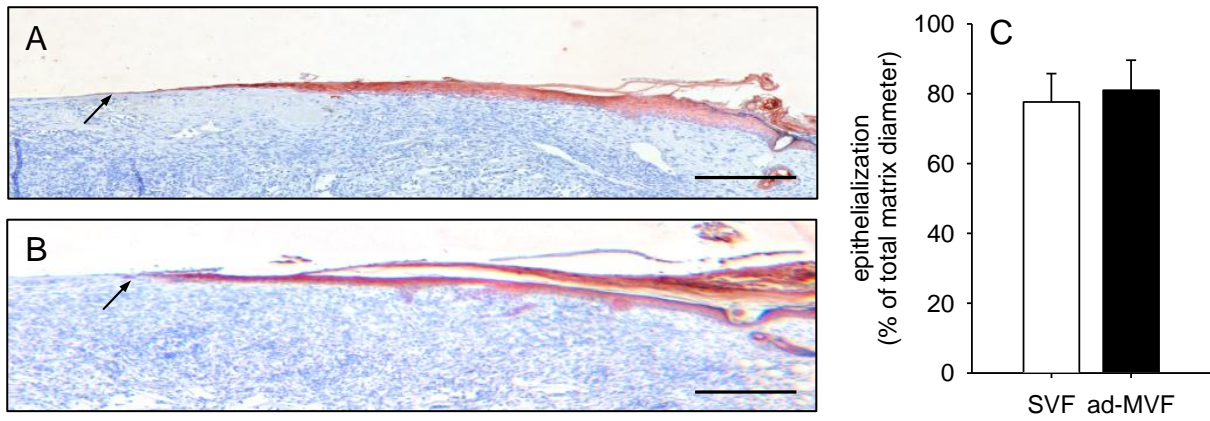


Figure 55. A, B: Immunohistochemical detection of the cyokeratine⁺ epithelial layer (arrows) covering SVF- (A) and ad-MVF-seeded (B) MWD on day 14 after implantation into full-thickness skin defects within dorsal skinfold chambers of GFP⁻ C57BL/6 recipient mice. Scale bars = 300 μ m. **C:** Epithelialization (% of total matrix surface) of SVF- (white bars, n = 8) and ad-MVF-seeded (black bars, n = 8) MWD on day 14 after implantation, as assessed by immunohistochemistry. Means \pm SEM.

6.5. Enox treatment

6.5.1. Vascularization and tail vein bleeding time

It is known that LMWHs, such as enox, not only exhibit anti-thrombotic but also anti-angiogenic properties. This may prevent the interconnection of seeded ad-MVF and/or increase the risk of matrix-induced bleeding after implantation of MWD. Accordingly, in this experimental section the vascularization of enox- and vehicle-treated ad-MVF-seeded MWD was analyzed by means of intravital fluorescence microscopy (Figures 56A-L). On day 3 after implantation of enox-treated, ad-MVF-seeded matrices, individual blood-perfused microvessels could already be detected, indicating an early interconnection of ad-MVF with the surrounding host microvasculature (Figure 56M). In contrast, vehicle-treated, ad-MVF-seeded MWD did not exhibit blood-perfused microvessels before day 6 after implantation (Figure 56M). Throughout the remaining observation days, seeded ad-MVF reassembled into newly developing microvascular networks within both matrices (Figures 56M and N). Noteworthy, enox-treated matrices exhibited a slightly increased density of these networks, as indicated by a significantly higher functional microvessel density on day 10 when compared to vehicle-treated controls (Figure 56N). Furthermore, a continuous vascular maturation was observed in both groups over time, as characterized by progressively decreasing diameters as well as increasing centerline RBC velocities and wall shear rates of individual microvessels (Table 6).

| | d0 | d3 | d6 | d10 | d14 |
|---|----|-----------------|------------------|-------------------|-------------------|
| <i>Diameter (μm)</i> | | | | | |
| Vehicle | - | - | 30.6 \pm 6.1 | 22.5 \pm 2.1 | 17.8 \pm 1.6 |
| Enox | - | 38.6 \pm 5.5 | 29.0 \pm 1.9 | 19.8 \pm 1.2 | 16.3 \pm 1.0 |
| <i>Centerline RBC velocity ($\mu\text{m/s}$)</i> | | | | | |
| Vehicle | - | - | 174.7 \pm 74.4 | 440.9 \pm 103.7 | 562.9 \pm 111.2 |
| Enox | - | 22.5 \pm 14.5 | 299.6 \pm 83.7 | 463.9 \pm 14.2 | 445.9 \pm 52.3 |
| <i>Wall shear rate (s^{-1})</i> | | | | | |
| Vehicle | - | - | 45.8 \pm 23.5 | 156.1 \pm 29.1 | 273.9 \pm 67.4 |
| Enox | - | 5.5 \pm 3.9 | 82.3 \pm 23.6 | 190.2 \pm 10.7 | 225.1 \pm 30.8 |

Table 6. Diameter (μm), centerline RBC velocity ($\mu\text{m/s}$), and wall shear rate (s^{-1}) of individual microvessels within enox- and vehicle-treated (control) ad-MVF-seeded MWD on day 0 (day of implantation) as well as 3, 6, 10 and 14 days after implantation into dorsal skinfold chambers of GFP⁻ C57BL/6 recipient mice. Mean \pm SEM.

To verify the anti-coagulative activity of enox, a tail vein bleeding test was performed at the end of the 2-week observation period. As anticipated, the tail vein bleeding time in enox-treated mice was significantly prolonged when compared to vehicle-treated controls (Figure 56O).

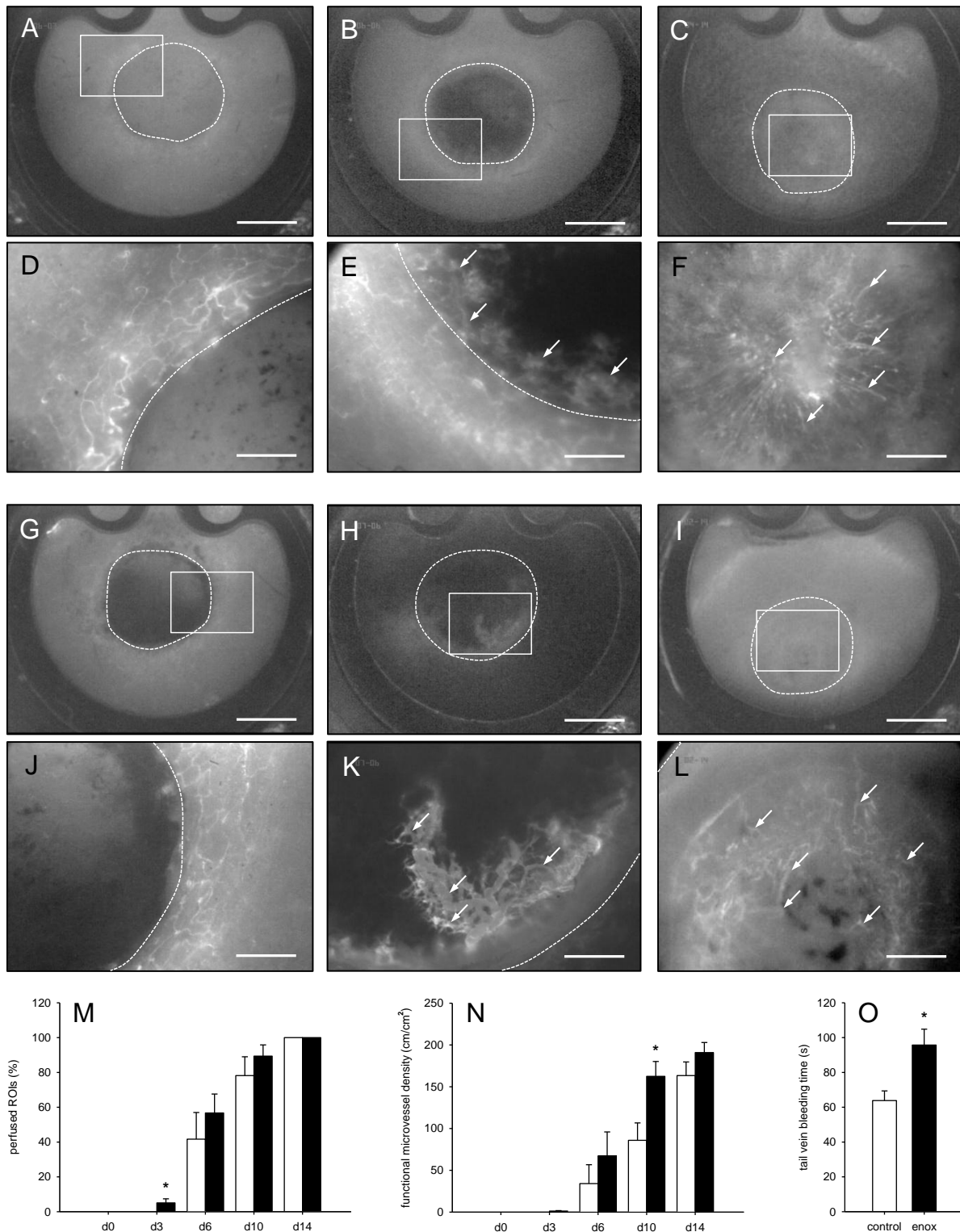


Figure 56. A-L: Intravital fluorescence microscopy (blue light epi-illumination, 5 % FITC-labeled dextran) of vehicle- (A-F) and enox-treated (G-L) ad-MVF-seeded MWD on day 0 (A, D, G, J), 6 (B, E, H, K), and 14 (C, F, I, L) after implantation into full-thickness skin defects within dorsal skinfold chambers of GFP⁻ recipient mice. A-C and G-I = overview of the chamber observation window. D-F and J-L = higher magnifications of inserts in A-C and G-I. Broken line = matrix border. Arrows = perfused microvessels. Scale bars: A-C and G-I = 2.2 mm, D-F and J-L = 500 μ m. **M, N:** Perfused ROIs (%) (M) and functional microvessel density (cm/cm²) (N) of vehicle- (white bars; n = 8) and enox-treated (black bars; n = 8) ad-MVF-seeded MWD. Means \pm SEM. * $p < 0.05$ vs. vehicle. **O:** Tail vein bleeding time (s) of vehicle- (white bar; n = 8) and enox-treated (black bar; n = 8) mice, as assessed by the tail vein bleeding test. Means \pm SEM. * $p < 0.05$ vs. control.

6.5.2. Hemorrhage formation

Trans-illumination stereomicroscopy was used to analyze whether the anti-coagulative effect of enox promotes hemorrhage formation within ad-MVF-seeded matrices (Figures 57A-G). The highest hemorrhagic score in both groups could be detected on day 6 (Figures 57B, E, and G).

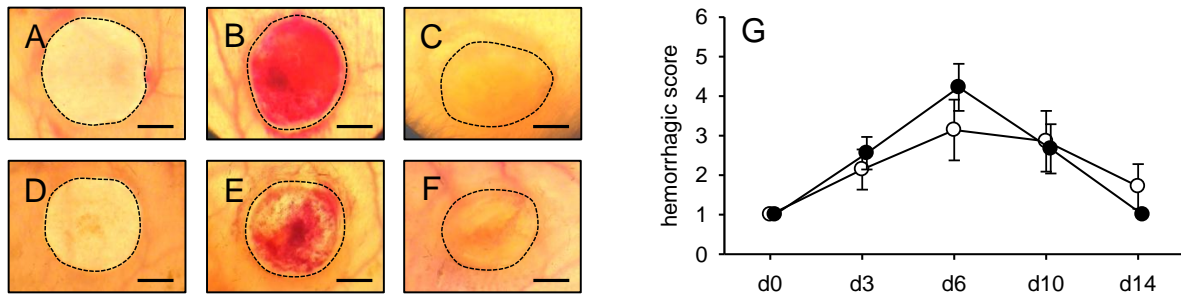


Figure 57. A-F: Trans-illumination stereomicroscopy of vehicle- (A-C) and enox-treated (D-F) ad-MVF-seeded MWD on day 0 (A, D), 6 (B, E), and 14 (C, F) after implantation into full-thickness skin defects within dorsal skinfold chambers of GFP⁺ recipient mice, as assessed by the semi-quantitative hemorrhagic score, i.e. 1: No bleeding, 2: 1-25 %, 3: 26-50 %, 4: 51-75 %, 5: 76-100 %, 6: Bleeding exceeding matrix surface. Scale bars = 1.5 mm. G: Hemorrhagic score of vehicle- (white circles; n = 8) and enox-treated (black circles; n = 8) ad-MVF-seeded MWD, as assessed by trans-illumination stereomicroscopy.

6.5.3. Incorporation

In line with the aforementioned *in vivo* results, further histological analyses revealed a comparable incorporation of vehicle- and enox-treated MWD within dorsal skinfold chambers of GFP⁺ C57BL/6 recipient mice on day 14 after implantation. Matrices of both groups were surrounded by a well-vascularized granulation tissue, which also grew into the pores of the matrices' border zones (Figures 58A-D).

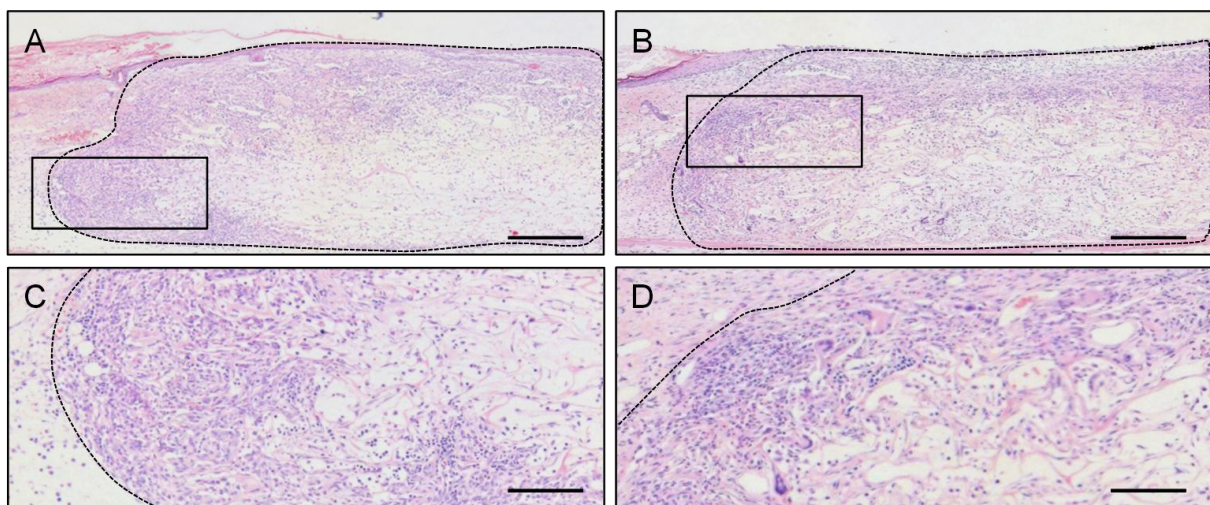


Figure 58. A-D: HE-stained sections of vehicle-treated (A, C) and enox-treated (B, D) ad-MVF-seeded MWD on day 14 after implantation into full-thickness skin defects within dorsal skinfold chambers of GFP⁺ C57BL/6 recipient mice. Broken line = matrix border. C and D = higher magnifications of inserts in A and B. Scale bars: A, B = 200 μ m; C, D = 60 μ m.

Furthermore, both matrices exhibited a comparable number of CD31⁺ microvessels (~ 140 mm⁻²) (Figure 59A-C) as well as a comparable collagen content on day 14 after implantation (Figures 59D-G). Additionally, CD31/GFP co-staining revealed that ~ 90 % of the microvessels within the matrices were GFP⁺ and, hence, originated from the seeded ad-MVF (Figures 59H-K).

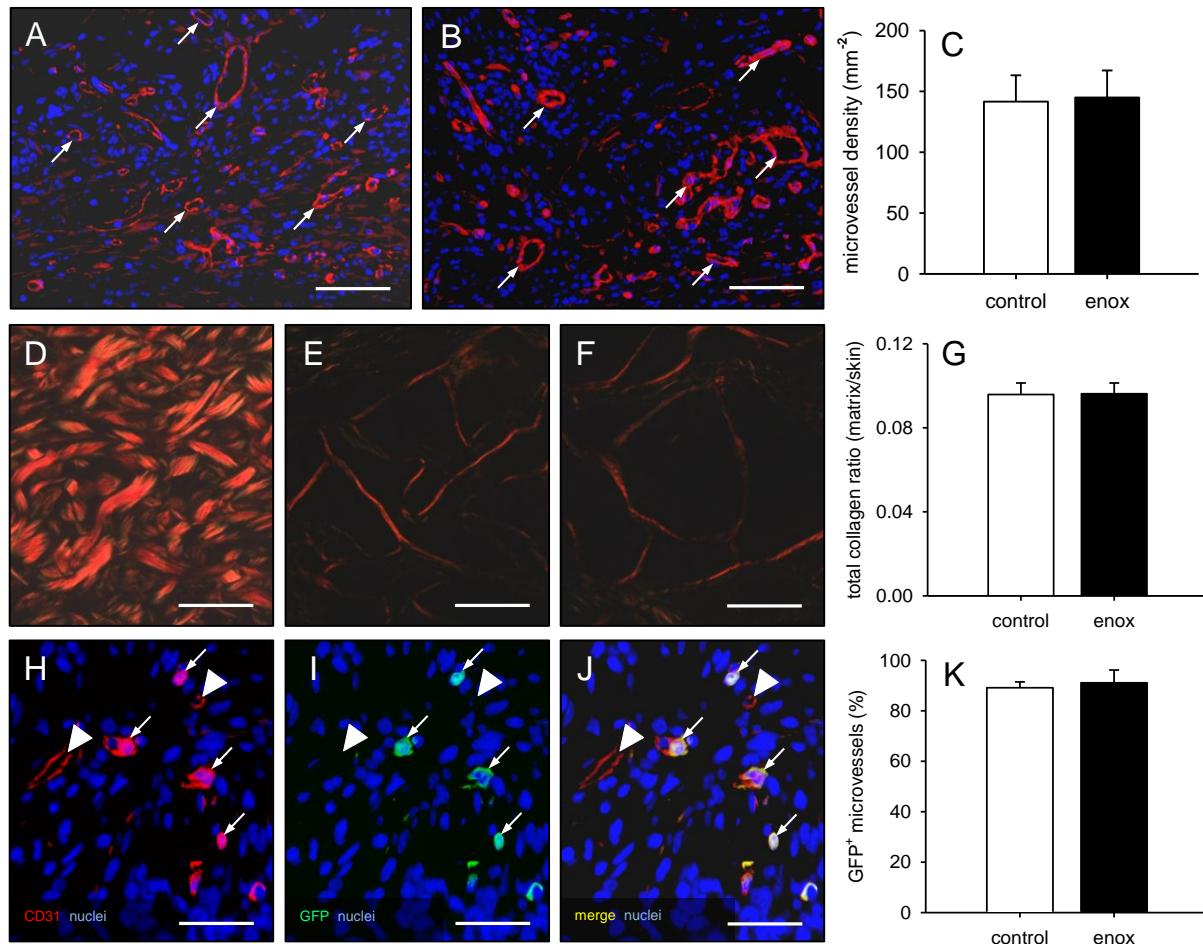


Figure 59. **A, B:** Immunohistochemical detection of CD31⁺ microvessels (arrows) within vehicle- (A) and enox-treated (B) MWD on day 14 after implantation into full-thickness skin defects within dorsal skinfold chambers of GFP C57BL/6 recipient mice. Scale bars = 65 μ m. **C:** Microvessel density (mm⁻²) within vehicle- (white bar; n = 8) and enox-treated (black bar; n = 8) ad-MVF-seeded MWD, as assessed by immunohistochemical analysis. Means \pm SEM. **D-F:** Polarized light microscopy of Sirius red-stained sections of normal skin (D) as well as vehicle- (E) and enox-treated (F) ad-MVF-seeded MWD. Scale bars = 32 μ m. **G:** Total collagen ratio (matrix/skin) within vehicle- (white bar; n = 8) and enox-treated (black bar; n = 8) ad-MVF-seeded MWD. Means \pm SEM. **H-J:** CD31⁺/GFP⁺ microvessels (arrows) in ad-MVF-seeded MWD. Arrowheads = CD31⁺/GFP⁻ microvessels. Scale bars = 45 μ m. **K:** GFP⁺ microvessels (%) within vehicle- (white bars, n = 8) and enox-treated (black bars, n = 8), ad-MVF-seeded MWD. Means \pm SEM.

6.5.4. Epithelialization

Repetitive epi-illumination stereomicroscopy of vehicle- and enox-treated MWD revealed a progressing and comparable epithelialization of both vehicle- and enox-treated matrices over time (Figures 60A-G). These results were further confirmed by immunohistochemical analyses. These analyses showed that ~ 87 % of the matrices' surfaces were covered by a

cytokeratine⁺ epithelial layer on day 14 after implantation (Figures 61A-C).

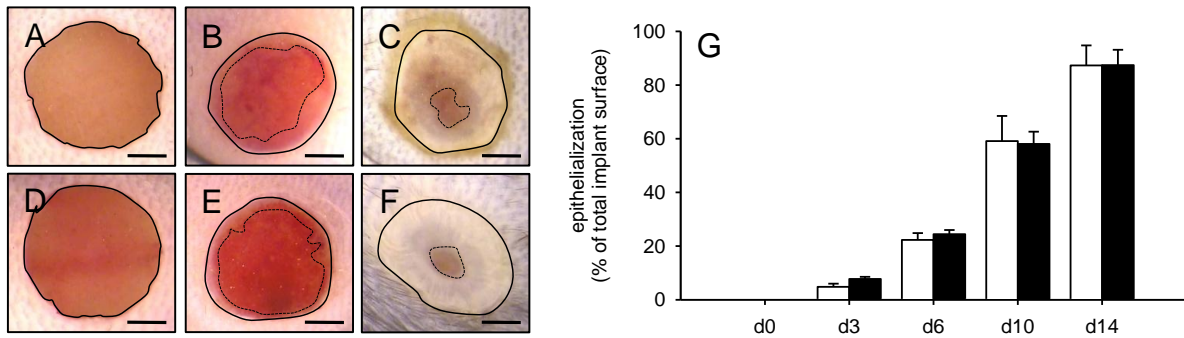


Figure 60. A-F: Stereomicroscopic images of implanted vehicle- (A-C) and enox-treated (D-F) ad-MVF-seeded MWD on day 0 (A, D) as well as on day 6 (B, E) and 14 (C, F) after implantation into full-thickness skin defects within dorsal skinfold chambers of GFP⁻ C57BL/6 recipient mice. Scale bars = 750 μm. **G:** Epithelialization (% of total matrix surface) of vehicle- (white bars; n = 8) and enox-treated (black bars; n = 8) ad-MVF-seeded MWD, as assessed by planimetric analysis of stereomicroscopic images. Means ± SEM.

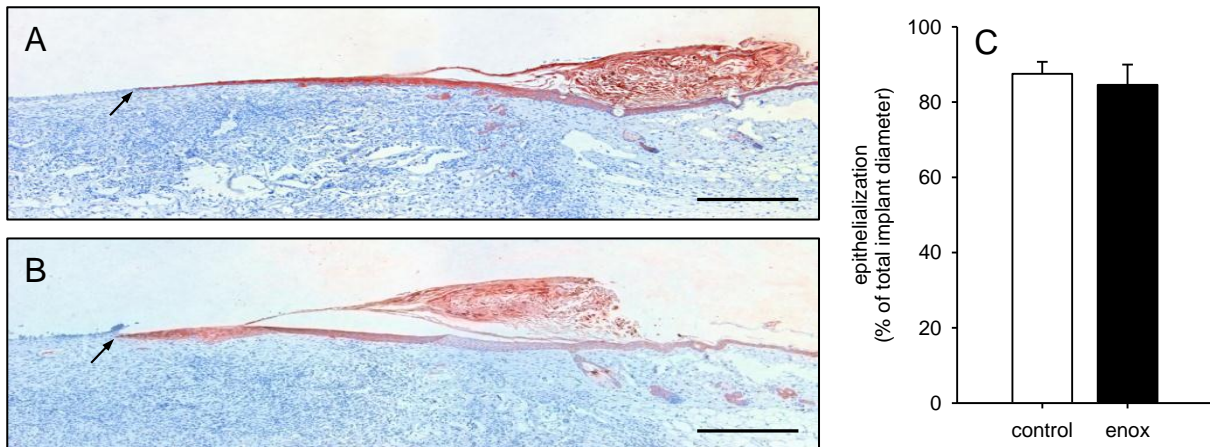


Figure 61. A, B: Immunohistochemical detection of the cytokeratine⁺ epithelial layer (arrows) covering vehicle- (A) and enox-treated (B) ad-MVF-seeded MWD on day 14 after implantation into full-thickness skin defects within dorsal skinfold chambers of GFP⁻ C57BL/6 recipient mice. Scale bars = 330 μm. **C:** Epithelialization (% of total matrix diameter) of vehicle- (white bars; n = 8) and enox-treated (black bars; n = 8) ad-MVF-seeded MWD, as assessed by immunohistochemical analysis. Means ± SEM.

6.6. Summary of the results

The aim of the present doctoral thesis was to test several hypotheses, which may be of crucial importance for the transfer of ad-MVF as prevascularization units into clinical practice.

In a **first set of experiments** it was tested whether older GFP⁺ C57BL/6 donor animals contain reduced volumes of adipose tissue as well as lower numbers of ad-MVF when compared to younger ones. The following results were found:

- Older donor mice did not contain reduced volume of adipose tissue when compared to younger ones.
- Older donor mice did not contain reduced numbers of ad-MVF when compared to younger ones.
- Ad-MVF isolated from 7 - 12 months old donor mice exhibit both a comparable cellular composition and length distribution.

In a **second set of experiments** it was first tested whether the difference in MWD and FWM sample preparation leads to variations in their fiber thicknesses, fiber lengths, or pore sizes. Moreover, it was tested whether a more homogeneous seeding of ad-MVF into FWM is possible and leads to an improved matrix vascularization and incorporation when compared to ad-MVF-seeded MWD. The following results were found:

- The preparation of FWM does not lead to different pore sizes, fiber thicknesses, or fiber lengths when compared to MWD.
- FWM allows a more homogeneous distribution of ad-MVF during sample preparation when compared to MWD.
- The more homogeneous distribution of ad-MVF within FWM leads to a reduced vascularization and incorporation when compared to ad-MVF-seeded MWD.

In a **third set of experiments** it was tested whether the seeding density of ad-MVF is a crucial determinant for the adequate vascularization and incorporation of matrices. The following results were found:

- The least required density of ad-MVF to guarantee an adequate matrix vascularization and incorporation is 80,000 ad-MVF/cm².

- MWD seeded with less than 80,000 ad-MVF/cm² exhibits a reduced oxygenation on day 14 after implantation into full-thickness skin defects within dorsal skinfold chambers of GFP⁻ C57BL/6 recipient mice.

In a **fourth set of experiments** it was tested whether the novel approach of ad-MVF-based prevascularization is superior to the prevascularization with the SVF. The following results were found:

- Freshly isolated ad-MVF exhibit a significantly higher viability when compared to SVF single cells.
- Ad-MVF-seeded MWD exhibits a better vascularization and incorporation when compared to SVF-seeded MWD.

In a **fifth set of experiments** it was tested whether the anti-angiogenic and anti-coagulative properties of enox lead to a reduced interconnection of ad-MVF and/or increased matrix-induced bleeding. The following results were found:

- The anti-angiogenic properties of enox do not lead to a reduced vascularization within ad-MVF-seeded MWD.
- The anti-coagulative properties of enox do not promote increased hemorrhage formation within ad-MVF-seeded MWD.

7. Discussion

7.1. Discussion of materials and methods

7.1.1. Dorsal skinfold chamber model

In 1928, the first observation chamber was implanted into the ears of rabbits to study the behavior of living cells by means of intravital microscopy [SANDISON, 1928]. The transparent chamber model was then adapted for its use in mice in 1943 [ALGIRE et al., 1943]. This particularly allowed analyses of both growth and vascularization of implanted tumors [ALGIRE et al., 1943]. However, newly formed granulation tissue impaired the analysis of the physiological microvasculature [ALGIRE et al., 1943]. After the chamber model was continuously modified, it has been widely used for the analysis of the microcirculation over the past decades [LEHR et al., 1993; USHIYAMA et al., 2004; CONTALDO et al., 2007; DEBERGH et al., 2010; LASCHKE et al., 2011; SCKELL and LEUNIG, 2016]. The dorsal skinfold chamber model bears the advantage that the chamber window can be horizontally placed under a microscope for repetitive and non-invasive intravital microscopy in trans-illumination or epi-illumination [LASCHKE and MENDER, 2016]. In addition, since the cover glass of the chamber can temporarily be removed, the dorsal skinfold chamber model is a perfect tool for the chronic observation of implanted biomaterials and tissue constructs. However, to assure an air-free closure of the chamber, the size of the matrices should not exceed $\sim 3 \times 3 \times 1$ mm [LASCHKE and MENDER, 2016]. This size is not comparable to the size of biomaterials usually implanted into patients in clinical practice. Nonetheless, the experimental setting of the dorsal skinfold chamber model allows for the *in vivo* observation of matrix vascularization under highly standardized conditions.

Despite all benefits of the dorsal skinfold chamber model, complications may appear throughout the observation period of 2 weeks. Although the titanium chamber is designed with a relatively low weight of ~ 4 g, it may progressively subside laterally over time. Hence, in the present work, some of the created full-thickness skin defects changed their location within the observation window over time, eventually moving from their well-observable central position (Figure 62A) to an only partly observable position underneath the snap ring (Figure 62B). In such a case, the snap ring was removed before the microscopic imaging. Accordingly, microscopic epi- and transillumination microscopy of all implanted matrices could be conducted throughout the 14-day observation period.

Besides the dislocation of implanted matrices, the formation of hemorrhages could be observed throughout the experiments. Noteworthy, appearance and severity of the bleeding

correlated with the formation of microvascular networks within the implanted matrices. Particularly during the early stage of the vascularization process, when individual ad-MVF interconnected with each other or the blood vessels of the surrounding host tissue, matrix-induced bleeding complicated the detection of newly epithelialized areas during epi-illumination microscopy (Figure 62C). This was due to the rather incomplete and immature microvascular networks, leading to a leakage of blood particularly around day 6 after implantation of the matrices into the full-thickness skin defects. Since, for these reasons, epi-illumination was not always sufficient to detect the epithelial layer, trans-illumination had to be additionally used. Noteworthy, the combination of epi- and trans-illumination microscopy allowed the detection of epithelial layers at every time point of the 2-week observation period, regardless of the bleeding severity.

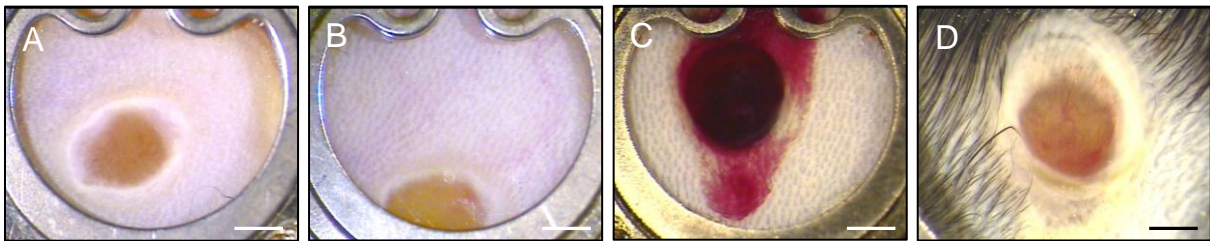


Figure 62. **A:** Full-thickness skin defect filled with MWD in the center of the observation window on day 14 after implantation, allowing an unproblematic detection of epithelialization. **B:** Dislocated wound on day 14, partially covered by the snap ring. **C:** Severe bleeding of the wound on day 6 after implantation. **D:** Ingrowth of hair into the dorsal skinfold chamber on day 14 after implantation. Scale bars: A-C = 1.9 mm; D = 1.3 mm.

For all *in vivo* experiments, dorsal skinfold chambers were implanted into C57BL/6 mice, one of the most used mouse strains for experimental studies [MARIN-BAÑASCO et al., 2014]. However, this strain is also known to exhibit skin pigmentations due to the accumulation of melanin [VAN DER HEIJDEN et al., 1995; PLONKA et al., 2005]. The appearance of “black spots” [WEISSMAN, 1967] within the animals’ skin is unpredictable and can only be detected after depilation. Since hair and melanin lead to a thicker skin, the fluorescent signal within the microvascular network may not, or only partly, be detected. Hence, this may impair the imaging quality of intravital fluorescence microscopy. Accordingly, animals that entered the *in vivo* experiments of the present thesis had to be carefully selected. Only mice without pigmented skin (Figures 63A and B) were used for the implantation of dorsal skinfold chambers. However, mice showing only little amounts of pigmented skin could still be used when the estimated position of the observation window was guaranteed within a non-pigmented area (Figures 63C and D). This selection of mice guaranteed a consistently sufficient intravital fluorescence microscopic imaging quality and prevented a loss of data throughout the entire observation period. Of interest, skin abnormalities were not always obvious. Although skin appeared to be “normal” after depilation, an increased growth rate of hair could sometimes be observed (Figure 62D). This, however, did not hinder a straight-

forward workflow or cause a loss of data. In fact, the detection of newly epithelialized areas by means of epi-illumination as well as the detection of hemorrhages by means of trans-illumination could still be performed with no limitations.

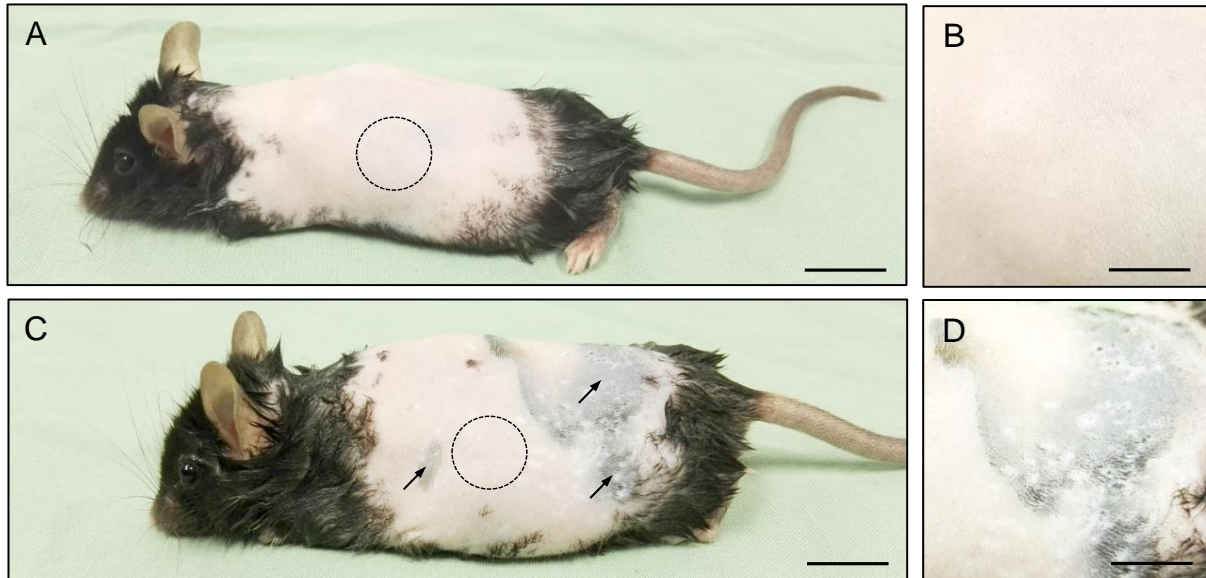


Figure 63. **A:** C57BL/6 mouse exhibiting normal skin without pigmentation. Circle = estimated position of the observation window after dorsal skinfold chamber implantation. Scale bar = 12 mm. **B:** Higher magnification of the skin, showing no pigmentation. Scale bar = 6 mm. **C:** C57BL/6 mouse exhibiting pigmented skin. Circle = estimated position of the observation window after dorsal skinfold chamber implantation. Arrows = pigmented areas of the skin. Scale bar = 10 mm. **D:** Higher magnification of the skin, showing a strong pigmentation. Scale bar = 6 mm.

7.1.2. Intravital fluorescence microscopy

Intravital fluorescence microscopy is a widely used method to study the microcirculation and to assess microhemodynamic parameters by visualizing the blood flow (Figure 64) via the injection of fluorescent dyes [VAJKOCZY et al., 1998; STEINBAUER et al., 2000; BARON et al., 2011; BOULAFALI et al., 2012]. Moreover, this method allows a repetitive detection and, hence, represents an ideal approach to observe dynamic processes, such as angiogenesis. In combination with image processing techniques, this approach allows the recording of microscopic images and videos, which can easily be evaluated at the end of the experiments without any additional stress for the animals. However, a too long exposure time to light excitation can still lead to damage of the visualized tissue, caused by the induction of oxygen radicals [KONTOS et al., 1983]. Consequences of such phototoxic effects on the microcirculation can be an increased activation of platelets with thrombus formation [HERRMANN, 1983], damage of endothelial cells leading to an increased permeability of the vessel wall [KONTOS et al., 1983], vasospasms [SAETZLER et al., 1997], increased leukocyte-endothelial cell interactions [SAETZLER et al., 1997], or the reduction of the functional microvessel density [FRIESENECKER et al., 1994]. Of interest, as shown in previous studies in

hamster dorsal skinfold chambers [STEINBAUER et al., 2000], such effects can be avoided by keeping the exposure time of the analyzed tissue to light excitation to a minimum of ~ 15 - 20 minutes. In the present work, this time limit was not exceeded.

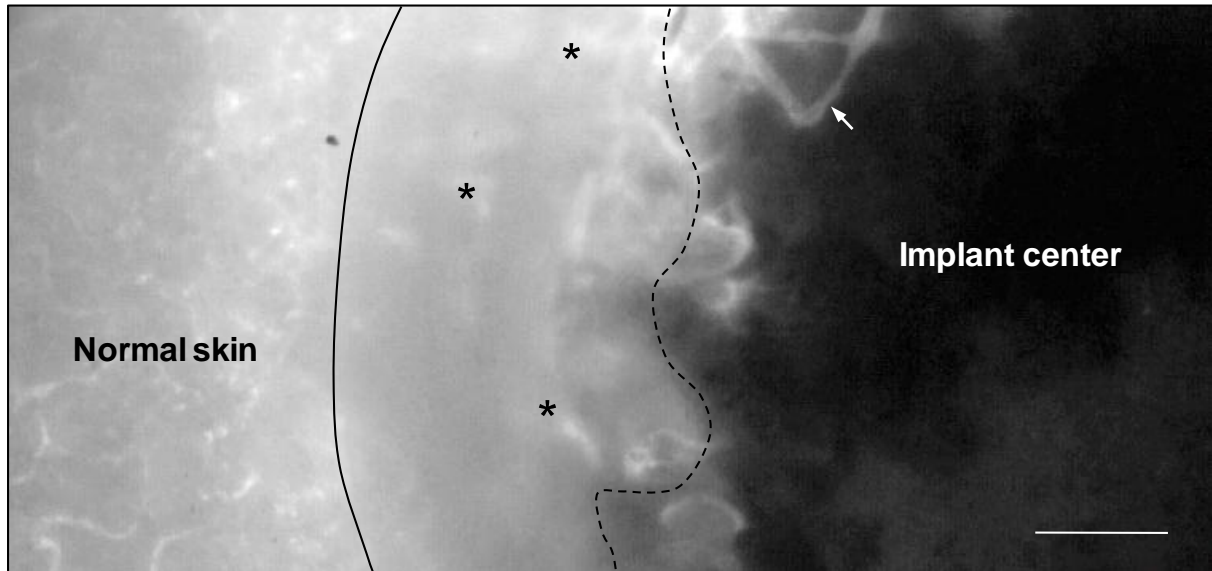


Figure 64. Intravital fluorescence microscopic image of ad-MVF-seeded MWD on day 10 after implantation into a full-thickness skin defect within a dorsal skinfold chamber of a GFP⁺ C57BL/6 recipient mouse. Black line = matrix border. Asterisks = newly developing epithelial layer. Broken line = edge of the epithelial layer. Arrow = newly developed blood-perfused vessel. Scale bar = 250 μ m.

7.2. Discussion of the results

7.2.1. Ad-MVF characterization

Ad-MVF have previously been described as biologically intact vascularization units that can be used for the prevascularization of matrices [FRUEH et al., 2016]. Of interest, studies have also shown that network formation and vascular remodeling are markedly affected in implanted matrices, which were seeded with ad-MVF from aged donors when compared to younger ones [LASCHKE et al., 2014]. Therefore, in the **first set of experiments** it was hypothesized that older mice also contain reduced volumes of adipose tissue as well as lower numbers of ad-MVF when compared to younger animals. However, it could be demonstrated that mice between the age of 7 - 12 months exhibited a comparable volume of adipose tissue as well as a comparable number of ad-MVF isolated from 1 mL adipose tissue. Furthermore, the average length of fragments was found to be ~ 38 μ m in all age groups. Moreover, the analysis of length distribution of ad-MVF revealed that ~ 70 % of all counted ad-MVF exhibited a length of 21 – 50 μ m. These results indicate that the age of the donor animal does not affect the outcome of ad-MVF isolation. Further flow cytometric analyses also showed a comparable cellular composition of ad-MVF from the donor mice of different ages, containing endothelial cells and perivascular cells as well as cells that

expressed the stem cell surface markers CD90 and CD177. Particularly the latter ones have been reported to exhibit a high regenerative and angiogenic potential [LI et al., 2003; LI et al., 2005; OISHI and ITO-DUFROS, 2006]. Taken together it can be concluded that the available volume of donor fat as well as the composition of isolated ad-MVF is identical when harvested from animals of the tested age range. Hence, it can be assumed that the seeding of MWD or FWM with ad-MVF isolated from donor mice within the age range of 7 - 12 months can be conducted in a very standardized manner.

7.2.2. MWD vs. FWM

In clinical practice, MWD represents a well-established dermal substitute for the filling of full-thickness skin defects. More recently, Integra Life Sciences has also developed the injectable FWM, which is especially suitable for the treatment of complex skin defects, such as tunneling wounds with anomalous geometries [CAMPITIELLO et al., 2015]. However, there is a lack of preclinical studies comparing the *in vitro* and *in vivo* properties of these matrices, which should exhibit an identical material composition. For this reason, the aim of the **second set of experiments** was to clarify whether MWD and FWM exhibit different pore sizes and surface topographies due to their differences in sample preparation. Of interest, *in vitro* analyses of both materials revealed an average inter-fiber distance of ~ 45 μm . This may be particularly indicated for the regeneration of skin defects. In fact, CHOI et al. [2013] showed that matrices with small pores < 200 μm are known to support the development of dense vascular networks with small vessels and poor penetration depth, as found in skin under physiological conditions. Fiber diameter and fiber length were comparable in both matrices as well. These findings indicate that the varying sample preparation of both matrices does not alter their structural properties. However, scanning electron microscopy revealed that the surface topography differed between MWD and FWM. FWM presented an irregular and fissured surface when compared to the more planar surface of the sheet-like MWD. This was most likely due to the fact that the gel-like consistency of FWM did not allow this matrix to keep a stable form. This difference in the consistency between MWD and FWM may markedly affect the porous architecture of both materials after their press-fit implantation into full-thickness skin defects, resulting in different biological host tissue responses after implantation.

To test this, non-seeded MWD and FWM were next implanted into full-thickness skin defects within dorsal skinfold chambers of C57BL/6 recipient mice. Epi-illumination light microscopy revealed a comparable epithelialization of both matrices over time. In addition, it could be demonstrated that vascularized tissue progressively grew into the pores of MWD and FWM. Of interest, a dense granulation tissue could exclusively be detected within the border zones

of both matrices at the end of the 2-week observation period. Additionally, both matrices exhibited a comparably low microvessel density and collagen ratio, indicating a rather slow incorporation. These rather negative findings should be interpreted with caution when it comes to the application of the matrices in clinical practice. In fact, based on their skin anatomies, there are major distinctions between the healing mechanisms and kinetics of wounds in mice and humans [LINDBLAD, 2008; RITTIÉ, 2016]. For example, human skin exhibits a much thicker epidermis and a higher vascularization when compared to the skin of mice. Hence, the results of this experimental section may not directly reflect the incorporation of MWD and FWM in human wounds.

The implantation of biomaterials, such as MWD or FWM, usually causes a foreign body reaction, which is associated with the infiltration of various immune cells [ANDERSON et al., 2008]. Particularly in the initial phase, activated polymorphonuclear leukocytes and macrophages are recruited from the blood stream to release numerous cytokines and growth factors at the site of implantation [GARASH et al., 2016]. Noteworthy, this process is similar to the inflammatory phase of wound healing [REINKE and SORG, 2012]. Hence, the inflammatory tissue response to MWD and FWM was analyzed as an indicator of both matrices' biocompatibility, which is defined as "the ability of a material to perform with an appropriate host response in a specific application" [VAN WACHEM et al., 1994; RATNER, 2011]. During the initial phase of implantation, it could be demonstrated that the matrices were not only primarily infiltrated by neutrophilic granulocytes but also macrophages and lymphocytes. However, there were no significant differences between the two matrices, indicating a comparable *in vivo* biocompatibility.

Taken together, the first part of this second section did not reveal significant differences in the *in vivo* performances of MWD and FWM in a standardized wound healing model. Although these findings indicate that both matrices may be equally suitable for clinical use, the injectable FWM may pave the way for innovative concepts in the area of tissue engineering and regenerative medicine by allowing a more homogeneous incorporation and distribution of bioactive molecules and cells within this gel-like material.

Previous studies have shown that ad-MVF are mainly trapped in the surface layers of MWD [FRUEH et al., 2016]. In this experimental section it was further hypothesized that a more homogeneous distribution of ad-MVF may be possible within FWM due to its differing sample preparation and, hence, lead to an improved matrix vascularization and incorporation. In a first *in vitro* analysis it was confirmed that ad-MVF could be distributed more homogeneously within FWM when compared to MWD. However, this did not result in an improved

vascularization and incorporation after implantation into full-thickness skin defects within dorsal skinfold chambers of GFP⁻ C57BL/6 recipient mice. This was most likely caused by an elevated distance between individual fragments. Actually, both matrices were seeded with a comparable number of ~ 15,000 ad-MVF. Accordingly, the more homogeneous distribution of individual ad-MVF within FWM was associated with a ~ 15-fold higher inter-fragment distance. Hence, individual ad-MVF needed more time to bridge the wider distances between each other. This, in turn, prolonged the process of reassembly into newly developing microvascular networks. Accordingly, when compared to FWM, the blood perfusion of ad-MVF-seeded MWD was sped up and improved in the early stage after implantation, as indicated by a higher centerline RBC velocity and wall shear rate of individual microvessels. This could have resulted in an increased survival rate of individual ad-MVF. In accordance with this view, MWD showed a diminished number of apoptotic cells on day 6 as well as a lower fraction of CD31⁺/GFP⁺ microvessels at the end of the 2-week observation period. Ultimately, histological and immunohistochemical analyses revealed that most pores of ad-MVF-seeded MWD were filled with a densely vascularized granulation tissue at the end of the *in vivo* observation period, indicating a good matrix incorporation into the surrounding host tissue. This was further confirmed by an increased proliferation rate and collagen content as well as an accelerated epithelialization over time when compared to ad-MVF-seeded FWM. Taken together, these findings demonstrate that a locally limited and high seeding density of ad-MVF is already sufficient to achieve a rapid matrix vascularization.

Lastly, it may be assumed that it is possible to further improve the vascularization of FWM by means of seeding an increased number of ad-MVF. This, in turn, may shorten the distance between individual ad-MVF and, thus, allow them to rapidly reassemble into microvascular networks. However, for this the needed volume of donor fat tissue may not always be available in patients. Therefore, ad-MVF-seeded FWM may be specifically recommended as an injectable carrier for the filling of small and hardly to access wounds with anomalous and irregular geometries, for which relatively low amounts of donor fat tissue would be necessary. In contrast, ad-MVF-seeded MWD may rather serve for the coverage of large skin defects, such as caused by extensive burns.

7.2.3. Ad-MVF seeding density

In this **third set of experiments** it was hypothesized that the seeding density of ad-MVF is a crucial determinant for the adequate vascularization and incorporation of matrices. To test this, MWD was seeded with three different densities of ad-MVF and implanted into full-thickness skin defects of GFP⁻ C57BL/6 recipient mice. Noteworthy, the seeding of ~ 120,000 ad-MVF/cm² MWD has been previously shown to be sufficient for an adequate matrix

vascularization and incorporation [FRUEH et al., 2017]. This density corresponded to the density of the HD ad-MVF-seeded control group of this experimental section.

Especially in case of severe burn injuries affecting large surface areas of the body [SUPP and BOYCE, 2005], the available amount of adipose donor tissue for the isolation of ad-MVF may be limited. Taking this into account, the findings of this third set of experiments show that only $\sim 80,000$ ad-MVF/cm² MWD, corresponding to the MD group, are needed to assure a sufficient vascularization and incorporation. In contrast, reducing the number of ad-MVF to only $\sim 40,000$ /cm² MWD, corresponding to the LD group, results in an insufficient matrix vascularization and incorporation, as indicated by the lack of a vascularized granulation tissue within the center zones of the matrices. Using intravital fluorescence microscopy, it was further demonstrated that HD- and MD-seeded MWD exhibit a comparable vascularization over time, whereas LD ad-MVF-seeded MWD is characterized by a significantly reduced number of perfused ROIs and a reduced microvessel density. In addition, photoacoustic analyses revealed lower O₂ levels within LD ad-MVF-seeded MWD on day 14 after implantation. This reduced oxygenation, in turn, may lead to an impaired engraftment of STSG under clinical conditions.

The process of ad-MVF reassembly not only includes the interconnection of single ad-MVF with each other but also the development of anastomoses with the blood vessels of the surrounding host tissue. The latter mechanism leads to an early onset of blood perfusion, while newly developing microvascular networks within the matrices have not been fully established yet and, thus, allow an increased leakage of blood. Accordingly, hemorrhages could be found within the matrices of all three groups, mostly pronounced between day 6 and 10 after implantation. Moreover, the delayed onset of blood perfusion in LD ad-MVF-seeded MWD was associated with less bleedings on day 6. Noteworthy, the extent of hemorrhages in all experimental groups decreased again towards day 14. This can be explained by the continuous stabilization of the newly developing microvascular networks, as indicated by decreased vessel diameters as well as elevated centerline RBC velocities and wall shear rates of individual microvessels.

Immunohistochemical analyses revealed that the pores in the center of both HD and MD ad-MVF-seeded matrices were filled with a vascularized granulation tissue. LD ad-MVF-seeded matrices, on the other hand, mainly contained infiltrated single cells. As anticipated, LD ad-MVF-seeded matrices further showed a significantly reduced density of CD31⁺ microvessels. However, the fraction of GFP⁺ microvessels was comparable in all three groups, indicating that even in the poorly vascularized LD group ad-MVF survived throughout the observation

period of 14 days. The overall correlation between a low ad-MVF seeding density and a reduced ingrowth of blood vessels may be explained by decreased levels of pro-angiogenic factors, such as VEGF and bFGF, within the matrices. Previous studies have shown that isolated ad-MVF release relevant amounts of these factors, which considerably participate to the high angiogenic activity of ad-MVF after *in vivo* implantation [LASCHKE et al., 2012]. In this context, it should also be taken into account that there is a close connection between angiogenesis and inflammation [FIEDLER et al., 2006; DIPIETRO, 2016]. Pro-angiogenic factors are capable of acting as chemokines for the recruitment of immune cells [KHOURY and ZIYADEH, 2011; BARBAY et al., 2015]. Accordingly, histological analyses revealed comparable numbers of MPO⁺ neutrophilic granulocytes, CD68⁺ macrophages, and CD3⁺ lymphocytes in HD and MD ad-MVF-seeded MWD. Since immune cell infiltration is a key event in wound healing [REINKE and SORG, 2012] and adequate matrix integration [ANDERSON et al., 2008], this may have further contributed to the improved incorporation of HD and MD ad-MVF-seeded MWD, which ultimately showed a higher collagen content and an increased surface epithelialization when compared to LD ad-MVF-seeded MWD.

Taken together, this third set of experiments demonstrates that a reduction from ~ 120,000 to ~ 80,000 ad-MVF/cm² MWD does not alter the vascularization and incorporation of the matrix after implantation into full-thickness skin defects. These novel findings demonstrate that 33 % less adipose tissue are needed for the isolation of ad-MVF required for a quick and adequate vascularization of MWD. Under clinical conditions, this may be especially important for the treatment of patients with extensive skin defects and/or limited availability of adipose tissue.

7.2.4. Ad-MVF vs. SVF single cells

Besides the herein described novel ad-MVF-based approach, another common prevascularization strategy is the seeding of SVF single cells, which represent a heterogeneous mixture of endothelial cells, pericytes, smooth muscle cells, and various stem cells [BOURIN et al., 2013; HASSAN et al., 2014; MAIJUB et al., 2015; CERINO et al., 2017; LOCKHART et al., 2017]. Of interest, such a SVF single cell-based prevascularization is already evaluated in clinical trials for the regeneration of bone fractures or the treatment of idiopathic pulmonary fibrosis [TZOUVELEKIS et al., 2013; CHARLES-DE-SÁ et al., 2015; RIGOTTI et al., 2016; SAXER et al., 2016]. However, after their seeding onto matrices, SVF single cells form a microvasculature *de novo* by reassembling into new blood vessels. In contrast, the fully functional ad-MVF rapidly interconnect to each other or the surrounding host tissue, leading to a rapid creation of new vascular networks. Accordingly, it was hypothesized that the ad-MVF-based prevascularization is superior to the prevascularization with the SVF. To

test this hypothesis, identical amounts of adipose tissue were used for the isolation of both ad-MVF and SVF single cells to ensure an identical cell load per matrix, and, thus to guarantee a standardized comparison of the vascularization potential between the SVF and ad-MVF. However, a longer enzymatic digestion time was needed for the disassembly of fat tissue into SVF single cells. Hence, the longer exposure of the tissue to collagenase could explain the reduced cell viability of SVF single cells when compared to ad-MVF. These results are in line with previous studies, indicating a ranging viability of SVF single cells between 80 - 83 % [DOI et al., 2013; PRINS et al., 2016].

Of interest, commercially available devices for the separation of the SVF from lipoaspirates exhibit a great heterogeneity regarding the outcome of the isolates' cellular composition [ARONOWITZ and ELLENHORN, 2013]. In contrast, flow cytometric analyses of this experimental section revealed that the SVF and ad-MVF are comparable mixtures of endothelial cells, perivascular cells, adipocytes, and stem cells. Although this heterogeneous composition may complicate the standardization of the method for a broad clinical application, it also bears a major advantage. Unlike purified cell isolations, the isolation of the SVF and ad-MVF is not associated with any complex cell separation or manipulative cultivation steps, which may facilitate the fulfillment of regulatory criteria for clinical approval.

For *in vivo* analyses, ad-MVF and SVF-seeded MWD were implanted into full-thickness skin defects within dorsal skinfold chambers of GFP⁺ C57BL/6 mice to analyze their vascularization and incorporation. Of interest, both matrices already exhibited first blood-perfused microvessels on day 6 after implantation. At this time point, hemorrhage formation was mostly pronounced, probably caused by an increased leakage of blood from immature microvessels. As a typical sign of microvascular maturation, the diameter of these microvessels decreased over time while their centerline RBC velocity and wall shear rate increased. Although these characteristics did not differ between both groups, a significantly higher number of perfused ROIs and a higher functional microvessel density were found in the border zones of ad-MVF-seeded MWD. This can be explained by the fact that ad-MVF already represent fully functional arteriolar, capillary, and venular segments that develop interconnections with each other and the surrounding microvasculature of the host tissue via the process of inosculation to establish a rapid blood perfusion within the implants [FRUEH et al., 2017]. In contrast, KOH et al. [2011] showed that the endothelial cells within SVF suspensions first reassemble into new vessel channels as a precondition for the subsequent formation of microvascular networks. Accordingly, much more time is required to complete this process when compared to the ad-MVF-based vascularization. In this context it should be further noted that ad-MVF exhibit a length of up to 150 μm [SPÄTER et al., 2017] enabling

the direct bridging of rather wide distances within tissue constructs in a short period. Accordingly, ad-MVF promote a more homogeneous blood perfusion within the border and center zones of implanted matrices. Of interest, the difference in vascularization between the SVF and ad-MVF group was most pronounced in the center of the implants, where > 90 % of all detected microvessels originated from the seeded GFP⁺ SVF or ad-MVF. UTZINGER et al. [2015] showed that the physiological growth rate of microvessels is ~ 5 µm/h. Hence, host vessels are mainly expected to occur in the border zones of the matrices. In these regions, SVF- and ad-MVF-seeded matrices contained a fraction of ~ 30 % and ~ 10 % GFP⁻ microvessels, respectively. Since the detected microvessel density within ad-MVF-seeded matrices was ~ 3-fold higher, these immunohistochemical findings demonstrate a comparable number of ingrowing GFP⁻ microvessels from the surrounding host tissue into both implant types. The epithelialization of both matrices was also found to be comparable. This may be explained by the fact, that both SVF- and ad-MVF-seeded matrices initially contained an identical cellular load and composition, leading to a comparable release of growth factors, which stimulated the vascularization-independent coverage with ingrowing keratinocytes from the edges of the wound.

Taken together, the findings of this fourth experimental section demonstrate several important advantages of ad-MVF for the prevascularization of matrices when compared to the SVF. The faster isolation of ad-MVF may allow their application in a less time-consuming intra-operative procedure while exhibiting a higher viability due the shorter enzymatic digestion time. This, in turn, may markedly contribute to an enhanced cell yield and, thus, to reduced volumes of adipose tissue needed for individual patient treatments. Finally, ad-MVF already represent fully functional vessel segments that markedly accelerate and improve the vascularization of matrices. In conclusion, all these unique features of ad-MVF suggest their future clinical use as vascularization units in tissue engineering.

7.2.5. Enox treatment

Enox is a frequently used LMWH for the thromboprophylactic therapy of hospitalized patients. Of interest, enox not only exerts anti-coagulative effects but also anti-angiogenic activity. In fact, enox has been shown to inhibit endothelial cell proliferation, sprouting, and tube formation *in vitro* [MARCHETTI et al., 2008; MOUSA, 2013]. *In vivo*, enox suppresses blood vessel formation in the chorioallantois membrane model [DOGAN et al., 2011; MOUSA, 2013] and tumor angiogenesis [DEBERGH et al., 2015]. Based on these findings it was herein speculated that enox treatment may also prevent the sprouting and reassembly of individual ad-MVF into microvascular networks. However, it could be demonstrated that enox even promoted the vascularization of ad-MVF-seeded MWD, as indicated by a significantly higher

functional microvessel density on day 10 when compared to vehicle-treated controls. A reason for this observation could be the anti-coagulative effect of enox, which may prevent microthrombosis formation caused by ischemia and reperfusion-induced endothelial cell activation of ad-MVF. This prevention of thrombus formation could also be the reason why the onset of blood perfusion within the newly developed microvasculature was accelerated. Blood-perfused microvessels could already be detected within enox-treated, ad-MVF-seeded MWD on day 3 after implantation. In contrast, matrices in vehicle-treated animals did not show blood perfusion before day 6.

A successful coverage of full-thickness skin defects not only depends on a sufficient vascularization, but also on an intact vessel integrity of the graft bed. Accordingly, hematoma and seroma formation beneath the wound bed are common reasons for graft failure [BLUME et al., 2010]. To evaluate implant-induced bleeding, a hemorrhagic score was assessed. However, even though increased bleeding has been reported as a major side effect of LMWH treatment in patients, it was shown that the extent of bleeding in enox-treated matrices did not differ from that of vehicle-treated control matrices [NIEUWENHUIS et al., 1999; MARTEL et al., 2005]. These results show that enox-treatment does not increase the risk of bleeding caused by ad-MVF-seeded MWD, excluding the possibility for hematoma-caused graft failure.

As previously described, there is a correlation between the vascularization of implanted MWD within full-thickness skin defects and its incorporation into the surrounding host tissue [FRUEH et al., 2017]. This incorporation was herein evaluated by the development of a vascularized granulation tissue, the formation of collagen fibers, and epithelialization over time. In line with the finding that matrices in enox- and vehicle-treated animals exhibited a comparable microvessel density, this experimental section showed that none of the above listed processes showed significant differences between the two experimental groups.

Taken together, this experimental section shows that enox-treatment does neither alter vascularization nor hemorrhage formation within ad-MVF-seeded MWD. Hence, it can be summarized that ad-MVF may also be used as vascularization units for dermal skin substitutes during routinely applied thromboprophylactic therapy of hospitalized patients.

7.3. Conclusion and clinical perspectives

The aim of the present doctoral thesis was to test several hypotheses, which are of crucial importance for transferring the novel approach of ad-MVF-based matrix prevascularization into clinical practice. The results shown in this work strongly indicate the high regenerative potential of ad-MVF over single cell-based approaches for future tissue engineering strategies [SPÄTER et al., 2017a; 2017b; 2018a; 2018b]. After their seeding onto MWD, ad-MVF, which represent fully functional vessel segments, are able to interconnect with each other as well as with the microvasculature of the surrounding host tissue, resulting in a rapid formation of blood-perfused networks.

In future studies it may be very interesting to analyze the vascularization potential of human ad-MVF. This could be done by isolating ad-MVF from liposuctioned adipose tissue of patients. The isolated ad-MVF could then be seeded onto MWD and subsequently be implanted into full-thickness skin defects within immunodeficient mice to analyze the vascularization and incorporation of the seeded matrix without the risk of rejection.

Besides the possible use of ad-MVF as prevascularization units for dermal substitutes, these vessel segments may also be suitable for the prevascularization of other implants, constructs or tissues. For example, ad-MVF may be injected into fracture gaps to enhance bone healing or to prevent the development of non-unions, i.e. the permanent failure of broken bones to heal without surgical intervention. Moreover, ad-MVF may be used for the prevascularization of spheroids, which represent three-dimensional cell clusters that are generated by cellular self-assembly *in vitro*. Of interest, when compared to two-dimensional single cell approaches, spheroids exhibit increased proliferation activity, enhanced cellular viability, and improved physiological metabolic functions [LASCHKE and MENGER, 2017]. Due to these advantages, spheroids are increasingly used as building blocks in tissue engineering and regenerative medicine. Since the cells in the core of spheroids are typically exposed to hypoxic conditions [PEDRAZA et al., 2011], it may be an advantage to prevascularize the spheroids with ad-MVF prior to their *in vivo* implantation. This could lead to an improved cellular survival rate, especially within their core areas.

Taken together, the present doctoral thesis demonstrates the high vascularization capacity of ad-MVF within an experimental mouse model. Additional translational studies should now be conducted to further pave the way for these promising prevascularization units into clinical practice.

8. References

1. **Algire GH.** An adaption of the transparent chamber technique to the mouse. *J Natl Cancer Inst USA* 4: 1-11, 1943.
2. **Alrubaiy L, Al-Rubaiy KK.** Skin substitutes: a brief review of types and clinical applications. *Oman Med J* 24: 4-6, 2009.
3. **Anderson JM, Rodriguez A, Chang DT.** Foreign body reaction to biomaterials. *Semin Immunol* 20: 86-100, 2008.
4. **Aronowitz JA, Ellenhorn JD.** Adipose stromal vascular fraction isolation: a head-to-head comparison of four commercial cell separation systems. *Plast Reconstr Surg* 132: 932e-939e, 2013.
5. **Auger FA, Gibot L, Lacroix D.** The pivotal role of vascularization in tissue engineering. *Annu Rev Biomed Eng* 15: 177-200, 2013.
6. **Baffour R, Berman J, Garb JL, Rhee SW, Kaufman J, Friedmann P.** Enhanced angiogenesis and growth of collaterals by in vivo administration of recombinant basic fibroblast growth factor in a rabbit model of acute lower limb ischemia: dose-response effect of basic fibroblast growth factor. *J Vasc Surg* 16: 181-191, 1992.
7. **Barbay V, Houssari M, Mekki M, Banquet S, Edwards-Lévy F, Henry JP, Dumesnil A, Adriouch S, Thuillez C, Richard V, Brakenhielm E.** Role of M2-like macrophage recruitment during angiogenic growth factor therapy. *Angiogenesis* 18: 191-200, 2015.
8. **Baron VT, Welsh J, Abedinpour P, Borgström P.** Intravital microscopy in the mouse dorsal chamber model for the study of solid tumors. *Am J Cancer Res* 1: 674-686, 2011.
9. **Baroni A, Buommino E, De Gregorio V, Ruocco E, Ruocco V, Wolf R.** Structure and function of the epidermis related to barrier properties. *Clin Dermatol* 30: 257-262, 2012.
10. **Bellas E, Seiberg M, Garlick J, Kaplan DL.** In vitro 3D full-thickness skin-equivalent tissue model using silk and collagen biomaterials. *Macromol Biosci* 12: 1627-1636, 2012.

11. **Bergqvist D, Agnelli G, Cohen AT, Eldor A, Nilsson PE, Le Moigne-Amrani A, Dietrich-Neto F.** Duration of prophylaxis against venous thromboembolism with enoxaparin after surgery for cancer. *N Engl J Med* 346: 975-980, 2002.
12. **Bergqvist D, Benoni G, Björgell O, Fredin H, Hedlundh U, Nicolas S, Nilsson P, Nylander G.** Low-molecular-weight heparin (enoxaparin) as prophylaxis against venous thromboembolism after total hip replacement. *N Engl J Med* 335: 696-700, 1996.
13. **Blanco R, Gerhardt H.** VEGF and Notch in tip and stalk cell selection. *Cold Spring Harb Perspect Med* 3: a006569, 2013.
14. **Blume PA, Key JJ, Thakor P, Thakor S, Sumpio B.** Retrospective evaluation of clinical outcomes in subjects with split-thickness skin graft: comparing V.A.C[®] therapy and conventional therapy in foot and ankle reconstructive surgeries. *Int Wound J* 7: 480-487, 2010.
15. **Böttcher-Haberzeth S, Biedermann T, Reichmann E.** Tissue engineering of skin. *Burns* 36: 450-460, 2010.
16. **Boulaftali Y, Lamrani L, Rouzaud MC, Loyau S, Jandrot-Perrus M, Bouton MC, Ho-Tin-Noé B.** The mouse dorsal skinfold chamber as a model for the study of thrombolysis by intravital microscopy. *Thromb Haemost* 107: 962-971, 2012.
17. **Bourin P, Bunnell BA, Casteilla L, Dominici M, Katz AJ, March KL, Redl H, Rubin JP, Yoshimura K, Gimble JM.** Stromal cells from the adipose tissue-derived stromal vascular fraction and culture expanded adipose tissue-derived stromal/stem cells: a joint statement of the International Federation for Adipose Therapeutics and Science (IFATS) and the International Society for Cellular Therapy (ISCT). *Cytotherapy* 15: 641-648, 2013.
18. **Broze GJ Jr, Yin ZF, Lasky N.** A tail vein bleeding time model and delayed bleeding in hemophiliac mice. *Thromb Haemost* 85: 747-748, 2001.
19. **Campitiello F, Della Corte A, Guerniero R, Pellino G, Canonico S.** Efficacy of a new flowable wound matrix in tunneled and cavity ulcers: A preliminary report. *Wounds* 27: 152-157, 2015.

20. **Cangkrama M, Ting SB, Darido C.** Stem cells behind the barrier. *Int J Mol Sci* 14: 13670-13686, 2013.
21. **Cerino G, Gaudiello E, Muraro MG, Eckstein F, Martin I, Scherberich A, Marsano A.** Engineering of an angiogenic niche by perfusion culture of adipose-derived stromal vascular fraction cells. *Sci Rep* 7: 14252, 2017.
22. **Charles-de-Sá L, Gontijo-de-Amorim NF, Maeda Takiya C, Borojevic R, Benati D, Bernardi P, Sbarbati A, Rigotti G.** Antiaging treatment of the facial skin by fat graft and adipose-derived stem cells. *Plast Reconstr Surg* 135: 999-1009, 2015.
23. **Choi SW, Zhang Y, Macewan MR, Xia Y.** Neovascularization in biodegradable inverse opal scaffolds with uniform and precisely controlled pore sizes. *Adv Healthc Mater* 2: 145-154, 2013.
24. **Choussat R, Montalescot G, Collet JP, Vicaut E, Ankri A, Gallois V.** A unique, low dose of intravenous enoxaparin in elective percutaneous coronary intervention. *J Am Coll Cardiol* 40: 1943-1950, 2002.
25. **Clayton ZE, Sadeghipour S, Patel S.** Generating induced pluripotent stem cell derived endothelial cells and induced endothelial cells for cardiovascular disease modelling and therapeutic angiogenesis. *Int J Cardiol* 197: 116-122, 2015.
26. **Connolly SJ, Milling TJ Jr, Eikelboom JW, Gibson CM, Curnutte JT, Gold A, Bronson MD, Lu G, Conley PB, Verhamme P, Schmidt J, Middeldorp S, Cohen AT, Beyer-Westendorf J, Albaladejo P, Lopez-Sendon J, Goodman S, Leeds J, Wiens BL, Siegal DM, Zotova E, Meeks B, Nakamya J, Lim WT, Crowther M.** Andexanet alfa for acute major bleeding associated with factor Xa inhibitors. *N Engl J Med* 375: 1131-1141, 2016.
27. **Contaldo C, Meier C, Elsherbiny A, Harder Y, Trentz O, Menger MD, Wanner GA.** Human recombinant erythropoietin protects the striated muscle microcirculation of the dorsal skinfold from postischemic injury in mice. *Am J Physiol Heart Circ Physiol* 293: H274-H283, 2007.
28. **Curtis A, Calabro K, Galarneau JR, Bigio IJ, Krucker T.** Temporal variations of skin pigmentation in C57BL/6 mice affect optical bioluminescence quantitation. *Mol Imaging Biol* 13: 1114-1123, 2011.

29. **Daly CH.** Biomechanical properties of dermis. *J Invest Dermatol* 79 Suppl 1: 17s-20s, 1982.
30. **de Vries HJ, Middelkoop E, van Heemstra-Hoen M, Wildevuur CH, Westerhof W.** Stromal cells from subcutaneous adipose tissue seeded in a native collagen/elastin dermal substitute reduce wound contraction in full thickness skin defects. *Lab Invest* 73: 532-540, 1995.
31. **Debels H, Hamdi M, Abberton K, Morrison W.** Dermal matrices and bioengineered skin substitutes: a critical review of current options. *Plast Reconstr Surg Glob Open* 3: e284, 2015.
32. **Debergh I, Van Damme N, Pattyn P, Peeters M, Ceelen WP.** The low-molecular-weight heparin, nadroparin, inhibits tumour angiogenesis in a rodent dorsal skinfold chamber model. *Br J Cancer* 102: 837-843, 2010.
33. **Debergh I, Pattyn P, Ceelen W.** Microvascular effects of the low molecular weight heparins in a colorectal xenograft model: an intravital microscopy study. *J Surg Res* 194: 488-495, 2015.
34. **Dengler WA, Schulte J, Berger DP, Mertelsmann R, Fiebig HH.** Development of a propidium iodide fluorescence assay for proliferation and cytotoxicity assays. *Anticancer Drugs* 6: 522-532, 1995.
35. **DiPietro LA.** Angiogenesis and wound repair: when enough is enough. *J Leukoc Biol* 100: 979-984, 2016.
36. **Dockal M, Hartmann R, Fries M, Thomassen MC, Heinzmann A, Ehrlich H, Rosing J, Osterkamp F, Polakowski T, Reineke U, Griessner A, Brandstetter H, Scheiflinger F.** Small peptides blocking inhibition of factor Xa and tissue factor-factor VIIa by tissue factor pathway inhibitor (TFPI). *J Biol Chem* 289: 1732-1741, 2014.
37. **Dogan OT, Polat ZA, Karahan O, Epozturk K, Altun A, Akkurt I, Cetin A.** Antiangiogenic activities of bemiparin sodium, enoxaparin sodium, nadroparin calcium and tinzaparin sodium. *Thromb Res* 128: e29-e32, 2011.

38. **Doi K, Tanaka S, Iida H, Eto H, Kato H, Aoi N, Kuno S, Hirohi T, Yoshimura K.** Stromal vascular fraction isolated from lipo-aspirates using an automated processing system: bench and bed analysis. *J Tissue Eng Regen Med* 7: 864-870, 2013.
39. **Druecke D, Langer S, Lamme E, Pieper J, Ugarkovic M, Steinau HU, Homann HH.** Neovascularization of poly(ether ester) block-copolymer scaffolds in vivo: long-term investigations using intravital fluorescent microscopy. *J Biomed Mater Res A* 68: 10-18, 2004.
40. **Duttenhoefer F, Lara de Freitas R, Meury T, Loibl M, Benneker LM, Richards RG, Alini M, Verrier S.** 3D scaffolds co-seeded with human endothelial progenitor and mesenchymal stem cells: evidence of prevascularisation within 7 days. *Eur Cell Mater* 26: 49-64, 2013.
41. **Egaña JT, Danner S, Kremer M, Rapoport DH, Lohmeyer JA, Dye JF, Hopfner U, Lavandero S, Kruse C, Machens HG.** The use of glandular-derived stem cells to improve vascularization in scaffold-mediated dermal regeneration. *Biomaterials* 30: 5918-5926, 2009.
42. **Esmon CT.** Targeting factor Xa and thrombin: impact on coagulation and beyond. *Thromb Haemost* 111: 625-633, 2014.
43. **Evers LH, Bhavsar D, Mailänder P.** The biology of burn injury. *Exp Dermatol* 19: 777-783, 2010.
44. **Fiedler U, Reiss Y, Scharpfenecker M, Grunow V, Koidl S, Thurston G, Gale NW, Witzenrath M, Rosseau S, Suttorp N, Sobke A, Herrmann M, Preissner KT, Vajkoczy P, Augustin HG.** Angiopoietin-2 sensitizes endothelial cells to TNF-alpha and has a crucial role in the induction of inflammation. *Nat Med* 12: 235-259, 2006.
45. **Formigli L, Paternostro F, Tani A, Mirabella C, Quattrini Li A, Nosi D, D'Asta F, Saccardi R, Mazzanti B, Lo Russo G, Zecchi-Orlandini S.** MSCs seeded on bioengineered scaffolds improve skin wound healing in rats. *Wound Repair Regen* 23: 115-123, 2015.
46. **Friesenecker B, Tsai AG, Instaglietta M.** Capillary perfusion during ischemia-reperfusion in subcutaneous connective tissue and skin muscle. *Am J Physiol* 267: H2204-H2212, 1994.

47. **Frueh FS, Calcagni M, Giesen T, Giovanoli P, Harder Y.** Das Management von Weichteilverletzungen im Extremitätentrauma: Die Rolle der Plastischen Chirurgie. *Praxis* 105: 1493-1501, 2016.
48. **Frueh FS, Später T, Lindenblatt N, Calcagni M, Giovanoli P, Scheuer C, Menger MD, Laschke MW.** Adipose tissue-derived microvascular fragments improve vascularization, lymphangiogenesis, and integration of dermal skin substitutes. *J Invest Dermatol* 137: 217-227, 2017.
49. **Garash R, Bajpai A, Marcinkiewicz BM, Spiller KL.** Drug delivery strategies to control macrophages for tissue repair and regeneration. *Exp Biol Med (Maywood)* 241: 1054-1063, 2016.
50. **Gerlach AT, Pickworth KK, Seth SK, Tanna SB, Barnes JF.** Enoxaparin and bleeding complications: a review in patients with and without renal insufficiency. *Pharmacotherapy* 20: 771-775, 2000.
51. **Graham GP, Helmer SD, Haan JM, Khandelwal A.** The use of Integra® dermal regeneration template in the reconstruction of traumatic degloving injuries. *J Burn Care Res* 34: 261-266, 2013.
52. **Green CJ, Knight J, Precious S, Simpkin S.** Ketamine alone and combined with diazepam or xylazine in laboratory animals: a 10 year experience. *Lab Anim* 15: 163-170, 1981.
53. **Greenwood J, Amjadi M, Dearman B, Mackie I.** Real-time demonstration of split skin graft inosculation and integra dermal matrix neovascularization using confocal laser scanning microscopy. *Eplasty* 9: e33, 2009.
54. **Griffith CK, Miller C, Sainson RC, Calvert JW, Jeon NL, Hughes CC, George SC.** Diffusion limits of an in vitro thick prevascularized tissue. *Tissue Eng* 11: 257-266, 2005.
55. **Gunin AG, Petrov VV, Golubtzova NN, Vasilieva OV, Kornilova NK.** Age-related changes in angiogenesis in human dermis. *Exp Gerontol* 55: 143-151, 2014.
56. **Hassan WU, Greiser U, Wang W.** Role of adipose-derived stem cells in wound healing. *Wound Repair Regen* 22: 313-325, 2014.

57. **Herrmann KS.** Platelet aggregation induced in the hamster cheek pouch by a photochemical process with excited fluorescein isothiocyanate-dextran. *Microvasc Res* 26: 238-249, 1983.
58. **Hirche C, Senghaas A, Fischer S, Hollenbeck ST, Kremer T, Kneser U.** Novel use of a flowable collagen-glycosaminoglycan matrix (Integra™ Flowable Wound Matrix) combined with percutaneous cannula scar tissue release in treatment of post-burn malfunction of the hand - A preliminary 6 month follow-up. *Burns* 42: e1-e7, 2016.
59. **Hiscox AM, Stone AL, Limesand S, Hoying JB, Williams SK.** An islet-stabilizing implant constructed using a preformed vasculature. *Tissue Eng Part A* 14: 433-440, 2008.
60. **Hoying JB, Boswell CA, Williams SK.** Angiogenic potential of microvessel fragments established in three-dimensional collagen gels. *In Vitro Cell Dev Biol Anim* 32: 409-419, 1996.
61. **Hulsen J, Diederich R, Neumeister MW, Bueno RA Jr.** Integra® dermal regenerative template application on exposed tendon. *HAND* 9: 539-542, 2014.
62. **Hunt JA, Moisidis E, Haertsch P.** Initial experience of Integra in the treatment of post-burn anterior cervical neck contracture. *Br J Plast Surg* 53: 652-658, 2000.
63. **Hur J, Yoon CH, Kim HS, Choi JH, Kang HJ, Hwang KK, Oh BH, Lee MM, Park YB.** Characterization of two types of endothelial progenitor cells and their different contributions to neovasculogenesis. *Arterioscler Thromb Vasc Biol* 24: 288-293, 2004.
64. **Hussain SH, Limthongkul B, Humphreys TR.** The biomechanical properties of the skin. *Dermatol Surg* 39: 193-203, 2013.
65. **Jeng JC, Fidler PE, Sokolich JC, Jaskille AD, Khan S, White PM, Street JH 3rd, Light TD, Jordan MH.** Seven years' experience with Integra as a reconstructive tool. *J Burn Care Res* 28: 120-126, 2007.
66. **Jensen UB, Lowell S, Watt FM.** The spatial relationship between stem cells and their progeny in the basal layer of human epidermis: a new view based on whole-mount labeling and lineage analysis. *Development* 126: 2409-2418, 1999.

67. **Johnstone CC, Farley A.** The physiological basics of wound healing. *Nurs Stand* 19: 59-65, 2005.
68. **Junqueira LC, Bignolas G, Brentani RR.** Picrosirius staining plus polarization microscopy, a specific method for collagen detection in tissue sections. *Cell Tissue Res* 202: 453-460, 1979.
69. **Jørgensen LN, Wille-Jørgensen P, Hauch O.** Prophylaxis of postoperative thromboembolism with low molecular weight heparins. *Br J Surg* 80: 689-704, 1993.
70. **Kakkar AK, Brenner B, Dahl OE, Eriksson BI, Mouret P, Muntz J, Sogliani AG, Pap AF, Misselwitz F, Haas S.** Extended duration rivaroxaban versus short-term enoxaparin for the prevention of venous thromboembolism after total hip arthroplasty: a double-blind, randomised controlled trial. *Lancet* 372: 31-39, 2008.
71. **Khan MA, Chipp E, Hardwicke J, Srinivasan K, Shaw S, Rayatt S.** The use of dermal regeneration template (Integra®) for reconstruction of a large full-thickness scalp and calvarial defect with exposed dura. *J Plast Reconstr Aesthet Surg* 63: 2168-2171, 2010.
72. **Khoury CC, Ziyadeh FN.** Angiogenic factors. *Contrib Nephrol* 170: 83-92, 2011.
73. **Kirsner RS, Eaglstein WH, Kerdel FA.** Split-thickness skin grafting for lower extremity ulcerations. *Dermatol Surg* 23: 85-91, 1997.
74. **Koh YJ, Koh BI, Kim H, Joo HJ, Jin HK, Jeon J, Choi C, Lee DH, Chung JH, Cho CH, Park WS, Ryu JK, Suh JK, Koh GY.** Stromal vascular fraction from adipose tissue forms profound vascular network through the dynamic reassembly of blood endothelial cells. *Arterioscler Thromb Vasc Biol* 31: 1141-1150, 2011.
75. **Kontos HA, Wei EP, Christman CW, Levasseur JE, Povlishock JT, Ellis EF.** Free oxygen radicals in cerebral vascular responses. *Physiologist* 26: 165-169, 1983.
76. **Laschke MW, Vollmar B, Menger MD.** Inosculation: connecting the life-sustaining pipelines. *Tissue Eng Part B Rev* 15: 455-465, 2009.
77. **Laschke MW, Vollmar B, Menger MD.** The dorsal skinfold chamber: window into the dynamic interaction of biomaterials with their surrounding host tissue. *Eur Cell Mater* 22: 147-164, 2011.

78. **Laschke MW, Menger MD.** Vascularization in tissue engineering: angiogenesis versus inosculation. *Eur Surg Res* 48: 85-92, 2012.
79. **Laschke MW, Kleer S, Scheuer C, Schuler S, Garcia P, Eglin D, Alini M, Menger MD.** Vascularisation of porous scaffolds is improved by incorporation of adipose tissue-derived microvascular fragments. *Eur Cell Mater* 24: 266-277, 2012.
80. **Laschke MW, Grässer C, Kleer S, Scheuer C, Eglin D, Alini M, Menger MD.** Adipose tissue-derived microvascular fragments from aged donors exhibit an impaired vascularisation capacity. *Eur Cell Mater* 28: 287-298, 2014.
81. **Laschke MW, Menger MD.** Adipose tissue-derived microvascular fragments: natural vascularization units for regenerative medicine. *Trends Biotechnol* 33: 442-448, 2015.
82. **Laschke MW, Menger MD.** Prevascularization in tissue engineering: Current concepts and future directions. *Biotechnol Adv* 34: 112-121, 2016.
83. **Laschke MW, Menger MD.** Life is 3D: Boosting spheroid function for tissue engineering. *Trends Biotechnol* 35: 133-144, 2017.
84. **Lassen MR, Bauer KA, Eriksson BI, Turpie AG.** Postoperative fondaparinux versus preoperative enoxaparin for prevention of venous thromboembolism in elective hip-replacement surgery: a randomised double-blind comparison. *Lancet* 359: 1715-1720, 2002.
85. **Lee AY, Levine MN, Baker RI, Bowden C, Kakkar AK, Prins M, Rickles FR, Julian JA, Haley S, Kovacs MJ, Gent M.** Low-molecular-weight heparin versus a coumarin for the prevention of recurrent venous thromboembolism in patients with cancer. *N Engl J Med* 349: 146-153, 2003.
86. **Lehr HA, Leunig M, Menger MD, Nolte D, Messmer K.** Dorsal skinfold chamber technique for intravital microscopy in nude mice. *Am J Pathol* 143: 1055-1062, 1993.
87. **Leizorovicz A, Haugh MC, Chapuis FR, Samama MM, Boissel JP.** Low molecular weight heparin in prevention of perioperative thrombosis. *BMJ* 305: 913-920, 1992.

88. **Li TS, Hamano K, Nishida M, Hayashi M, Ito H, Mikamo A, Matsuzaki M.** CD117+ stem cells play a key role in therapeutic angiogenesis induced by bone marrow cell implantation. *Am J Physiol Heart Circ Physiol* 285: H931-H937, 2003.
89. **Li TS, Ito H, Hayashi M, Furutani A, Matsuzaki M, Hamano K.** Cellular expression of integrin-beta 1 is of critical importance for inducing therapeutic angiogenesis by cell implantation. *Cardiovasc Res* 65: 64-72, 2005.
90. **Lindblad WJ.** Considerations for selecting the correct animal model for dermal wound-healing studies. *J Biomater Sci Polym Ed* 19: 1087-1096, 2008.
91. **Lockhart RA, Aronowitz JA, Dos-Anjos Vilaboa S.** Use of freshly isolated human adipose stromal cells for clinical applications. *Aesthet Surg J* 37: S4-S8, 2017.
92. **MacNeil S.** Progress and opportunities for tissue-engineered skin. *Nature* 445: 874-880, 2007.
93. **Maijub JG, Boyd NL, Dale JR, Hoying JB, Morris ME, Williams SK.** Concentration-dependent vascularization of adipose stromal vascular fraction cells. *Cell Transplant* 24: 2029-2039, 2015.
94. **Marchetti M, Vignoli A, Russo L, Balducci D, Pagnoncelli M, Barbui T, Falanga A.** Endothelial capillary tube formation and cell proliferation induced by tumor cells are affected by low molecular weight heparins and unfractionated heparin. *Thromb Res* 121: 637-645, 2008.
95. **Marin-Bañasco C, Suardíaz García M, Hurtado Guerrero I, Maldonado Sánchez R, Estivill-Torrús G, Leyva Fernández L, Fernández Fernández O.** Mesenchymal properties of SJL mice-stem cells and their efficacy as autologous therapy in a relapsing-remitting multiple sclerosis model. *Stem Cell Res Ther* 5: 134, 2014.
96. **Martel N, Lee J, Wells PS.** Risk for heparin-induced thrombocytopenia with unfractionated and low-molecular-weight heparin thromboprophylaxis: a meta-analysis. *Blood* 106: 2710-2715, 2005.

97. **McLeod RS, Geerts WH, Sniderman KW, Greenwood C, Gregoire RC, Taylor BM, Silverman RE, Atkinson KG, Burnstein M, Marshall JC, Burul CJ, Anderson DR, Ross T, Wilson SR, Barton P.** Subcutaneous heparin versus low-molecular-weight heparin as thromboprophylaxis in patients undergoing colorectal surgery: results of the canadian colorectal DVT prophylaxis trial: a randomized, double-blind trial. *Ann Surg* 233: 438-444, 2001.
98. **McDaniel JS, Pilia M, Ward CL, Pollot BE, Rathbone CR.** Characterization and multilineage potential of cells derived from isolated microvascular fragments. *J Surg Res* 192: 214-222, 2014.
99. **Meruane MA, Rojas M, Marcelain K.** The use of adipose tissue-derived stem cells within a dermal substitute improves skin regeneration by increasing neoangiogenesis and collagen synthesis. *Plast Reconstr Surg* 130: 53-63, 2012.
100. **Moroni L, Licht R, de Boer J, de Wijn JR, van Blitterswijk CA.** Fiber diameter and texture of electrospun PEOT/PBT scaffolds influence human mesenchymal stem cell proliferation and morphology, and the release of incorporated compounds. *Biomaterials* 27: 4911-4922, 2006.
101. **Mousa SA.** Comparative pharmacodynamic assessment of the antiangiogenesis activity of heparin and low-molecular-weight heparin fractions: structure-function relationship. *Clin Appl Thromb Hemost* 19: 48-54, 2013.
102. **Nakano M, Nakajima Y, Kudo S, Tsuchida Y, Nakamura H, Fukuda O.** Effect of autotransplantation of microvessel fragments on experimental random-pattern flaps in the rat. *Eur Surg Res* 30: 149-160, 1998.
103. **Nakano M, Nakajima Y, Kudo S, Tsuchida Y, Nakamura H, Fukuda O.** Successful autotransplantation of microvessel fragments into the rat heart. *Eur Surg Res* 31: 240-248, 1999.
104. **Nieuwenhuis HK, Albada J, Banga JD, Sixma JJ.** Identification of risk factors for bleeding during treatment of acute venous thromboembolism with heparin or low molecular weight heparin. *Blood* 78: 2337-2343, 1991.
105. **Nguyen DQ, Potokar TS, Price P.** An objective long-term evaluation of Integra (a dermal skin substitute) and split thickness skin grafts, in acute burns and reconstructive surgery. *Burns* 36: 23-28, 2010.

106. **Norman AW.** Sunlight, season, skin pigmentation, vitamin D, and 25-hydroxyvitamin D: integral components of the vitamin D endocrine system. *Am J Clin Nutr* 67: 1108-1110, 1998.
107. **Oishi K, Ito-Dufros Y.** Angiogenic potential of CD44+ CD90+ multipotent CNS stem cells in vitro. *Biochem Biophys Res Commun* 349: 1065-1072, 2006.
108. **Okabe M, Ikawa M, Kominami K, Nakanishi T, Nishimune Y.** 'Green mice' as a source of ubiquitous green cells. *FEBS Lett* 407: 313-319, 1997.
109. **Papenfuss HD, Gross JF, Intaglietta M, Treese FA.** A transparent access chamber for the rat dorsal skin fold. *Microvasc Res* 18: 311-318, 1979.
110. **Papini R.** Management of burn injuries of various depths. *BMJ* 329: 158-160, 2004.
111. **Pedraza E, Coronel MM, Fraker CA, Ricordi C, Stabler CL.** Preventing hypoxia-induced cell death in beta cells and islets via hydrolytically activated, oxygen-generating biomaterials. *Proc Natl Acad Sci U S A* 109: 4245-4250, 2011.
112. **Petersen JL, Mahaffey KW, Hasselblad V, Antman EM, Cohen M, Goodman SG, Langer A, Blazing MA, Le-Moigne-Amrani A, de Lemos JA, Nessel CC, Harrington RA, Ferguson JJ, Braunwald E, Califf RM.** Efficacy and bleeding complications among patients randomized to enoxaparin or unfractionated heparin for antithrombin therapy in non-ST-Segment elevation acute coronary syndromes: a systematic overview. *JAMA* 292: 89-96, 2004.
113. **Petite H, Viateau V, Bensaïd W, Meunier A, de Pollak C, Bourguignon M, Oudina K, Sedel L, Guillemain G.** Tissue-engineered bone regeneration. *Nat Biotechnol* 18: 959-963, 2000.
114. **Pilia M, McDaniel JS, Guda T, Chen XK, Rhoads RP, Allen RE, Corona BT, Rathbone CR.** Transplantation and perfusion of microvascular fragments in a rodent model of volumetric muscle loss injury. *Eur Cell Mater* 28: 11-23, 2014.
115. **Pill K, Hofmann S, Redl H, Holnthoner W.** Vascularization mediated by mesenchymal stem cells from bone marrow and adipose tissue: a comparison. *Cell Regen (Lond)* 4: 8, 2015.

116. **Plonka PM, Michalczyk D, Popik M, Handjiski B, Slominski A, Paus R.** Splenic eumelanin differs from hair eumelanin in C57BL/6 mice. *Acta Biochim Pol* 52: 433-441, 2005.
117. **Prins HJ, Schulten EA, Ten Bruggenkate CM, Klein-Nulend J, Helder MN.** Bone regeneration using the freshly isolated autologous stromal vascular fraction of adipose tissue in combination with calcium phosphate ceramics. *Stem Cells Transl Med* 5: 1362-1374, 2016.
118. **Rabah MM, Premmereur J, Graham M, Fareed J, Hoppensteadt DA, Grines LL, Grines CL.** Usefulness of intravenous enoxaparin for percutaneous coronary intervention in stable angina pectoris. *Am J Cardiol* 84: 1391-1395, 1999.
119. **Radhika T, Sekaran P, Narasimhan M.** Qualitative analysis of collagen fibers in oral submucous fibrosis using picosirius red stain and polarising microscope. *J Clin Diagn Res* 10: ZC04-ZV07, 2016.
120. **Ratner BD.** The biocompatibility manifesto: biocompatibility for the twenty-first century. *J Cardiovasc Transl Res* 4: 523-527, 2011.
121. **Reagan-Shaw S, Nihal M, Ahmad N.** Dose translation from animal to human studies revisited. *FASEB J* 22: 659-661, 2008.
122. **Reid MJ, Currie LJ, James SE, Sharpe JR.** Effect of artificial dermal substitute, cultured keratinocytes and split thickness skin graft on wound contraction. *Wound Repair Regen* 15: 889-896, 2007.
123. **Reiffel AJ, Henderson PW, Krijgh DD, Belkin DA, Zheng Y, Bonassar LJ, Stroock AD, Spector JA.** Mathematical modeling and frequency gradient analysis of cellular and vascular invasion into integrin and strattice: toward optimal design of tissue regeneration scaffolds. *Plast Reconstr Surg* 129: 89-99, 2012.
124. **Reinke JM, Sorg H.** Wound repair and regeneration. *Eur Surg Res* 49: 35-43, 2012.
125. **Rich LJ, Seshadri M.** Photoacoustic imaging of vascular hemodynamics: validation with blood oxygenation level-dependent MR imaging. *Radiology* 275: 110-118, 2015.

126. **Rigotti G, Charles-de-Sá L, Gontijo-de-Amorim NF, Takiya CM, Amable PR, Borojevic R, Benati D, Bernardi P, Sbarbati A.** Expanded stem cells, stromal-vascular fraction, and platelet-rich plasma enriched fat: comparing results of different facial rejuvenation approaches in a clinical trial. *Aesthet Surg J* 36: 261-270, 2016.
127. **Rittié L.** Cellular mechanisms of skin repair in humans and other mammals. *J Cell Commun Signal* 10: 103-120, 2016.
128. **Rondina MT, Wheeler M, Rodgers GM, Draper L, Pendleton RC.** Weight-based dosing of enoxaparin for VTE prophylaxis in morbidly obese, medically-ill patients. *Thromb Res* 125: 220-223, 2010.
129. **Ruszczak Z.** Effect of collagen matrices on dermal wound healing. *Adv Drug Deliv Rev* 55: 1595-1611, 2003.
130. **Saetzler RK, Jallo J, Lehr HA, Philips CM, Vasthare U, Arfors KE, Tuma RF.** Intravital fluorescence microscopy: impact of light-induced phototoxicity on adhesion of fluorescently labeled leukocytes. *J Histochem Cytochem* 45: 505-513, 1997.
131. **Saha JK, Xia J, Grondin JM, Engle SK, Jakubowski JA.** Acute hyperglycemia induced by ketamine/xylazine anesthesia in rats: mechanisms and implications for preclinical models. *Exp Biol Med (Maywood)* 230: 777-784, 2005.
132. **Sanderink GJ, Guimart CG, Ozoux ML, Jariwala NU, Shukla UA, Boutouyrie BX.** Pharmacokinetics and pharmacodynamics of the prophylactic dose of enoxaparin once daily over 4 days in patients with renal impairment. *Thromb Res* 105: 225-231, 2002.
133. **Sandison JC.** The transparent chamber of the rabbit's ear, giving a complete description of improved technic of construction and introduction, and general account of growth and behavior of living cells and tissues as seen with the microscope. *Am J Anat* 41: 447-472, 1928.
134. **Sasagawa T, Shimizu T, Yamato M, Okano T.** Endothelial colony-forming cells for preparing prevascular three-dimensional cell-dense tissues using cell-sheet engineering. *J Tissue Eng Regen Med* 10: 739-747, 2016.

135. **Saxer F, Scherberich A, Todorov A, Studer P, Miot S, Schreiner S, Güven S, Tchang LA, Haug M, Heberer M, Schaefer DJ, Rikli D, Martin I, Jakob M.** Implantation of stromal vascular fraction progenitors at bone fracture sites: from a rat model to a first-in-man study. *Stem Cells* 34: 2956-2966, 2016.
136. **Schultz GS, Sibbald RG, Falanga V, Ayello EA, Dowsett C, Harding K, Romanelli M, Stacey MC, Teot L, Vanscheidt W.** Wound bed preparation: a systematic approach to wound management. *Wound Repair Regen* (Suppl 1): S1-S28, 2003.
137. **Schurr MJ, Foster KN, Lokuta MA, Rasmussen CA, Thomas-Virnic CL, Faucher LD, Caruso DM, Allen-Hoffmann BL.** Clinical evaluation of NIKS-based bioengineered skin substitute tissue in complex skin defects: phase I/IIa clinical trial results. *Adv Wound Care (New Rochelle)* 1: 95-103, 2012.
138. **Sckell A, Leunig M.** Dorsal skinfold chamber preparation in mice: Studying angiogenesis by intravital microscopy. *Methods Mol Biol* 1430: 251-263, 2016.
139. **Seebach C, Henrich D, Wilhelm K, Barker JH, Marzi I.** Endothelial progenitor cells improve directly and indirectly early vascularization of mesenchymal stem cell-driven bone regeneration in a critical bone defect in rats. *Cell Transplant* 21: 1667-1677, 2012.
140. **Shahrokhi S, Arno A, Jeschke MG.** The use of dermal substitutes in burn surgery: acute phase. *Wound Repair Regen* 22: 14-22, 2014.
141. **Shepherd BR, Hoying JB, Williams SK.** Microvascular transplantation after acute myocardial infarction. *Tissue Eng* 13: 2871-2879, 2007.
142. **Shevchenko RV, James SL, James SE.** A review of tissue-engineered skin bioconstructs available for skin reconstruction. *J R Soc Interface* 7: 229-258, 2010.
143. **Shi L, Günther S, Hübschmann T, Wick LY, Harms H, Müller S.** Limits of propidium iodide as a cell viability indicator for environmental bacteria. *Cytometry A* 71: 592-598, 2007.
144. **Singer M, Korsh J, Predun W, Warfield D Jr, Huynh R, Davenport T, Riina L.** A novel use of integra™ bilayer matrix wound dressing on a pediatric scalp avulsion: a case report. *Eplasty* 15: e8, 2015.

145. **Sorg H, Krueger C, Schulz T, Menger MD, Schmitz F, Vollmar B.** Effects of erythropoietin in skin wound healing are dose related. *FASEB J* 23: 3049-3058, 2009.
146. **Später T, Frueh FS, Menger MD, Laschke MW.** Potentials and limitations of Integra[®] flowable wound matrix seeded with adipose tissue-derived microvascular fragments. *Eur Cell Mater* 33: 268-278, 2017a.
147. **Später T, Körbel C, Frueh FS, Nickels RM, Menger MD, Laschke MW.** Seeding density is a crucial determinant for the in vivo vascularisation capacity of adipose tissue-derived microvascular fragments. *Eur Cell Mater* 34: 55-69, 2017b.
148. **Später T, Frueh FS, Metzger W, Menger MD, Laschke MW.** In vivo biocompatibility, vascularization, and incorporation of Integra[®] dermal regenerative template and flowable wound matrix. *J Biomed Mater Res B Appl Biomater* 106: 52-60, 2018a.
149. **Später T, Frueh FS, Karschnia P, Menger MD, Laschke MW.** Enoxaparin does not affect network formation of adipose tissue-derived microvascular fragments. *Wound Repair Regen* 26: 36-45, 2018b.
150. **Spronk HM, de Jong AM, Crijns HJ, Schotten U, Van Gelder IC, Ten Cate H.** Pleiotropic effects of factor Xa and thrombin: what to expect from novel anticoagulants. *Cardiovasc Res* 101: 344-351, 2014.
151. **Steinbauer M, Harris AG, Abels C, Messmer K.** Characterization and prevention of phototoxic effects in intravital fluorescence microscopy in the hamster dorsal skinfold model. *Langenbecks Arch Surg* 385: 290-298, 2000.
152. **Stosich MS, Bastian B, Marion NW, Clark PA, Reilly G, Mao JJ.** Vascularized adipose tissue grafts from human mesenchymal stem cells with bioactive cues and microchannel conduits. *Tissue Eng* 13: 2881-2890, 2007.
153. **Supp DM, Boyce ST.** Engineered skin substitutes: practices and potentials. *Clin Dermatol* 23: 403-412, 2005.
154. **Thinda S, Wright HV, Mawn LA.** Integra Bilayer Matrix Wound Dressing closure of large periorbital traumatic wound. *Arch Ophthalmol* 130: 217-219, 2012.

155. **Truong AT, Kowal-Vern A, Latenser BA, Wiley DE, Walter RJ.** Comparison of dermal substitutes in wound healing utilizing a nude mouse model. *J Burns Wounds* 4: e4, 2005.
156. **Tzouvelekis A, Paspaliaris V, Koliakos G, Ntoliou P, Bouros E, Oikonomou A, Zissimopoulos A, Boussios N, Dardzinski B, Gritzalis D, Antoniadis A, Froudarakis M, Kolios G, Bouros D.** A prospective, non-randomized, no placebo-controlled, phase Ib clinical trial to study the safety of the adipose derived stromal cells-stromal vascular fraction in idiopathic pulmonary fibrosis. *J Transl Med* 11: 171, 2013.
157. **Ushiyama A, Yamada S, Ohkubo C.** Microcirculatory parameters measured in subcutaneous tissue of the mouse using a novel dorsal skinfold chamber. *Microvasc Res* 68: 147-152, 2004.
158. **Utzinger U, Baggett B, Weiss JA, Hoying JB, Edgar LT.** Large-scale time series microscopy of neovessel growth during angiogenesis. *Angiogenesis* 18: 219-232, 2015.
159. **Vajkoczy P, Schilling L, Ullrich A, Schmiedek P, Menger MD.** Characterization of angiogenesis and microcirculation of high-grade glioma: an intravital multicolor fluorescence microscopic approach in the athymic nude mouse. *J Cereb Blood Flow Metab* 18: 510-520, 1998.
160. **van der Heijden A, van Dijk JE, Lemmens AG, Beynen AC.** Spleen pigmentation in young C57BL mice is caused by accumulation of melanin. *Lab Anim* 29: 459-463, 1995.
161. **van der Veen VC, van der Wal MB, van Leeuwen MC, Ulrich MM, Middelkoop E.** Biological background of dermal substitutes. *Burns* 36: 305-321, 2010.
162. **van Wachem PB, van Luyn MJ, Olde Damink LH, Dijkstra PJ, Feijen J, Nieuwenhuis P.** Biocompatibility and tissue regenerating capacity of crosslinked dermal sheep collagen. *J Biomed Mater Res* 28: 353-363, 1994.
163. **Vartanian KB, Chen HY, Kennedy J, Beck SK, Ryaby JT, Wang H, Hoying JB.** The non-proteolytically active thrombin peptide TP508 stimulates angiogenic sprouting. *J Cell Physiol* 206: 175-180, 2006.
164. **Wagner RC, Matthews MA.** The isolation and culture of capillary endothelium from epididymal fat. *Microvasc Res* 10: 286-297, 1975.

165. **Wagner RC, Andrews SB, Matthews MA.** A fluorescence assay for micropinocytosis in isolated capillary endothelium. *Microvasc Res* 14: 67-80, 1977.
166. **Weissman I.** Genetic and histochemical studies on mouse spleen black spots. *Nature* 215: 315, 1967.
167. **Zhong SP, Zhang YZ, Lim CT.** Tissue scaffolds for skin wound healing and dermal reconstruction. *Wiley Interdiscip Rev Nanomed Nanobiotechnol* 2: 510-525, 2010.
168. **Zouboulis CC, Adjaye J, Akamatsu H, Moe-Behrens G, Niemann C.** Human skin stem cells and the ageing process. *Exp Gerontol* 43: 986-997, 2008.

9. Acknowledgement

I would like to sincerely thank all of those who supported me in putting together this doctoral thesis.

First, I would like to thank Prof. Dr. Michael D. Menger and Prof. Dr. Matthias W. Laschke for providing such a fascinating and challenging research topic as well as granting me the possibility to continuously work at the Institute for Clinical and Experimental Surgery at Saarland University in Homburg under such wonderful working conditions.

Particular thanks to Prof. Dr. Matthias W. Laschke for his outstanding support. From the very first day, his constant assistance, constructive criticism, personal engagement, and enthusiasm for scientific research awakened my interest in the field of tissue engineering and regenerative medicine. He is the reason for my great interest in science and the enjoyment of the work I am doing.

Furthermore, I would like to specially thank Dr. Florian Früh for the great working relationship and assistance throughout the time of our collaboration as well as providing Integra[®] samples for our research.

Moreover, I would like to thank Dr. Emmanuel Ampofo for the helpful discussions, Dr. Wolfgang Metzger for the great assistance regarding scanning electron microscopy, Christina Marx for the assistance in cell culture techniques, Ruth Nickels for the great teaching of flow cytometric methods, all co-workers of the animal facility as well as Janine Becker, Sandra Schuler, and Caroline Bickelmann for the preparation of histological samples.

The biggest debt of gratitude goes to my parents and, in particular, my wife. You fully supported me in every way possible throughout the time of my work. Because of you I can be who I am today.

10. Publications

10.1. Original articles

The data of this present doctoral thesis led to the publishment of the following original articles:

Später T, Frueh FS, Menger MD, Laschke MW. Potentials and limitations of Integra® flowable wound matrix seeded with adipose tissue-derived microvascular fragments. *Eur Cell Mater* 33: 268-278, 2017.

Später T, Körbel C, Frueh FS, Nickels RM, Menger MD, Laschke MW. Seeding density is a crucial determinant for the in vivo vascularization capacity of adipose tissue-derived microvascular fragments. *Eur Cell Mater* 34: 55-69, 2017.

Später T, Frueh FS, Metzger W, Menger MD, Laschke MW. In vivo biocompatibility, vascularization, and incorporation of Integra® dermal regenerative template and flowable wound matrix. *J Biomed Mater Res B Appl Biomater* 106: 53-60, 2018.

Später T, Frueh FS, Karschnia P, Menger MD, Laschke MW. Enoxaparin does not affect network formation of adipose tissue-derived microvascular fragments. *Wound Repair Regen* 26: 36-45, 2018.

Further original articles:

Ampofo E, **Später T**, Müller I, Eichler H, Menger MD, Laschke MW. The marine-derived kinase inhibitor fascaplysin exerts anti-thrombotic activity. *Mar Drugs* 13: 6774-6791, 2015.

Frueh FS, **Später T**, Lindenblatt N, Calcagni M, Giovanoli P, Scheuer C, Menger MD, Laschke MW. Adipose tissue-derived microvascular fragments improve vascularization, lymphangiogenesis, and integration of dermal skin substitutes. *J Invest Dermatol* 137: 217-227, 2017.

Frueh FS, **Später T**, Menger MD, Laschke MW. Isolation of murine adipose tissue-derived microvascular fragments as vascularization units for tissue engineering. *J Vis Exp* 30: 122, 2017.

Später T, Müller I, Menger MD, Laschke MW, Ampofo E. Dual inhibition of PI3K and mTor by VS-5584 suppresses thrombus formation. *Platelets* 15: 1-11, 2017.

Karschnia P, Scheuer C, Heß A, **Später T**, Menger MD, Laschke MW. Erythropoietin promotes network formation of transplanted adipose tissue-derived microvascular fragments. *Eur Cell Mater* 35: 268-280, 2018.

Frueh FS, **Später T**, Körbel C, Scheuer C, Simson AC, Lindenblatt N, Giovanoli P, Menger MD, Laschke MW. Prevascularization of dermal substitutes with adipose tissue-derived microvascular fragments enhances early skin grafting. *Sci Rep*, in press, 2018.

10.2. Citable abstracts

Später T, Ampofo E, Müller I, Eichler H, Menger MD, Laschke MW. The marine-derived kinase inhibitor fascaplysin exerts anti-thrombotic activity. *Eur Surg Res* 55: 277, 2015.

Frueh FS, **Später T**, Lindenblatt N, Calcagni M, Giovanoli P, Scheuer C, Menger MD, Laschke MW. Adipose tissue-derived microvascular fragments improve vascularization, lymphangiogenesis, and integration of dermal skin substitutes. *Eur Surg Res* 57: 330-331, 2016.

Später T, Frueh FS, Metzger W, Menger MD, Laschke MW. In vivo biocompatibility, vascularization, and incorporation of Integra[®] dermal regenerative template and flowable wound matrix. *Eur Surg Res* 57: 321, 2016.

Später T, Körbel C, Frueh FS, Nickels RM, Menger MD, Laschke MW. Seeding density is a crucial determinant for the in vivo vascularization capacity of adipose tissue-derived microvascular fragments. *Eur Surg Res* 58: 322, 2017.

Nalbach L, Ampofo E, **Später T**, Menger MD, Laschke MW. Generation of prevascularized pseudo-islets by co-culture of adipose tissue-derived microvascular fragments and islet cells in liquid overlay technique. *Eur Surg Res* 58: 325, 2017.

Später T, Müller I, Menger MD, Laschke MW, Ampofo E. Dual inhibition of PI3K and mTor by VS-5584 suppresses thrombus formation. *Eur Surg Res* 58: 68, 2017.

10.3. Non-citable abstracts

Später T, Frueh FS, Karschnia P, Menger MD, Laschke MW. Enoxaparin does not affect network formation of adipose tissue-derived microvascular fragments. *26. Wissenschaftliche Jahrestagung der Saarchirurgen*, Kirkel, 2018.

11.4. Awards

Nachwuchsförderpreis (Young investigator award) of the “Sektion Chirurgische Forschung der Deutschen Gesellschaft für Chirurgie”, 2018.